STUDIES OF ATMOSPHERIC EFFECTS ON FREE-SPACE THZ PULSE PROPAGATION AND APPLICATIONS

By

YIHONG YANG

Bachelor of Science in Material Physics
Nankai University
Tianjin, China
2006

Master of Engineering in Material Physics
Nankai University
Tianjin, China
2009

Submitted to the Faculty of the
Graduate College of the
Oklahoma State University
in partial fulfillment of
the requirements for
the Degree of
DOCTOR OF PHILOSOPHY
December, 2014

STUDIES OF ATMOSPHERIC EFFECTS ON FREE-SPACE THZ PULSE PROPAGATION AND APPLICATIONS

Dissertation Approved:

Dr. Daniel R. Grischkowsky

Dissertation Adviser

Dr. Weili Zhang

Dr. James C. West

Dr. Albert T. Rosenberger

ACKNOWLEDGEMENTS

This dissertation was conducted at the Ultrafast THz Optoelectronic Laboratory, Oklahoma State University. It could not be finished without the support from the professors, staff, colleagues in OSU and my family. It is my honor to acknowledge all the assistance, guidance and encouragement these people gave me.

First of all, I would like to express my sincere gratitude to my adviser Prof. Daniel R. Grischkowsky, who gave me the opportunities to participate in Ultrafast Terahertz Research Group. I really appreciate his constant guidance, support, and encouragement during last five years. His strong academic background, broad knowledge and exceptional intelligence shaped my scientific development by introducing me with valuable theoretical and experimental ideas. I am proud of the work we did together and believe all of the achievement and trainings will always inspire me to find the "Truth and Beauty" in my future career.

I would like to express my special appreciation to Dr. Weili Zhang. He is helpful to continuously provide me valuable advices with his patience and encouragement during my graduate study career here. I would also like to thank other committee members, Dr. James West and Dr. Albert Rosenberger for their helpful research advice and suggestion in my Ph.D Study.

I want to thank Dr. Joseph Melinger, who is an excellent scientist from the Naval Research Laboratory. I am grateful to his introduction and explanation of the data analysis and modeling in the several projects we worked on together. My understanding in the research was improved through the experience. I would like to thank Dr. John O'Hara. I learned a lot research advice and knowledge from him through many insightful discussions with his patience and trust.

It is my pleasure to thank my lab mates in the UTOL group for their support and care in my five years Ph.D career. There are past senior group members Mufei Gong, Sree Harsha, Michael Theuer, Jianqiang Gu, Zhen Tian, Xinchao Lu, Yongyao Chen and Dr. Yuping Yang, who gave me help either on my research or on my daily life, when I first came into the group. There are current group members, who we work together to solve problems and helped each other. I am grateful to: Alisha Shutler, Mahboubeh Mandehgarm, Wei Cao, Ran Huang, Liansheng Zheng, Lin Guo, Siyu Tan, Quan Li. I also thank the staff who gave me support: Minh Dinh, Helen Daggs, Lory Ferguson, Brian Ritthaler, Gary Thacker and Stacy James.

Finally, I want to express my deepest gratitude to my family: my parents, my parents-in law and my loving wife, Ningning Xu. Without their understanding, support and encouragement, I could not finish my Ph. D. study.

Name: YIHONG YANG

Date of Degree: DECEMBER, 2014

Title of Study: STUDIES OF ATMOSPHERIC EFFECT ON FREE-SPACE THZ PULSES PROPAGATION AND APPLICATIONS

Major Field: ELECTRICAL ENGINEERING

Abstract:

Within THz frequency range, free-space propagated EM wave and the related applications have attracted a lot of attention, due to promising solutions for new types of remote sensing, wireless communications and security applications. However, the characteristics of free-space THz wave are degraded by several atmospheric conditions, such as water vapor absorption and pulse distortion.

In this thesis, a comprehensive study on atmospheric effects on free-space THz signal and its potential applications by using the state-of-art Long-Path THz-TDS system is presented. Two types of absorptions from the ambient water vapor have been investigated: the resonant absorption which is associated with strong phase shifts and the continuum absorption. The molecular response theory is used as the lineshape function based on parameters from JPL and HITRAN databases for simulation to water vapor resonant absorption and phase shift. Not only were the THz digital bit observed for potential wireless communications, but the refractivity of water vapor was also obtained by line-by-line summation.

A series of accurate experiments of water vapor continuum absorption have been carried out by using the 170 m Long-Path THz-TDS system. With precise experimental results and MRT simulation, the parameters for general model of water vapor continuum absorption have been successfully obtained within several THz transparent windows. As another kind of atmospheric condition, artificial fog fully filled the 137 m long sample chamber, in order to investigate absorption and phase shift of the atmospheric diffusive scattering mediums.

With all the quantitative understanding of the atmospheric effects, a comprehensive atmospheric model for the free-space THz signals has been established, including the humidity, temperature and distance. This model can be used to provide a theoretical verification for all of the free-space THz applications.

To demonstrate another free-space THz application, a series of experiments of THz-TDS remote detection of small molecules vapor have been performed. Samples of CH_3CN, D_2O and HDO have been successfully detected using 170 m Long-Path THz-TDS system. Moreover, the reaction ratio of the transition from H_2O and D_2O to HDO has been monitored in time.

TABLE OF CONTENTS

Chapter Page

I. **INTRODUCTION** 1

1.1 Water Vapor Effects within THz Range 1
1.2 Scope of this Thesis 3

II. **EXPERIMENTAL SETUP** 6

2.1 Terahertz Time Domain Spectroscopy (THz-TDS) 6
2.2 Long-Tube and Long-Path THz Systems 6
2.2.1 Principle of Periodic Synchronization 6
2.2.2 6.68 m Long-Tube Setup 9
2.2.3 170 m Long-Path Setup 10
2.2.4 RH Controlled Sample Chamber 12
2.2.5 Laser Clock Drift and Thermal Drift Problem 12
2.4 System Capability 14

III. **RESONANT ABSORPTION LINES OF ATMOSPHERIC WATER VAPOR** 15

3.1 The Preliminary Experimental Results of Long-Tube and Long-Path System 16
3.1.1 6.68 m Long-Tube System 16
3.1.2 170 m Long-Path System 20
3.2 Resonant Absorption Line Theory 20
3.2.1 van Vleck-Weisskopf (vV-W) Theory 21
3.2.2 Line Intensity and vV-W Line Shape Function 22
3.2.3 Time Domain Pulse Calculation 28
3.2.4 Mismatched Absorption Problem 31
3.3 Longer Path Prediction 31
3.3.1 Observed Wireless Communication Windows 32
3.3.2 Proposed Ideal Wireless Communication Channels 35

Chapter Page

IV. **WATER VAPOR DENSITY RELATED ATMOSPHERIC REFRACTIVITY** 38

4.1 Experiments of Water Vapor Refractivity within THz Range 38
4.2 Microwave and MM-Wave Debye Theory Approach 42
4.2.1 Debye Theory 42
4.2.2 Inconsistent Debye Power Absorption 43
4.3 Relationship of vV-W Theory and Debye Theory 44
4.3.1 Converge from vV-W to Debye 45
4.3.2 Water Molecule Dipole Moment Determination 47

V. **WATER VAPOR CONTINUUM ABSORPTION** 50

5.1 Introduction 50
5.2 Resonant Absorption Lineshape Function 52
5.2.1 vV-W Model with Cutoff Frequency (vV-Wc) 52
5.2.2 Molecular Response Theory (MRT) 53
5.2.3 Empirical Continuum Absorption Equation 54
5.2.4 Cross-Term (X term) 57
5.3 Experimental Results and Discussion 58
5.3.1 High Relative Humidity Reference Signal 59
5.3.2 Low Relative Humidity Reference Signal 66
5.3.3 Backward Propagation 68
5.3.4 The Comprehensive Water Vapor Absorption Model 74

VI. **BROADBAND THZ SIGNAL PROPAGATION THROUGH FOG** 79

6.1 Introduction 79
6.1.1 Particle Size Distribution 80
6.2 Experiments 82
6.2.1 Double Debye Model 85
6.3 Discussion 86
6.3.1 Fog, Rain and Scintillations 90

VII. **THZ DETECTION OF ATMOSPHERIC SMALL MOLECULE VAPORS** 93

7.1 Introduction 94
7.2 THz Detection of Small Molecule Vapor 95

7.2.1 Experimental Setup 95
7.2.2 Long-Tube System Results and Discussion 98
7.2.3 Long-Path System Results and Discussion 104
7.3 Remote THz Monitoring of an Evolving Gas-Phase Mixture 109
7.3.1 Determination of Decay Time of Sample Chamber 110
7.3.2 Measurements of Reaction Rate of D_2O and H_2O 110

VIII. **SUMMARY AND FUTURE PROSPECTS**.....116

REFERENCES.....118

PUBLICATION LIST 124

LIST OF TABLES

Table **Page**

5.1 The determined values of $\Delta\alpha_{cx}$, X, $\Delta\alpha_c$ in dB/km at four THz windows with different density 65

5.2 Laboratory determinations of water vapor self and foreign continuum parameters in millimeter wave and THz range. The CW and CA parameters are in units of dB/km/(GHz hPa)^2 66

LIST OF FIGURES

Figure **Page**

2-1. (a) Standard THz-TDS system set-up. (b) Diagram of THz pulses from standard THz-TDS system coupled into Long-Tube and Long-Path system 8

2-2. (a) Diagram of the sealed long-tube system with round-trip length of 6.18m (b) Top (x-z plane) view of the 170 m long-path set-up with the sample chamber outlined (left red rectangle). 11

3-1. Long-Tube Results (a). Measured THz reference pulse (lower trace) and measured THz sample pulse (upper trace). (b). Corresponding amplitude spectrum (upper curve) for the THz reference pulse and the sample pulse (lower curve). 17

3-2. The amplitude transmission through 6.18 m of atmosphere at 21 ℃ with RH 51%. 10 water windows (circled numbers) and 8 weak water lines are marked 18

3-3. Long-Path Results (a) The free space signal of standard THz-TDS system and the output transmitted THz pulse after 170 m propagation. (b) Corresponding amplitude spectrum of (a). (c) The output transmitted THz pulses in (a). (d) Corresponding amplitude spectrum of (c). 19

3-4. vV-W amplitude absorbance (upper curve) and the corresponding phase shift in radians (lower curve) based on Eqs. (3-2a) and (3-2b), with 7 GHz FWHM linewidth 24

3-5. The vV-W amplitude transmission compared to the experimental measurements of Fig. 3-2. 26

3-6. (a). Calculated phase $\varphi = \Delta kL$ (solid line) and measured phase (dots) for transmission through 6.18 m of atmosphere at 21 ℃ with RH 51%. (b). Refractivity $(n(\omega) - 1)$ obtained from Eq.(3-10) and the results of (a).. 27

3-7. The measured transmitted THz pulse of Fig. 3-1a (upper trace) is compared to the calculated THz pulse with z = 6.18 m (lower trace).. 29

Figure **Page**

3-8. (a) Measured output pulse for 1.9 g/m^3 (outgoing pulse), the measured output pulse for 8.5 g/m^3 and the calculated output pulse using the vV-W calculation. (b). Corresponding amplitude spectra. 30

3-9. (a) 167 m outgoing signal with propagated pulses after 100m, 200m of vV-W calculated propagation. (b) Corresponding amplitude spectra. (c) 167 m outgoing signal with propagated pulses after 500 m, 1000 m and 2000 m of vV-W calculated propagation. (d) Corresponding amplitude spectra. (e) The calculated vV-W propagation of the phase coherent THz-bit pulse. (f). Corresponding amplitude spectra.. 33

3-10. (a) Calculated vV-W propagation of the Low-Frequency THz-bit pulse I. (b) Propagation of the High-Frequency THz-bit pulse II. (c) Amplitude spectra of the THz-bit pulses I and II 34

3-11. Calculated amplitude transmission for a 2 km length of water vapor at RH 58% and 20^{o}C (10g/m^3) with O_2 vapor and proposed two THz lines.....36

4-1 (a) Three measured transmitted THz pulses (top) RH 22.23%, (middle) RH 43.01%, (bottom) RH 58.42%. (b) Corresponding amplitude spectra. 40

4-2. (a) The measured pulse time-shift vs RH at 21 ℃ for four independent measurements. (b) Replot of the data and extended lines of (a), with the time delay at zero RH subtracted from the data series. 41

4-3. Refractivity of water vapor at 20 ^{o}C and 10 g/m^3, calculated by the complete van-Vleck Weisskopf theory. The earlier measurements of are indicated by the open circles. The straight line at 61.06 x10^{-6} marks the complete calculated value of (n(0) -1). 49

5-1. (a) Amplitude transmission comparison between vV-W, vV-Wc and MRT. (b) Corresponding power attenuation in dB/km 55

5-2. Absorption line comparison of a single resonance line of vV-W, FL, MRT, and the vV-Wc with cut-off at 1.75 THz.. 56

5-3. (a) Reference pulse (top trace) and sample pulse (bottom trace). (b) Amplitude spectra corresponding to (a). (c) Reference pulse (top tract) and two sample pulses (lower traces). (d) Amplitude spectra corresponding to (c).....60

Figure **Page**

5-4. (a) Amplitude transmission for $\Delta\rho_w$ = 7.0 g/m^3 in Fig.5-3d. (b) Measured power attenuation coefficients $\Delta\alpha_x$ in dB/km, for the water vapor density differences of $\Delta\rho_w$ = 4.1 g/m^3 (bottom blue circles), $\Delta\rho_w$ = 5.2 g/m^3 (middle red circles) and $\Delta\rho_w$ = 7.0 g/m^3 (top black circles), and MRT calculation for $\Delta\rho_w$ = 4.1 g/m^3 (bottom purple line). 62

5-5. (a) The measured total absorption (blue circles), smoothed measured THz window (red solid line), MRT lineshape (black line). The quadratic fitting for X (black dash line) with yellow highlight for 7.0 g/m^3. (b) The calculated cross-term X absorption for 7.0 g/m^3 (top black line), 5.2 g/m^3 (middle red line), and 4.1 g/m^3 (bottom blue line). (c) The continuum absorption and corresponding fitting (solid lines), and the historical curve for 7 g/m^3 (dash dot line). The MRT calculation of Fig. 5-5(a) is shown as the lower red curve and is also shown as the 5X magnified red curve 64

5-6. Two sets of measurements are shown as: Measured THz pulses transmitted through the 137 m sample chamber in (a) and (e); Corresponding amplitude spectra in (b) and (f); Corresponding power attenuation in (c) and (g); Corresponding continuum absorption in (d) and (h). 67

5-7. (a) RH 0% outgoing pulse, Measured THz pulse transmitted through the 170 m path at RH 8% at 21 ^{o}C (black middle pulse) and the THz pulse transmitted through the 137 m path sample chamber at RH 65% at 21 ^{o}C (red lower pulse). (b) Corresponding amplitude spectra. 70

5-8. (a) Calculated (red upper) pulse compared with measured (black lower) pulse transmitted through the same RH 8%, 170 m long path. (b) Comparison of the measured with the calculated spectrum. 72

5-9. Measured water vapor absorption Δαx (black curve and circles), calculated MRT resonant lines absorption ΔαMRT (red curve). Continuum absorption given by the blue circles, compared to Eq. (5-5) (black curve). 73

5-10. Summary results for the atmosphere at RH 58% and 20 ℃ (density of 10 g/m^3). 75

6-1. (a) Photograph of artificial fog generator. (b) Photograph of clear–air chamber. (c) Photograph of fog filled chamber. 83

Figure **Page**

6-2. (a). Measured THz pulses transmitted through sample chamber without fog (upper black trace) and with fog (lower red trace) (b) Corresponding amplitude spectra without fog (upper black) and with fog (lower red).....84

6-3. Amplitude transmission (upper black) curve, the ratio of amplitude spectra of Fig. 6-2b, with fog to that without fog. The calculated amplitude transmission (middle red) curve for water vapor density increase of 1.1 g/m^3. 88

6-4. Top black reference curve is without fog. Middle red curve is calculated transmitted spectrum through 137 m of water vapor (1.1 g/m^3). Bottom blue curve is the calculated transmitted spectrum through 137 m of (1.1 g/m^3) fog. 89

7-1 (a). Diagram of the Long-tube apparatus based on a standard THz-TDS spectrometer with 5.4 meter round trip path length enclosed tube for vapor measurements (highlight). (b) Schematic from the top (x-z plane) of the 170 meter round trip long path apparatus with the 1.2 m sample chamber (highlight). 96

7-2. (a) Measured THz signal propagated through chamber with CH_3CN. (b) Corresponding spectral amplitude for CH_3CN. The RH in the chamber was 14%. The inset shows the time base expanded in the echo region. 99

7-3. (a)Amplitude absorbance spectra for CH_3CN vapor contained in the long - tube at three concentrations: 200 ppm (top blue curve), 50 ppm (middle red curve), and 12 ppm (bottom black curve). (b) Calculated absorbance spectrum for CH_3CN. The solid curve is the sum of the contributions from CH_3CN in the ground vibrational state and excited vibrational state v8=1. The dotted curve is the calculated spectrum from CH_3CN (v8=1). 100

7-4. (a) Spectral amplitudes for the reference (top black curve) and signal (red curve) for D_2O sample with a vapor concentration of 750 ppm and at RH = 51%. The inset shows absorption resonances in the expanded higher frequency range. (b) Experimental amplitude absorbance spectrum (black curve) and JPL fitting (red curve). 103

7-5. Spectral amplitudes for the reference (upper black curve) and the CH_3CN sample (lower red curve) for the 170 meter path measurement. The concentration of acetonitrile is 800 ppm in the sample tube. The laboratory relative humidity was 50%.....105

Figure **Page**

7-6. Experimental amplitude absorbance spectrum (black curve) where D_2O liquid is introduced into the 1.2 m (round-trip) sample chamber to give a concentration of approximately 3000 ppm. The red curve indicated a relative fraction of HDO: D_2O of 2.4:1. 107

7-7. Frequency spectra of set of 7 continuous scan of HDO sample using Long-Tube system. Inset shows the increasing amplitude at absorption line at 0.895 THz. 111

7-8. THz-TDS monitoring of an evolving D_2O plume. Purple arrows mark the D_2O lines and the red arrows marks HDO lines. The inset shows the transition indicated by change of line center frequency. 112

7-9. (a) Reaction rate calculated based on D_2O decay curve. (b) Reaction rate calculated based on HDO changing curve 113

CHAPTER I

INTRODUCTION

1.1 Water Vapor Effects within THz Range

Terahertz (THz) frequency radiation covers the range from 100 GHz to 10 THz which locates between microwaves and infrared regions. THz technology has attracted a lot of attentions, and the corresponding applications based on THz pulses are growing enormously, since interests on nondestructive evaluation, remote detection, wireless communication and security applications, such as sensing and imaging, have increased rapidly [1]. For example, the wireless communication with carrier frequency within the THz region are very attractive, not only because THz frequency has the larger frequency bandwidth and higher transmission rate than the current microwave bands, but also has the less scattering loss than optics in the diffusive atmosphere, such as dust and fog [2]. Moreover, the low loss and large bandwidth digital THz wireless ground link and satellite link are a promising alternative solution to solve the important problem of providing isolated cities, communities, remote industrial, technical and scientific sites with wideband access to the fiber backbone, instead of using the existing microwave ground or satellite links [3-5].

One of common properties among above free-space THz applications is the requirement of THz pulses propagated through atmosphere. However, THz pulses suffer attenuation and group velocity dispersion (GVD) from the atmospheric water vapor and scattering loss from suspended

particles, such as fog and smoke, especially within the frequency range from 0.05 to 2 THz.

The breakthrough technology to significantly improve THz research was the invention of THz Time-Domain Spectroscopy (THz-TDS) by Prof. Grischkowsky [6]. The coherent detection associated with femtosecond laser can measure the electrical field of THz pulses as a function of time by varying the time delay between the laser pulses gated window and THz pulses at receiver. The coherent detection determines the high signal-to-noise ratio without background noise interruption. The Fourier Transform of measured electrical field provides the complete complex amplitude spectral response of the sample, including absorption and phase shift.

Technology advances had promoted the research of atmospheric water vapor absorption in some aspects. For example, the Fourier Transform Spectroscopy (FTS), Fabry Perrot (FP) resonator [7, 8] have made progress in the study of water vapor effect. However, because of their relatively low sensitivity within THz frequencies, the technique of THz-TDS becomes more important in this study.

The water molecule is an asymmetric rotor with a permanent dipole moment along the axis of symmetry. In some conditions, two or more water molecules bond together as dimer, trimer, or cluster in gas phase. In the frequency range from 0.1 to 10 THz, the frequency-dependent absorption $\alpha(\omega)$ and the corresponding dispersive index of refraction $n(\omega)$ of water vapor control the electromagnetic propagation of broad-bandwidth THz pulses in the atmosphere, because water molecules have hundreds of relatively strong rotational resonant absorption lines from the radio wave range through the terahertz region. To data, several professional spectroscopic databases including Molecular Spectroscopy Database in Jet Propulsion Laboratory (JPL) [9], High-resolution Transmission Molecular absorption database (HITRAN) [10] have been created to supply the most accurate values of many physical parameters, such as intensity, line center frequency and line width, for water vapor molecule and other materials. By applying the molecular spectroscopic values in the databases to a proper lineshape function, the absorption

and phase shift curves over broadband THz frequencies can be calculated and help us to determine the attenuation on the transparent windows, which locate between absorption lines.

Between the strong resonant lines, the so-called atmospheric windows allow the transmission of propagated pulses, which can be used as the broad frequencies communication bands and molecular spectroscopy monitor. However, an additional continuum absorption exists within those transparent windows, which cannot be explained by the far-wing absorption of the resonant lines. It is still not very clear that how the continuum absorption derived [11]. But it has been proven that it has a frequency quadratic dependence based on an empirical theory fitting [12].

Consequently, a good understanding to the atmospheric water vapor effects within THz range are crucial for most of the THz applications, which required the long distance propagation of THz pulses through atmosphere, such as ground- and satellite-based radio astronomy [13], communication links [5], and remote spectroscopic application [14]. In this thesis, I will use the long-path THz-TDS technique to study the THz pulses power attenuation and phase dispersion after propagating through long path water vapor with corresponding theoretical modeling, as well as the water vapor refractivity and continuum absorption within THz frequencies [15].

1.2 Scope of this Thesis

The outline of this Thesis is as follows:

Chapter 2 introduces the two long path THz setups based on the standard THz-TDS system used in our experiments [14-19]: the 6.68m long-tube and the 170m long-path. By utilizing the stable repetition pulses of the femtosecond mode-lock laser as a precise clock, the THz pulses path can be increased to hundreds of meters without adding any optical compensation path. Then, the long path THz systems were designed and connected with a RH controlled chamber to have the ability of studying the characteristics (transit time, attenuation, phase) of the

propagated THz pulses through a certain distance with different levels of the atmospheric RH conditions inside the chamber.

Chapter 3 discusses the theoretical expressions of the absorption $\alpha(\omega)$ and the phase $\Delta k(\omega)$ of water vapor resonance lines in van Vleck-Weisskopf (vV-W) model [20]. Then, we examine the vV-W model with our experimental power attenuation and phase shift by using the values of intensity, line center frequency and linewidth from the JPL and the HITRAN databases [9, 10]. Based on the good agreements between the vV-W theoretical and our existing experimental results, we use this vV-W model to predict the propagation results for longer distance up to 2 km, which could not be set up in our lab. Two potential high data speed THz wireless communication channels are observed and discussed in detail [21].

Chapter 4 studies the refractivity of water vapor at zero frequency by analyzing the linear relationship between the refractivity and the transit times of propagated THz pulses, which can be explained by the Debye theory [22]. However, the corresponding absorption of the Debye model is extremely high and not physically correct. In the second section of this chapter, the vV-W model is shown to converge to the Debye theory at zero frequency, and remove the inconsistent phase shift problem in Debye theory.

Chapter 5 investigates the poorly understood continuum absorption, which is shown as the discrepancy between theory and experiments shown in Chapter 3. With the proper pre-factor for the vV-W line shape function derived from the original empirical continuum absorption equation, and MRT model, the calculation fits our measurements in a good agreement with new values of parameters, which gives another view of weighting the effect of dimer for continuum absorption.

Chapter 6 demonstrates the experiments of broadband THz signal propagation through dense artificial fog. According to these tentative experimental results of minimal distortion and attenuation of broadband, complex THz signals through 137 m of dense fog with an approximate

visibility of 7 m, the performance of high speed THz wireless communication channels would be maintained[21, 23], as well as the transparent windows reserved for observation of finger print spectra in remote detection applications. The propagation of broadband THz pulses through a dense artificial fog, shows that broadband THz waves could be also considered as a promising illumination source for many potential applications.

Chapter 7 demonstrates the THz-TDS remote detection of dilute vapor of small molecules, as well as the broadband THz-TDS monitoring of evolving HDO and D_2O with a sensitivity of 10 % amplitude absorption (5 minute integration time). The measurements show potential for broadband THz sensing of small-molecule vapors with a range of a few hundred meters. The experimental result shows that THz-TDS monitoring of reaction kinetics within a vapor plume is possible.

Chapter 8 presents the summary of the thesis projects and future prospects.

CHAPTER II

EXPERIMENTAL SETUP

2.1 Terahertz Time Domain Spectroscopy (THz-TDS)

All of the experiments discussed in this Thesis are based on the standard Terahertz Time Domain Spectroscopy (THz-TDS) [6], as shown in Fig. 2-1a. The broadband THz pulses are generated and detected by photoconductive dipole antennas on a semiconductor substrate, which are excited by a 10 mW, 800nm, 89.69 MHz repetition rate femtosecond laser pulses from a Ti-sapphire mode-lock laser. The generated THz beam from transmitter is collimated by a pair of high-resistivity truncated spherical silicon lens and a pair of the paraboloidal mirrors to receiver. Finally, the electric fields of the THz pulse are measured as a function of time by varying the time delay between the laser pulse and THz signal at receiver. The corresponding amplitude spectra can be obtained by taking the Fast Fourier transform (FFT) of the measured THz pulse.

The THz-TDS technique has several advantages on the long-path propagation study, than for other methods, such as Fourier Transform spectrometers (FTS). The first advantage of THz-TDS is the extreme sensitivity with a high signal-to-noise ratio up to 10,000 and very low energy per THz pulse (0.3 femtoJoule), because the background noise is not measured during the time between the repetitive laser pulses, but only within the 0.6 ps window gated by each 80 fs laser pulse on the photoconductive receiver. Another powerful advantage is that the electric field of the

repetitive pulses of THz radiation is measured directly. In addition, the FFT of the THz pulse measurements provide the complete complex amplitude spectral response of the sample, which illustrates the potential applications for THz-TDS to make entirely new type measurements.

2.2 Long-Tube and Long-Path THz System

Combining a set of collimating, focusing and flat mirrors with proper design to a standard THz-TDS system, it is possible to extend the THz path from 50 cm to more than 100 m. The generated diffracted broadband THz signal is collimated into a diffraction-limited beam, that directs a relatively large fraction of the THz beam onto a distant target and returned with good coupling efficiency into the THz receiver, by a removable output and outgoing coupling mirrors unit shown in Fig. 2-1b.

The extended THz path with range of 100 m provides us an important advantage for research related to atmospheric water vapor absorption, which absorbs large amount of THz signal. Compared to the usual sample chamber of several meters, the sample chamber introduced in our setup has 137 m distance for THz signal propagation through well-controlled relative humidity. Weak water vapor absorption lines were observed in our experiments due to long propagation distance. The good 1 GHz agreement with databases proved the high quality of stability and reproducibility of our system.

2.2.1 Principle of Periodic Synchronization

In standard THz-TDS system, as shown in Fig. 2-1a, the arrival time of the THz signal (TP1) which is excited by laser pulse LP1 at receiver (Rx) should match the arrival time of LP1 in receiver side by adjusting the time delay. Tx, Rx denote the transmitter and receiver. LP1, TP1 denotes the first laser pulse and THz pulse, respectively. In other word, after split mirror, the Tx-side laser path plus THz path should equal to the Rx-side laser path.

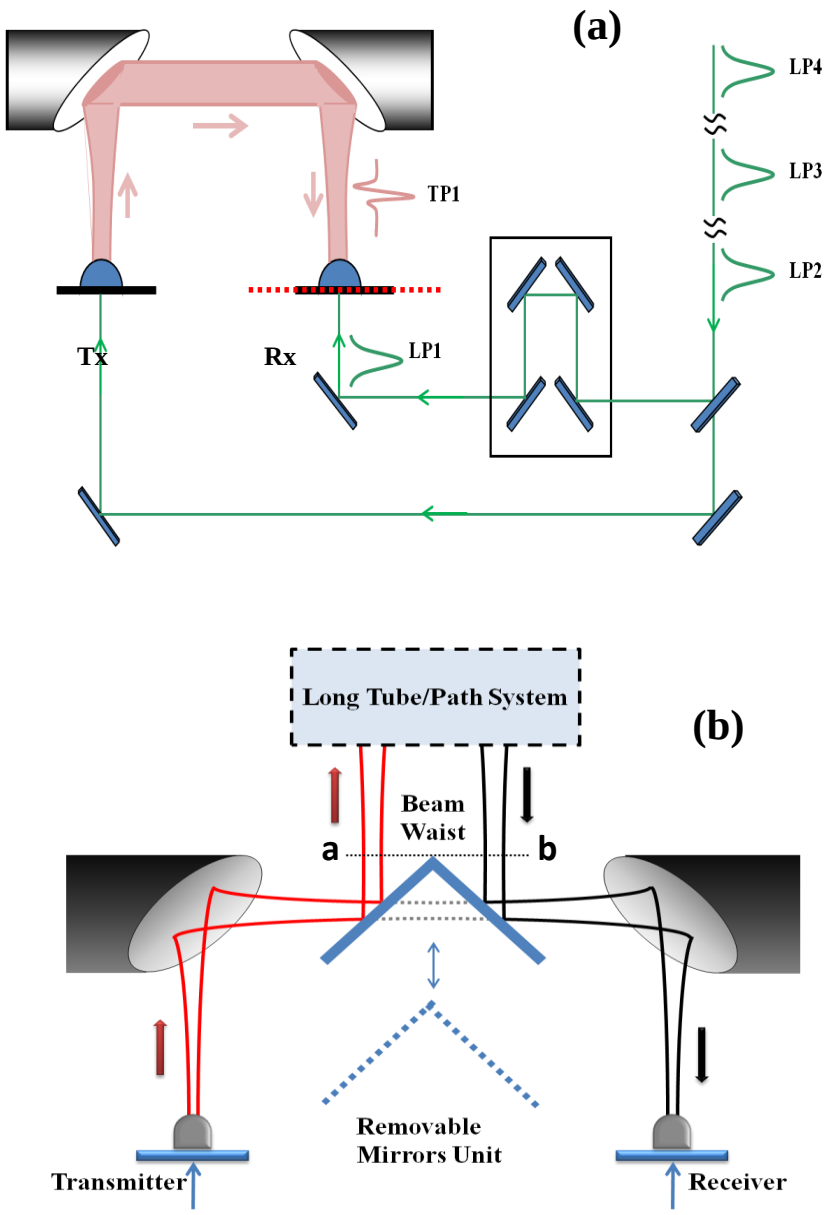

Fig. 2-1. (a) Standard THz-TDS system set-up diagram. (b) Diagram of THz pulses from standard THz-TDS system coupled into long-path and long-tube system.

Instead of adding compensated optical path in Rx-side when the THz path is extended, the technique of matching path length by using the laser clock as a precise multiple steps delay line is employed in the long path system shown in Fig. 2-1a. From the outgoing beam waist position a to incoming beam waist position b shown in Fig. 2-1b, the total extra round trip path distance must be chosen to equal integer times (N) of the round-trips of the ultrafast optical pulses in the mode locked Ti-Sapphire pumping laser with a repetition rate of 89.69 MHz, corresponding to a round-trip distance of 334 cm. Consequently, the laser sampling pulses, used to measure the THz reference and sample pulses, are delayed by N pulses down the pulse train from the excitation pulses.

The alignment of the long-path THz optical train typically requires no adjustments over periods as long as two-weeks. The main stability issue is the reproducibility of the THz outgoing pulses to the optical train, caused by changes in the laser driving and sampling pulses.

2.2.2 6.68 m Long-Tube Setup

Firstly, we present the experimental set-up of long-tube THz-TDS system with extended round trip THz path of 6.68 m in Fig. 2-2a [16].

The total extra round trip path distance of 6.68 m is designed to equal 2 times round-trips of the ultrafast optical pulses with a round-trip distance of 334 cm, shown as Fig. 2-2a. The extra THz path includs a round-trip distance of 6.18 m within the relative humidity (RH) controllable chamber from the film window of box #1 to the 6 inch end mirror, and a 25 cm distance from the film window to the top of the coupling mirror prism in box #1.

For the best THz coupling efficiency, an Au-coated spherical mirror with the 6 inch (15.24 cm) diameter and 120 inch (304.8 cm) radius of curvature is used as beam collimator and reflector at the end of long-tube shown in Fig. 2-2a.

The THz-TDS system together with the removable mirrors is contained in the air-tight box #1, which is always filled with dry air. The 15 cm diameter window connecting boxes #1 and #2 is made by stretching 12.5 μm cling wrap over the opening and sealing the edges with tape. Box #2 is air-tight and connected to a 6 inch (15.24 cm) internal diameter, commercially available PVC pipe. Box #2 together with the PVC pipe enclosure can be filled with dry air or moist room air via the connection on the PVC cap on the T connection, where a hygrometer is installed to monitor the inside humidity.

2.2.3 170 m Long-Path Setup

An improved long-path THz setup is build based on previous 6.68 m long-tube setup with total extra round trip path distance increase to 170 m. The long-path THz setup enables the propagation of the repetitive, broad-band, THz pulse of the low-power THz beam and bandwidth from 0.1 to 1 THz transmitted through 170 m of the atmosphere, as shown in Fig. 2-2b [19].

Here, we use 6 large optical-quality flat mirrors with Enhanced Aluminum coatings to guide the THz beam as M4-M9 in Fig. 2-2b. The fact that we can measure to pico-second precision, shows that the THz optical train is surprising stable, even though the mirror mount supports for M5-M9 (shown in Fig. 2-2b) are placed on the floor of our basement laboratory. Mirrors M1-M4, and M10 are on the optical table [17, 19].

For the best THz coupling efficiency, firstly the focus of the 12.5 inch (31.75 cm) end mirror is located at the beam waist in the THz-TDS system shown in Fig. 2-1b. Then the total extra round trip path distance of 170.46 m, is chosen to be precisely equal 51 times of round-trips of the ultrafast optical pulses with a laser pulse round-trip distance of 334 cm.

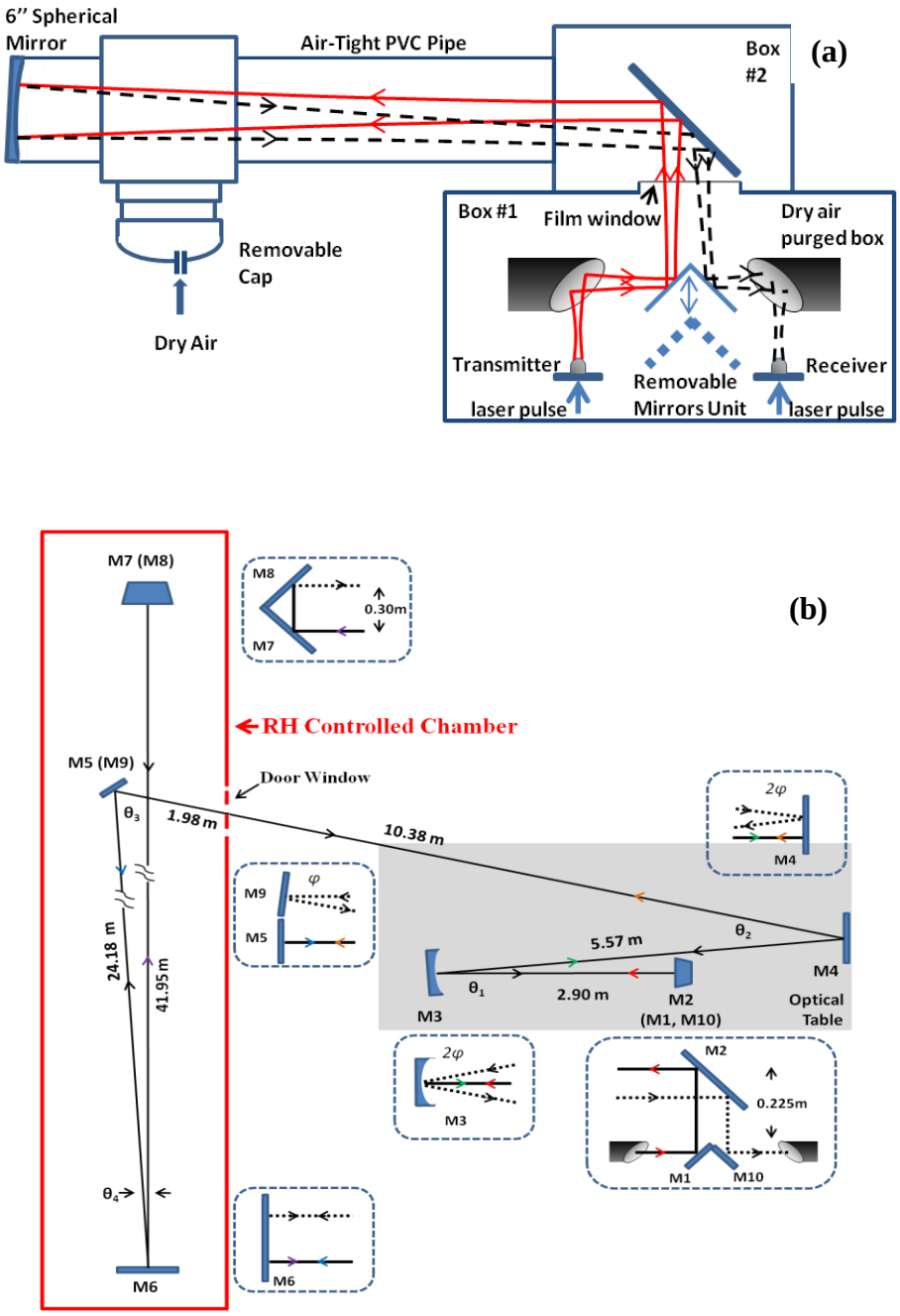

Fig.2-2. (a) Diagram of the sealed long-tube system with round-trip length of 6.18m. (Figure adapted from Ref. [16]). (b) Top (x-z plane) view of the 170 m long-path set-up with the sample chamber outlined (left red rectangle). (Figure adapted from Ref. [19])

2.2.4 RH Controlled Sample Chamber

In addition, we transform the 43.1 m long connecting hallway with the THz laboratory, as shown by the red rectangle in Fig. 2-2b, into a relative humidity (RH) controlled sample chamber, by semi-permanently sealing the ceiling with plastic sheet by magnet button and temporarily sealing the air-vents, lights, and lab-doors with plastic sheet and tape. This RH controlled sample chamber gives a 137 m round-trip THz path within the 170 m path, which allowed us to measure the transit time of the sharp leading edge of the reshaped THz pulses, as a function of the controllable humidity inside the chamber.

The THz beam passes into and out of this chamber, through a 12.5 μm thin plastic film window in the lab doorway. The humidity in the sample chamber can be stabilized and increased as much as RH 30% from the ambient laboratory value, by 8 humidifiers and four 16 liter water heaters distributed uniformly along the hallway, while two large fans circulate the air during measurements. Hygrometers, located at both ends of the chamber and on the optical table, are used to measure RH and temperature. Moreover, with relative long life time of sample chamber, small molecules vapor sample and diffusive medium, such as fog and smoke, can be added into chamber for different purposes of study.

2.2.5 Laser Clock Drift and Thermal Drift Problem

Using the synchronization between the laser clock and the total extended THz path requires extremely stable laser cavity and the long-tube/path setup. In our 170 m long-path measurement, a slow drift of the measured pulse of approximately 0.6 ps/hour was observed, which is caused by both the laser-clock drift and the slow drift of the length of the 170.46 m long THz optical train [17, 19].

The approximate 0.6 ps/hour drift corresponds to a 180 μm/hour change in the THz long-path length compared to the corresponding length of 51 laser round-trips. Because the thermal

drift is quite slow compared to a THz pulse scan measurement that requires only 3 minutes, it is possible to numerically align a series of pulse measurements for time-domain averaging.

The repetition (clock) rate of the Ti-Sapphire Mode-locked laser is measured as 89.6948xx MHz, which corresponds to a delay between pulses of 11.148918 ns and a spatial separation of 3.342446 m. The optical clock rate is quite stable to six digits, and the frequency drift and some jitter occur in the last 2 digits, as indicated by the x. Over the course of an experiment, there are slow changes in the optical clock rate of the order of 100 Hz, causing a difference in the total long-path clock delay of 0.63 ps, which is almost equal to our observed drift of 0.6 ps/hour of the measured transmitted THz pulse [17].

For the slow drift of the long-path length, a 149 m-long part of the 170.46 m optical train are directed by large mirrors on heavy mounts supported by the thick floating-slab concrete floor of the basement laboratory, which is influenced by the thermal effect of massive concrete floor of the building. The other 21.5 m-long part of the THz optical train is directed by mirrors supported on the stainless steel (SS) optical table. The massive concrete floor is considered to respond very slowly, on the order of many hours or days, to average temperature changes, while the temperature response of the SS table is much faster. It is important to note that stainless steel and concrete have approximately the same coefficient of thermal expansion 10^{-5} $(\Delta L/L)/^{\circ}C$. Consequently, if the difference temperature ΔT changed by 1 ^{o}C, a length difference of 170 m x 10^{-5} would occur, with the corresponding change in the start time of the THz pulse of 5.7 ps. This time change is approximately equal to the observed day to day and week to week changes. In the following chapters, we will demonstrate that both of the clock drift and the thermal drift are not a problem for our measurements and data analysis based on our experimental results.

2.3 System Capability

Based on the experimental results, the following physical characteristics of measured THz pulses provide enough information for us to analyze different aspect of tested samples:

1. THz signal spectra attenuation and resonant absorption;

2. THz signal reshaping in time domain;

3. THz signal arrival time delay;

The first characteristic is associated with the resonant absorption lines of water vapor or molecule vapor, the water vapor continuum absorption at THz transparent windows, and the broad band scattering loss by suspended particles. The second characteristic is used to investigate the phase shift and corresponding group velocity dispersion of the resonant lines. The third characteristic is related to the change of atmospheric refractivity which is linearly proportional to the water vapor density.

In the following chapters, we investigate these physical characteristics of the atmosphere and provide a comprehensive theory model including all of these phenomena, which have very good agreement with experimental results. We also experimentally demonstrate the potential application of THz-TDS remote detection of small molecule vapors based on all of these characteristics.

CHAPTER III

RESONANT ABSORPTION LINES OF ATMOSPHERIC WATER VAPOR

Firstly, the experimental results of the 6.68 m Long-Tube and the 170 m Long-Path are presented. Then, we study the van-Vleck Weisskopf (vV-W) model of absorption and phase for water vapor [20, 24], which can be used to fit our absorption and refractivity measurements. Moreover, the proper formats of vV-W function are derived to be compatible with professional spectroscopic databases [18].

Secondly, we fit our long-tube/path experiment results with the vV-W line shape function and JPL database [18]. The good agreement between the calculated THz output pulse and the measured output pulse with the same THz outgoing pulse is presented.

Thirdly, based on the good quality of the theoretical fitting, we have calculated the transmitted THz pulses through the atmosphere at a specified humidity for the longer distances of 500, 1000 and 2000 m, and two potential wireless communication channels are observed after 2000 m of propagation [18]. We proposed two ideal digital channels based on the linear dispersion theory [21]. It is noteworthy that the vV-W model is sufficient for a qualitative simulation for longer distance propagation, although it is not as precise as the MRT theory that will be introduced in the next Chapter.

.

3.1 The Preliminary Experimental Results of Long-Tube and Long-Path System

3.1.1 6.68 m Long Tube System

Firstly, we start from the precise coherent THz-TDS measurement of the amplitude transmission through the atmosphere with a corresponding accuracy of better than ± 10 dB/km from 0.2 to 2 THz for power transmission.

The measurement procedures are almost same for the two systems: Firstly, system operation and stability are checked by measuring performance of the THz-TDS system with the coupling mirrors removed. Secondly, with the coupling mirrors are re-installed, several THz reference pulses, transmitted through the sample chamber with background RH for Long-Path system (filled with dry air in PVC pipe for Long-Tube system), are measured. Thirdly, after adding tested samples (water vapor/small molecule vapor/fog) into the sample chamber (PVC pipe in Long-Tube case), several Long-Path/Tube THz sample pulses are measured. Then, again the reference pulses are measured. This sequence is repeated several times during the complete transmission measurement.

Since there are 50 cm path enclosed in box #1 with dry air filled all the time, the results are the measurement of a 6.18 m path of the atmosphere at 21 ^{o}C and relative humidity (RH) 51% [16]. Two transmitted electric field pulse are measured: the reference pulse with dry air at less than RH 0.5% in the sample pipe and the sample pulse with the pipe filled with room air and water vapor at RH 51%, illustrated as top and bottom traces in Fig. 3-1a respectively. Figure 3-1b shows the corresponding amplitude spectra of these pulses. The reference spectrum weakly shows the strong water lines, indicating that the residual water vapor in the sample space was less than RH 0.5%. In contrast, the sample spectrum shows complete absorption for the strong water lines.

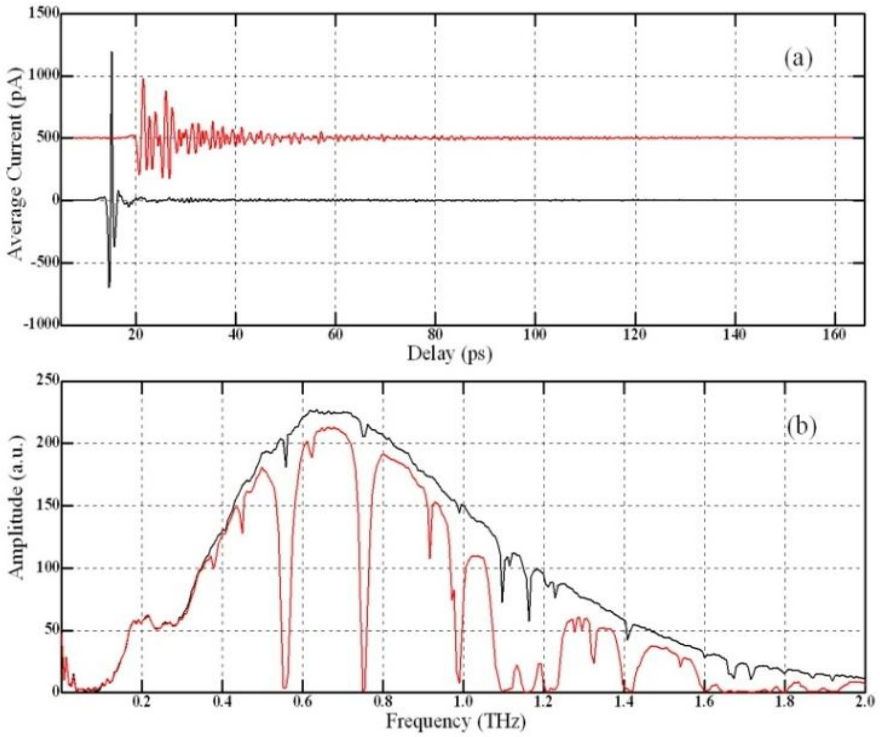

Fig. 3-1. Long-Tube results: (a). Measured THz reference pulse (lower trace) and measured THz sample pulse (upper trace). (b). Corresponding amplitude spectrum (upper curve) for the THz reference pulse and the sample pulse (lower curve). (Figure adapted from Ref. [16])

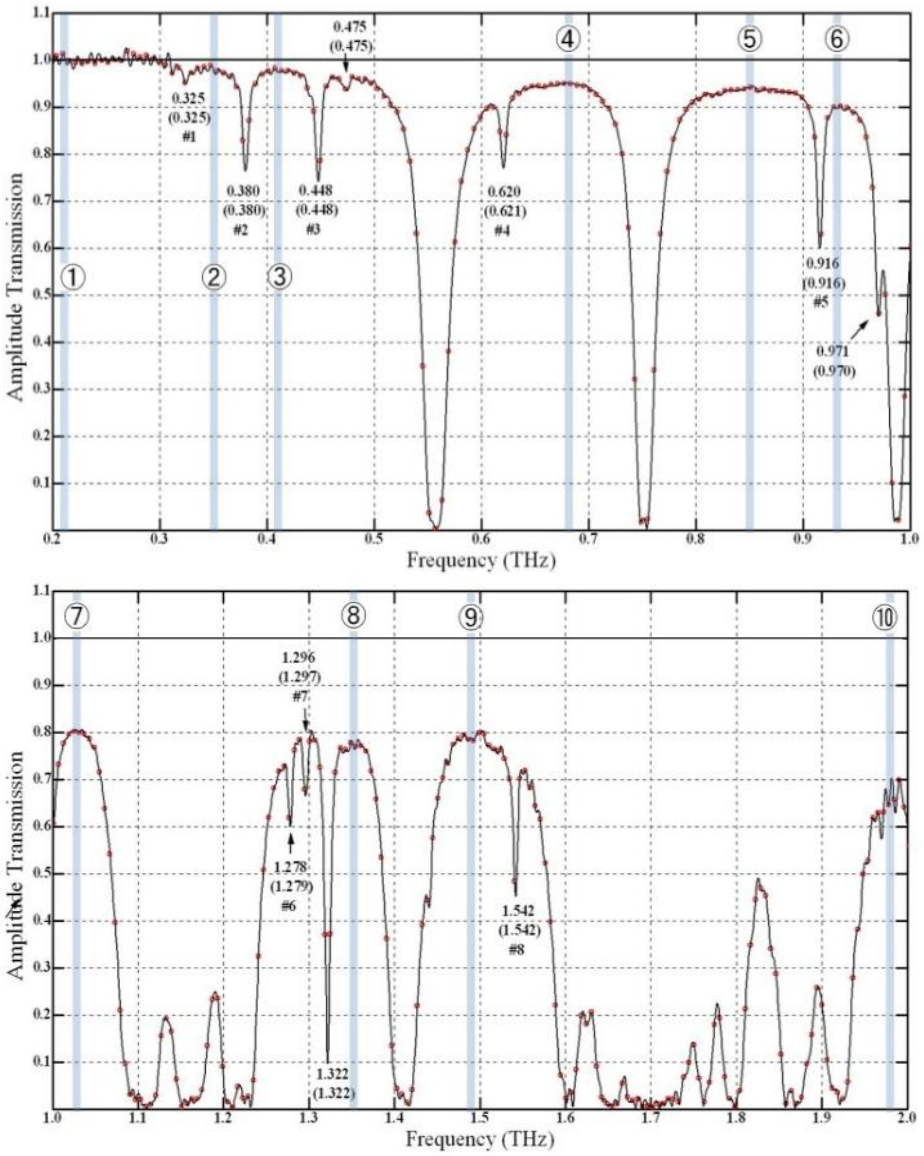

Fig. 3-2. The amplitude transmission through 6.18 m of atmosphere at 21 ℃ with RH 51%. 10 water windows (circled numbers) and 8 weak water lines are marked. (Figure adapted from Ref. [16])

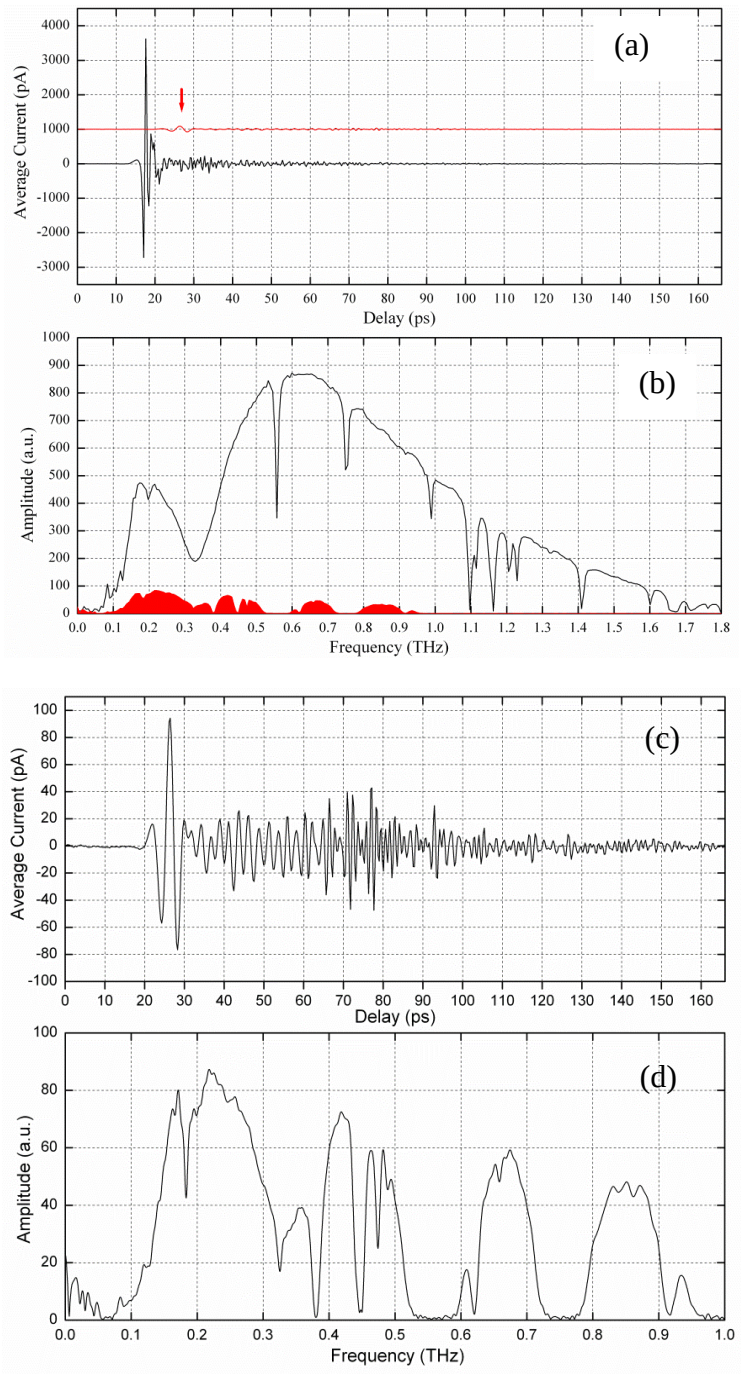

Fig.3-3. (a) The free space signal of standard THz-TDS system and the output transmitted THz pulse after 170 m propagation. (b) Corresponding amplitude spectrum of (a). (c) The output transmitted THz pulses in (a). (d) Corresponding amplitude spectrum of (c). (adapted from Ref. [17])

The amplitude transmission shown in Fig. 3-2 is the ratio of the sample spectrum to the reference spectrum of Fig. 3-1a. For this result the real data points are indicated by the larger open circles separated from each other by 6.1 GHz, and the interpolated points obtained from the zero-padding are separated from each other by 0.61 GHz and define the solid line. The weaker water lines appear with their expected frequencies, strengths and with linewidths equal to the spectral resolution of 6.1 GHz. The central frequency of the measured water lines was determined to an accuracy of ± 1 GHz as indicated on Fig. 3-2. The frequency in parenthesis is the accepted handbook value.

3.1.2 170 m Long-Path System

Then the experimental results of the long-path THz setup are shown as Fig. 3-3 [17]. The Fig. 3-3a compares the averaged outgoing pulse to the averaged incoming pulse. The outgoing pulse is the same reference signal in long tube experiment shown in Fig. 3-1, when the outgoing pulse is coupled to the long 170 m path in lab air with RH 51% at 21 ^{o}C. The incoming pulse shows very strong and extended ringing from the rotational lines of water vapor as shown in Fig. 3-3c.

The comparison of the averaged outgoing and incoming amplitude spectra is shown in Fig. 3-3b. The incoming spectrum shows complete absorption bands for the strong water lines and the significant appearance of the very weak water lines at their handbook frequencies to a precision of 1 GHz and with resolution limited linewidths. The spectral windows in Fig. 3-3d illustrates the THz potential applications for ranging, imaging, communications and sensing in the range of a few hundred meters [1, 2].

3.2 Resonant Absorption Line Theory

The complex Fourier transform of the output THz pulse $E(z, \omega)$ can be calculated by using the reference pulse $E(0, \omega)$ as follows

$$E(z,\omega) = E(0,\omega)\cdot e^{i\Delta k(\omega)z}\cdot e^{-\alpha(\omega)z/2}. \tag{3-1}$$

where α(ω) and Δk(ω) are frequency-dependent absorption coefficient and phase shift of the unit distance, respectively. Then the corresponding THz incoming pulse in time domain can be retrieved by taking the inverse numerical Fast Fourier transform (IFFT) of the output frequency components E(z, ω). So it is important to find the correct expression of α(ω) and Δk(ω) for water vapor absorption lines.

3.2.1 van Vleck-Weisskopf (vV-W) Theory

The van-Vleck Weisskopf model (vV-W) was derived by van-Vleck and Weisskopf from the standard Lorentz oscillator theory [20], and the vV-W model has been proved to be more accurate than the Full Lorentz and Gross models for water vapor [25]. The classical oscillator theory expression of α(ω) and Δk(ω) for single resonant absorption line are given by Eqs. (17) and (18) in the original vV-W paper [20], and are given below:

$$\alpha = \frac{2\pi Ne^2}{mc}\left(\frac{\omega}{\omega_0}\right)^2\left[\frac{1/\tau}{(\omega-\omega_0)^2+(1/\tau)^2}+\frac{1/\tau}{(\omega+\omega_0)^2+(1/\tau)^2}\right]. \tag{3-2a}$$

$$n^2-1 = \frac{4\pi Ne^2}{m(\omega_0^2-\omega^2)}\left[1-\frac{(\omega/\omega_0)+(\omega/\omega_0)^2}{2\tau^2\left[(\omega-\omega_0)^2+(1/\tau)^2\right]}+\frac{(\omega/\omega_0)-(\omega/\omega_0)^2}{2\tau^2\left[(\omega+\omega_0)^2+(1/\tau)^2\right]}\right]. \tag{3-2b}$$

where ω is the angular frequency, ω_0 is the line center angular frequency, τ is the mean time interval between collisions and $1/\tau=\Delta\omega_0/2$, which denotes the full-width half-maximum (FWHM) linewidth. The relationship between α(ω) and Δk(ω)is shown in Fig. 3-4.

In order to calculate α(ω) and Δk(ω) for all of the water vapor lines within THz range, the values of the line intensity, line width, and line center frequency for each line are needed, and can be found from professional spectroscopic databases.

In the JPL database the absorption coefficient $\alpha_j(\omega)$ of water vapor resonant line can be written as the product of a line intensity I_j (with units of nm^2 MHz) and a lineshape function $f(\omega, \omega_j)$ [9, 18]:

$$\alpha_j(\omega) = N_{H2O} \cdot I_j(\omega) \cdot f(\omega, \omega_j). \tag{3-3}$$

where N_{H2O} is the number density of water vapor in molecules / (cm nm^2), and ω_j is the water vapor resonant line center frequency in MHz, j refers to the water vapor resonance line.

The absorption coefficient equation in the HITRAN database has the same format [10] as,

$$\alpha_j(\tilde{\omega}) = N^*_{H_2O} \cdot S_j(\tilde{\omega}) \cdot f(\tilde{\omega}, \tilde{\omega}_j). \tag{3-4}$$

where $N^*_{H_2O}$ is the number density of water vapor in molecules/(cm^3), S_j is the intensity (with units of cm^{-1}/(molecules/cm^2) in HITRAN database) and $\tilde{\omega}_j$ is the water vapor resonant line center wavenumber in cm^{-1}. Note that S_j can be converted to I_j by $S_j = I_j / (c \cdot 10^{10})$ where c is the speed of light in vacuum with units of m/s [10]. For both the JPL and the HITRAN databases, the total absorption coefficient is the sum of all of individual water vapor absorption lines by using the line-by-line summation method as $\alpha = \sum_j \alpha_j$.

3.2.2 Line Intensity and vV-W Line Shape Function

Because line intensity is given by database, so if the Eq. (3-2a) can be rewritten in the same format of Eq. (3-3) to determine the corresponding expression of the vV-W line shape function, we can calculate water vapor absorption line, for all lines within THz range.

Firstly, after converting the classic oscillator expression to the general quantum-mechanical system and the factor e^2/m to $8\pi^2 v_j \left|\mu_{ba}^2\right|/3h$, (b and a in this quantum-mechanical expression denote the excited and ground states respectively, of the transition ω_j), where μ_{ba} is the corresponding dipole moment matrix element [20, 24, 26], we rewrite the Eq. (3-2a) as

$$\alpha_j = N\left[\frac{2\pi}{3ckT}\cdot\frac{\omega_j^2\left|\mu_{ba}\right|^2(2J+1)e^{-E_{ja}/kT}}{\sum_{j,J}(2J+1)e^{-E_{ja}/kT}}\right]\cdot\left(\frac{\omega}{\omega_j}\right)^2\left[\frac{2/\tau}{\left(\omega-\omega_j\right)^2+\left(1/\tau\right)^2}+\frac{2/\tau}{\left(\omega+\omega_j\right)^2+\left(1/\tau\right)^2}\right]. \tag{3-5}$$

Then, the line intensity I_j in Eq. (3) in the JPL database [9] is defined as below:

$$I_{ba}\left(T\right)=\left(\frac{4\pi^2}{3hc}\right)\cdot\frac{\omega_{ba}\,{}^{x}S_{ba}\mu_x^2\left[e^{-E_{ja}/kT}-e^{-E_{jb}/kT}\right]}{Q_{rs}}. \tag{3-6}$$

for $\omega_{ba}=\omega_j$, ${}^{x}S_{ba}\mu_x^2=\left(2J+1\right)\mu_{ba}^2$ according to Eq. (4-28) in [24], and the rotational-spin partition function $Q_{rs}=\sum_{j,J}(2J+1)e^{-E_{ja}/kT}$ [9, 24]. Using these relationships and the approximation: $1-e^{-\left(E_{jb}-E_{ja}\right)/kT}\approx\hbar\omega_j/kT$, for $\hbar\omega_j<<kT$, we can rewrite Eq. (3-6) as

$$I_j=\left(\frac{2\pi}{3ckT}\right)\cdot\frac{\omega_j^2\left|\mu_{ba}\right|^2(2J+1)e^{-E_{ja}/kT}}{\sum_{j,J}(2J+1)e^{-E_{ja}/kT}}. \tag{3-7}$$

which is identical to the line intensity I_j in the first brackets of Eq. (3-5).

In Eq. (3-5), the rest part after the line intensity can be treated as the vV-W lineshape function which is given as:

$$f_1\left(\omega,\omega_j\right)=\left(\frac{\omega}{\omega_j}\right)^2\cdot\left(\frac{\Delta\omega_j}{\left(\omega-\omega_j\right)^2+\left(\Delta\omega_j/2\right)^2}+\frac{\Delta\omega_j}{\left(\omega+\omega_j\right)^2+\left(\Delta\omega_j/2\right)^2}\right). \tag{3-8}$$

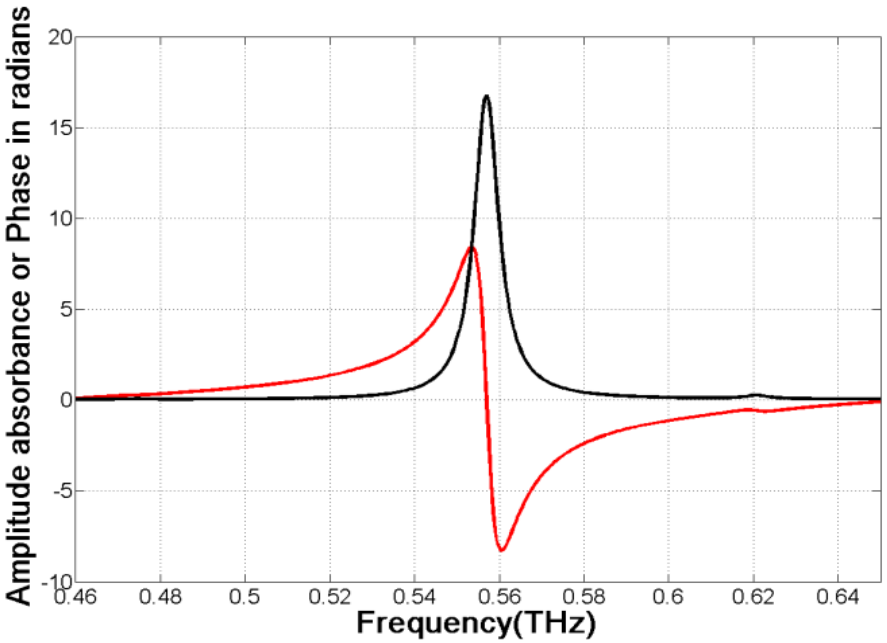

Fig. 3-4. vV-W amplitude absorbance (upper curve) and the corresponding phase shift in radians (lower curve) based on Eqs. (3-2a) and (3-2b), with 7 GHz FWHM linewidth. (Figure adapted from Reference [17])

where $\Delta\omega_j$ is the line full-width at half-maximum, ω_j is line center frequency. For each line, $\Delta\omega_j$ can be obtained as $\Delta\omega_j = 2\gamma_{ks}P_W + 2\gamma_{kf}P_A$ with γ_{ks} and γ_{kf} are the self and foreign gas line broadening coefficients, P_W and P_A are the water vapor partial pressure and the foreign gas partial pressures in the atmosphere.[27].

Finally, the absorption coefficient $\alpha(\omega)$ and the phase shift $\Delta k(\omega)$ of water vapor shown as Eqs. (3-2a) and (3-2b) can be rewritten as [18]

$$\alpha(\omega) = D \cdot \sum_j \frac{A_j}{\pi}\left(\frac{\omega}{\omega_j}\right)^2 \cdot \left[\frac{\Delta\omega_j}{(\omega-\omega_j)^2 + (\Delta\omega_j/2)^2} + \frac{\Delta\omega_j}{(\omega+\omega_j)^2 + (\Delta\omega_j/2)^2}\right]. \tag{3-9a}$$

$$\Delta k(\omega) = D \cdot \sum_j 2\frac{A_j}{\pi\omega_j}\left(\frac{\omega\omega_j}{\omega_j^2-\omega^2}\right)\left[1 - \frac{\Delta\omega_j^2}{8\omega_j}\left(\frac{\omega}{\omega_j}\right)\right.$$
$$\left.\cdot\left(\frac{\omega_j+\omega}{(\omega_j-\omega)^2 + (\Delta\omega_j/2)^2} - \frac{\omega_j-\omega}{(\omega_j+\omega)^2 + (\Delta\omega_j/2)^2}\right)\right] \tag{3-9b}$$

for which

$$\left(n(\omega)-1\right) = \Delta k(\omega)\lambda_0 / 2\pi. \tag{3-10}$$

and
$$D = 10^{-18} \cdot \pi \cdot N, \tag{3-11}$$

with N equal to the number of molecules per cubic meter, to give $\alpha(\omega)$ in units of inverse meters. Now, we obtain the expression of $\alpha(\omega)$ and $\Delta k(\omega)$, which is compatible with the JPL and HITRAN database, and will compare this model with our experimental results.

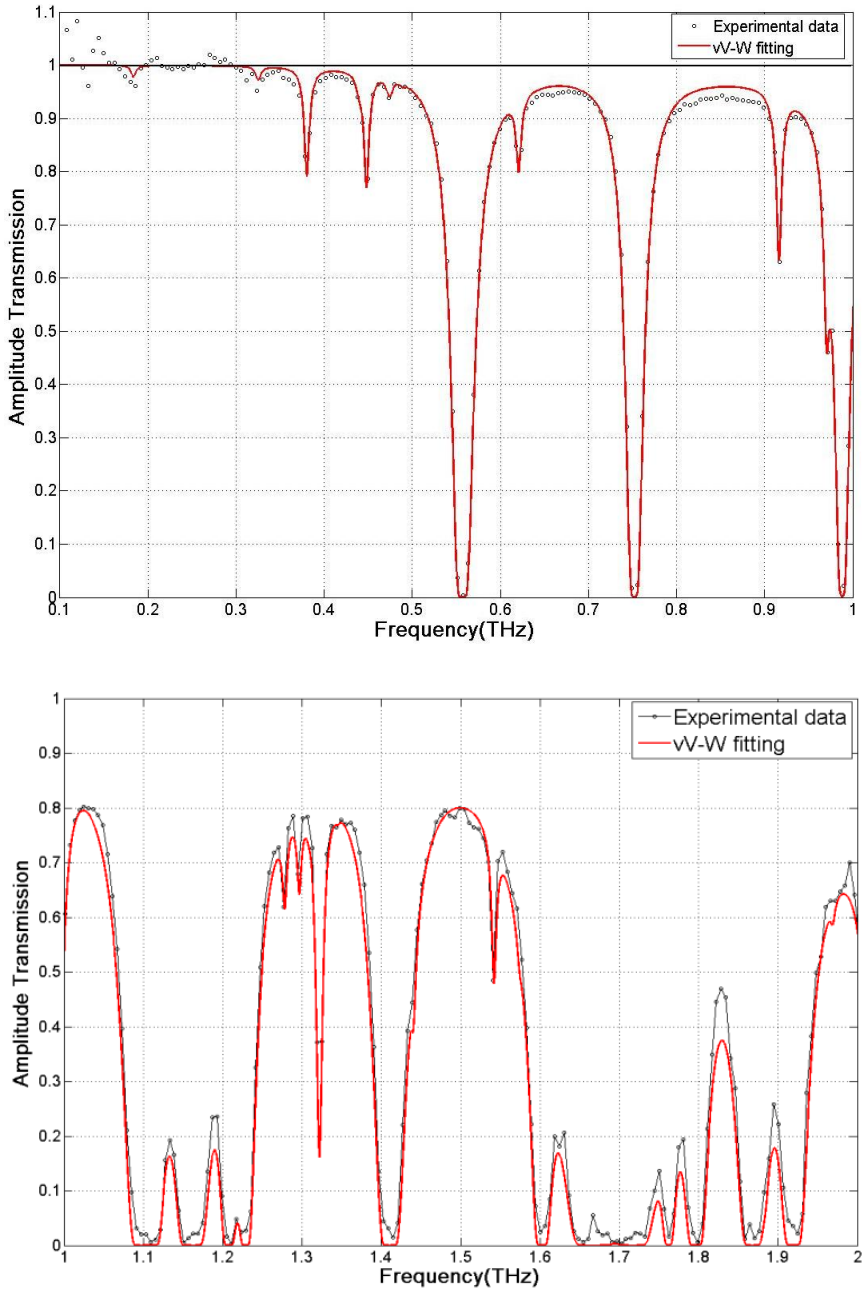

Fig. 3-5. The vV-W amplitude transmission compared to the experimental measurements of Fig. 3-2. (Figure adapted from Ref. [18])

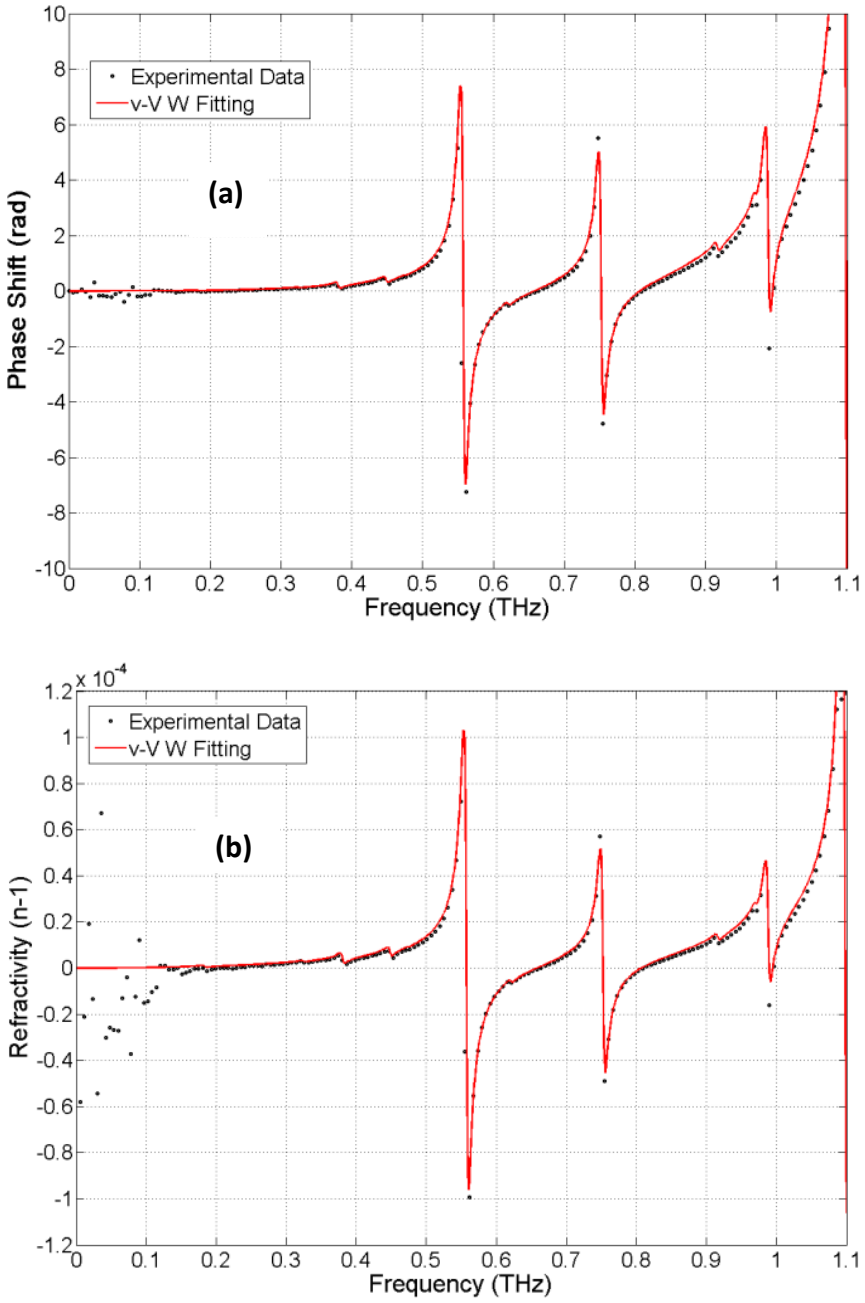

Fig. 3-6. (a). Calculated phase $\varphi = \Delta kL$ (solid line) and measured phase (dots) for transmission through 6.18 m of atmosphere at 21 ℃ with RH 51%. (b). Refractivity $(n(\omega) - 1)$ obtained from Eq.(3-10) and results of (a). (Figure adapted from Ref. [18])

3.2.3 Time Domain Pulse Calculation

From these fittings of the absorption coefficient $\alpha(\omega)$ and phase $\Delta k(\omega)$ to the vV-W lineshapes, we calculate the frequency components of the transmitted pulse through the water vapor in the sample chamber by using Eq. (3-1). Then the corresponding THz incoming pulse in time domain is obtained by taking the Inverse Fast Fourier Transform (IFFT) of the incoming frequency components.

Firstly, for the 6.68 m long-tube experimental result, by using the calculated $\alpha(\omega)$ and $\Delta k(\omega)$ shown in Figs. 3-5 and 3-6, the calculated time domain pulse modulations based on the IFFT of Eq. (3-1) are quite similar with the experimental signal shown in Fig. 3-7 [18]. This good agreement of vV-W model shows the ability to calculate the propagated THz pulses through longer and various RH levels atmosphere.

Then we examined the previous investigation of short, broadband THz pulse propagation in the atmosphere a distance of 170 m [18]. Firstly, the THz pulses measured in relative low RH conditions are used as the reference outgoing signals for long path calculations. Figure 3-8 shows the data set from a recent experiment for a 137 m path with relatively good system stability for measurements at 21 ^{o}C and RH 10.5% as the reference signal (top trace) and RH 46.5% as the sample signal (second top trace). These two measurements were used to test the accuracy of the longer path calculated incoming pulses, as shown in Fig. 3-8a. The incoming pulses from both calculations show good agreement with each other and the experiment. Consequently, we can extend our calculations to longer lengths with reasonable confidence in their tested accuracy.

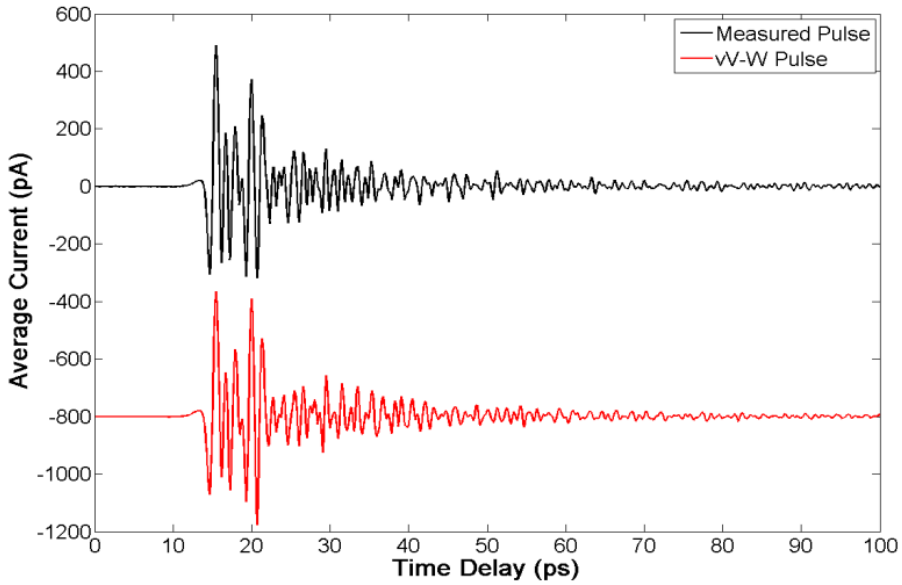

Fig. 3-7. The measured transmitted THz pulse of Fig. 3-1a (upper trace) is compared to the calculated THz pulse with z = 6.18 m (lower trace). (Figure adapted from Ref. [18])

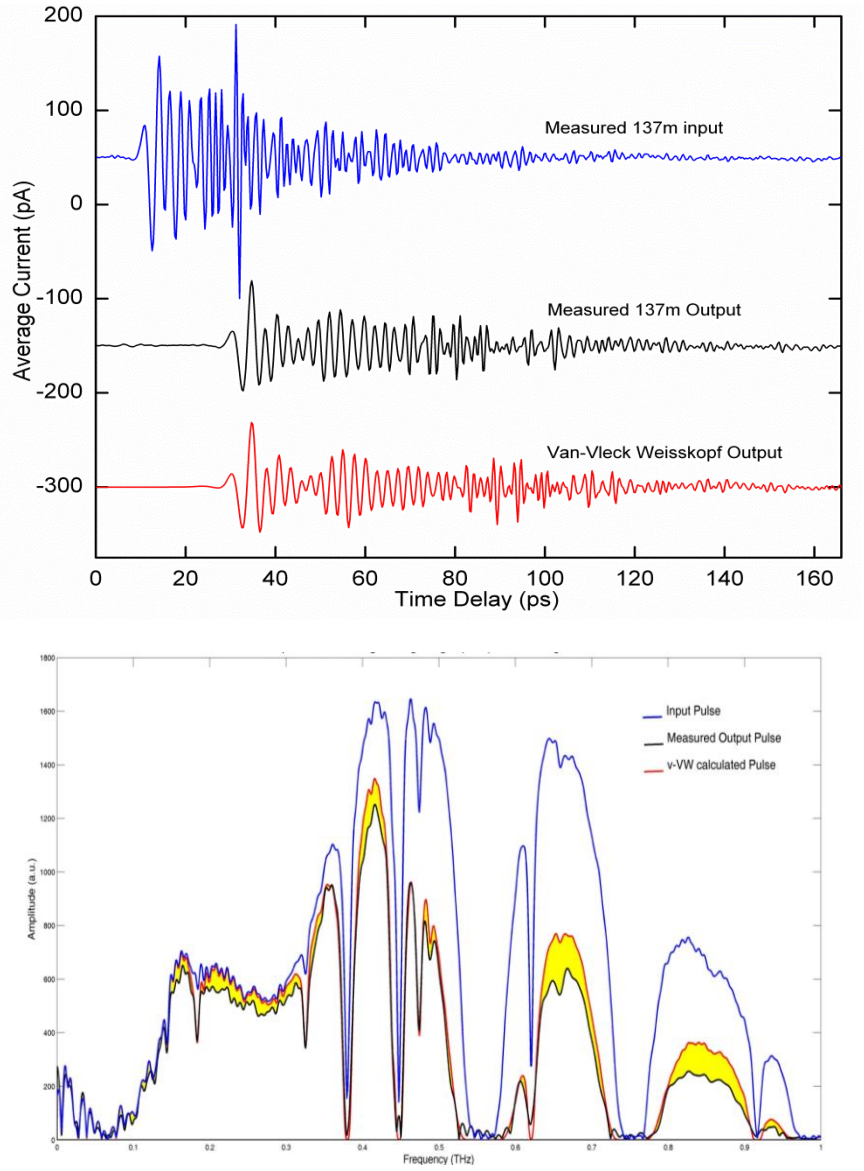

Fig. 3-8. (a) Measured incoming pulse for 1.9 g/m^3 (outgoing pulse), the measured incoming pulse for 8.5 g/m^3, and the calculated incoming pulse using the RH 10.5% pulse as outgoing and calculating the propagation through 137 m at RH (46.5%-10.5%), using the vV-W calculation. (b). Corresponding amplitude spectra. (Figure adapted from Ref. [18])

3.2.4 Mismatched Absorption Problem

The accuracy of the results given above is acceptable for our initial calculations of pulse propagation with a path length of 6.18 m, but for much longer propagation distances of 170 m, or hundreds of meters, the discrepancy between the observed and calculated absorption in the windows of transparency (minimum absorption) below 1 THz can become a problem as shown in Fig. 3-8b. The phenomenon behind this problem is the poorly understood continuum absorption of water vapor, which is especially important in the transparent windows, will be investigated in the next chapter.

3.3 Longer Path Prediction

Next, we will test the predicted range of the THz bit pulse and the incoming pulse propagated through 170 m with the relative low RH 10.5% is used as the outgoing pulse to calculate the longer path lengths of 100 m and longer at RH 51% at 21 ^{o}C [18]. These calculations assume perfect coupling and use the absorption and dispersion (phase) given by Eqs. (3-9a) and (3-9b), without considering the influence of oxygen in atmosphere.

The consequent THz incoming pulses are shown in Fig. 3-9a, together with the 170 m reference outgoing THz pulse. The THz bit pulse shape changes and broadens with the additional propagation, while the higher frequency ringing is significantly attenuated. However, it remains clear that the THz bit pulse structure is capable of digital transmission for distances of the order of 300 m.

Figure 3-9c presents much longer path propagation results of 500 m, 1000 m, and 2000 m at RH 51% at 21 ^{o}C, with the same low RH outgoing pulse. Figure 3-9d shows the corresponding amplitude spectra.

It is noteworthy that the predicted pulses are within the sensitivity range of our coherent system based on the realistic estimate of the simple expansion of a spherical wave of the actual received signal strength. This additional attenuation factor of the amplitude spectrum is simply the ratio of 170/(170 + L), where L is the additional path length. Corresponding attenuation factors are 0.250, 0.143, 0.077 for the additional path lengths of 500, 1000 and 2000 m, respectively. For the measured outgoing pulse the signal to noise ratio is 200, indicating a receiver sensitivity of 1 pA. The peak to peak signal of the 2000 m signal is 50 pA and after multiplication by spherical wave factor is 3.8 pA, which would be observable with S/N ratio of 4.

3.3.1 Observed Wireless Communication Windows

A careful study of the transmitted THz pulses through 170 m of humid air and longer distance has revealed the THz bit pulse for digital (binary) communications which is composed of the two stable, naturally-bounded windows located at 0.07-0.37 THz as the potential communication carrier bands channels I and II as shown in Fig. 3-9e and 3-9f [18, 21]. The outgoing pulse is the top trace shown in Fig. 3-9e and numerically IFFT calculated from the experimental RH 50% amplitude spectrum between 0.07 and 0.37 THz of Fig. 3-9a, assuming that all of the frequency components are in phase.

The results in Fig. 3-9f show that during the propagation of the THz-bit pulse, the pulse appears to be separating into two independent pulses. A successful test of this concept is shown in Fig. 3-10 for which the original THz bit pulse, is considered to be the overlap of THz bit pulse I and THz bit pulse II. The natural boundary of the water line at 0.184 THz separates the spectra of the two pulses, and the natural boundary of the water line at 0.326 THz defines the high frequency boundary of pulse-II. The low-frequency boundary of pulse-I at 0.128 THz is determined by the spectral response of the THz receiver, slightly above the weak oxygen line at 0.12 THz.

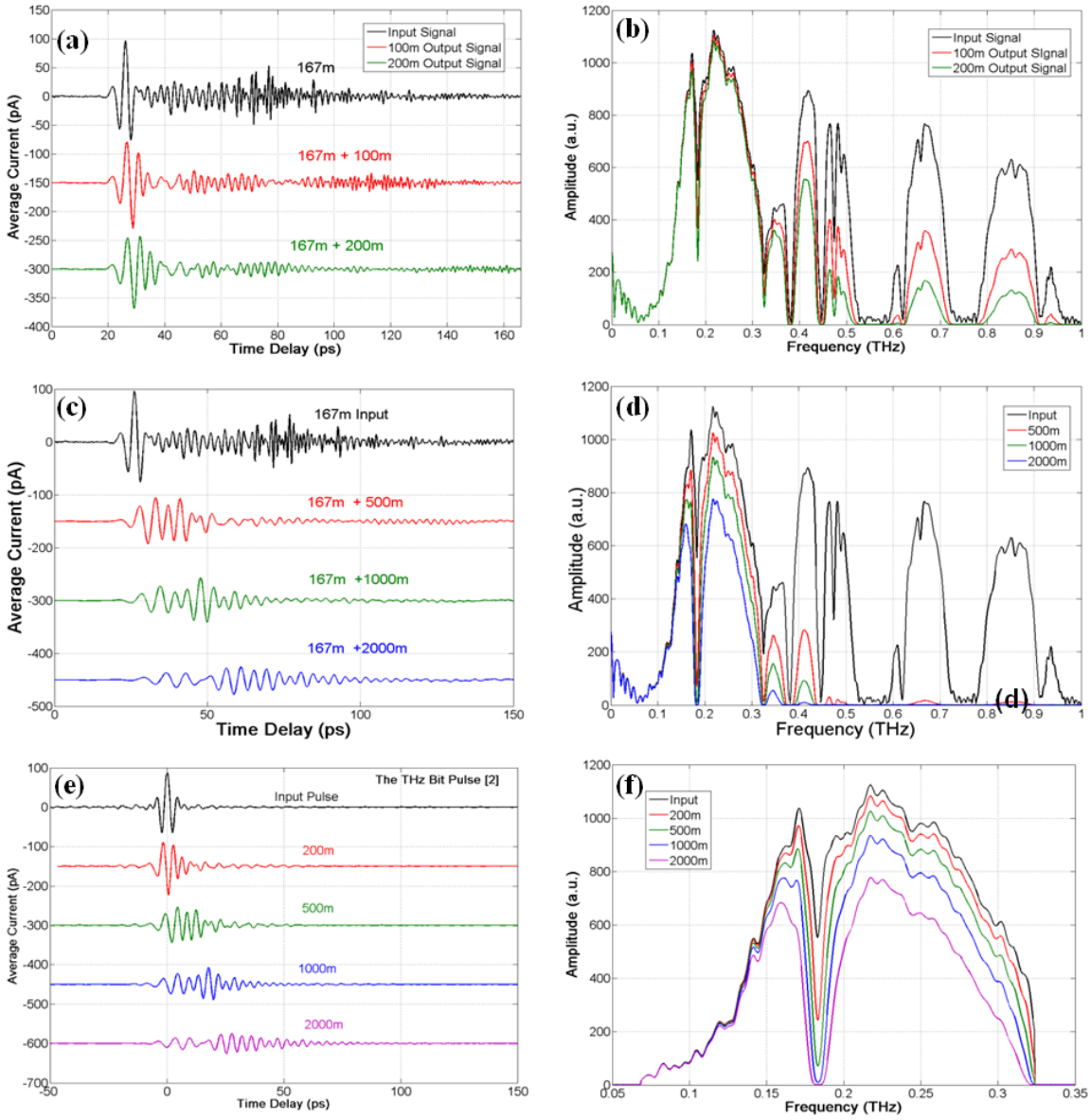

Fig. 3-9. (a) 167 m outgoing signal with propagated pulses after 100m, 200m of vV-W calculated propagation. (b) Corresponding amplitude spectra. (c) 167 m outgoing signal with propagated pulses after 500 m, 1000 m and 2000 m of vV-W calculated propagation. (d) Corresponding amplitude spectra. (e) The calculated vV-W propagation of the phase coherent THz-bit pulse [17]. (f). Corresponding amplitude spectra. (Figure adapted from Ref. [18])

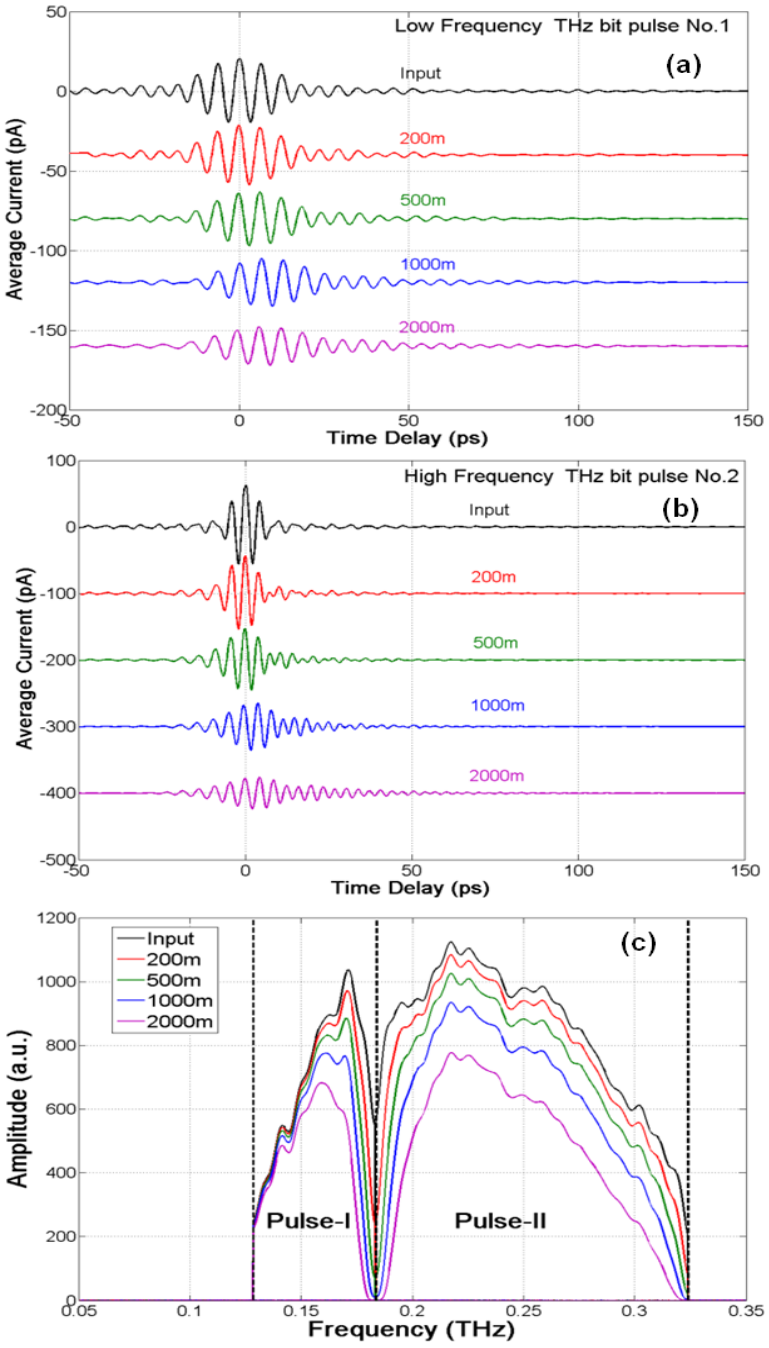

Fig.3-10. (a) Calculated vV-W propagation of the Low-Frequency THz-bit pulse I. (b) Propagation of the High-Frequency THz-bit pulse II. (c) Amplitude spectra of the THz-bit pulses I and II (Figure adapted from Ref. [18]).

From the propagation results shown in Fig. 3-10a for the THz–bit pulse 1, it is reasonable to consider a bit stream of these pulses separated from each other by 100 ps, corresponding to the bit rate of 10 Gb/s. And we can obtain the bit rate distance product of 20 (Gb/s)-km for 2 km propagation. Similarly, for the propagation results shown in Fig. 3-10b for the THz bit pulse 2, consider a bit stream of these pulses separated from each other by 50 ps, corresponding to the bit rate of 20 Gb/s, giving a bit rate distance product of 40 (Gb/s)-km for 2 km propagation [21].

3.3.2 Proposed Ideal Wireless Communication Channels

The results in Figs.3-9 and 3-10 show that the calculated propagated THz-bit pulse based on our THz long path setup outgoing pulse, appears to be separating into two independent bit pulses I and II, which corresponding to frequency bands of 0.13 – 0.18 THz, and 0.19 – 0.33 THz. Two weak water vapor absorption lines at 0.184 THz and 0.326 THz act as the natural boundaries. The low-frequency boundary of pulse-I at 0.13 THz is determined by the spectral response of the THz receiver, slightly above the weak oxygen line at 0.12 THz.

Here, we have proposed two ideal THz wireless communication channels I and II spectra centered on 95 and 250 GHz with FWHM bandwidths of 30 GHz, and 50 GHz respectively highlighted in Fig. 3-11, based on vV-W model of Eqs. (3-9a) and (3-9b), and the linear dispersion theory calculations using all knowledge to date concerning the atmosphere of water vapor, oxygen and water vapor continuum absorption [21].

As shown in Fig. 3-11, Channels I and II are defined by natural boundaries. Channel I starts with the strong O_2 lines at 60 GHz and extends to the 183 GHz water vapor resonance line; Channel II extends from 183 GHz to the 325 GHz water line. Moreover, the Channel I has significantly less absorption, less dispersion, and less group velocity dispersion (GVD) than Channel II. Consequently, the Channel I pulses are chosen as the lower frequency, lower bit rate, and longer ground link, while the Channel II pulses as the higher frequency, higher bit rate,

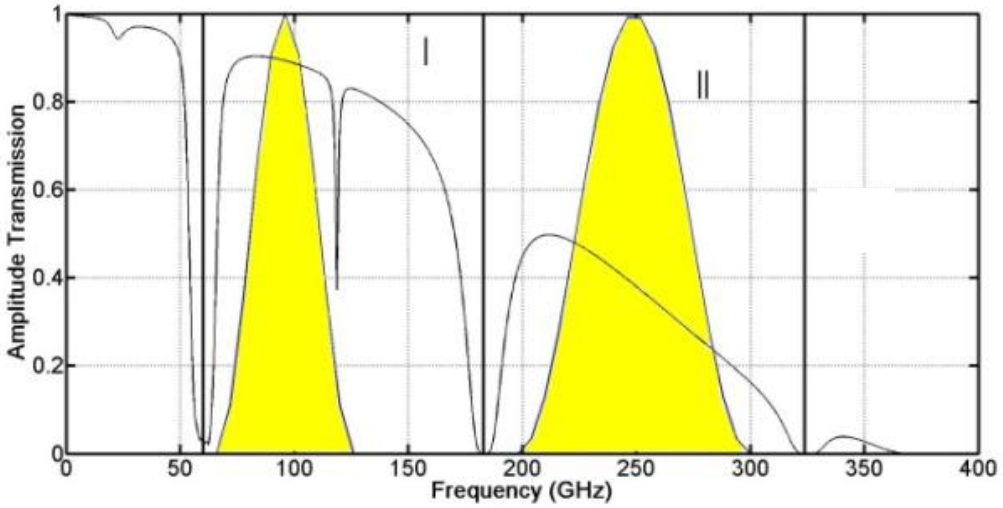

Fig. 3-11. Calculated amplitude transmission for a 2 km length of water vapor at RH 58% and 20 °C (10g/m^3) with O_2 vapor and proposed two THz lines (Figure adapted from Ref. [21])

satellite link, with a shorter integrated zenith path through the atmosphere.

A direct 95 GHz, 20 km ground link at 9.5 Gb/s would have a power loss of 10 dB due to water vapor at RH 58% (10 g/m^3) and 20 ^oC and O_2 absorption, and a diffraction loss of 26 dB for 2 m dia. antennas. A direct 250 GHz, 35,800 km geosynchronous satellite link at 20.8 Gb/s would have a 2 km (equivalent to the zenith integration) water vapor loss of 9 dB and a diffraction loss of 65 dB with 5 m ground and 2 m satellite antennas.

CHAPTER IV

WATER VAPOR DENSITY RELATED ATMOSPHERIC REFRACTIVITY

In this chapter, firstly we report the measurements of the essentially frequency independent refractivity of water vapor from 0.1 to 1 THz, independent of the simultaneous strong THz pulse broadening and absorption [19]. The humidity dependent transit time of THz pulses through the 170 m round trip path Long-Path system was measured to a precision of 0.1 ps.

Then, we show the convergence between Debye Oscillator Theory and the van-Vleck Weisskopf Theory at zero frequency, which leads to the conclusion that the refractivity of water vapor calculated by the van-Vleck Weisskopf theory via a summation over all the water lines from 22.2 GHz to 30 THz can explain all of the previous measurements from 0.5 MHz to microwave, mm-waves and THz frequencies [15]. This result removes a long standing absorption discrepancy in comparisons of measurements and theory, and is in excellent agreement with experiments [19].

4.1 Experiments of Water Vapor Refractivity within THz Range

In Fig.4-1a, the transmitted THz pulses for the reference (RH 22.23%), the first wet sample (RH 43.01%) and the second wet sample (RH 58.42%) are shown with actual transit times. The dashed lines mark the corresponding first minimums at 18.15 ps, 29.63 ps, and 37.63 ps. The corresponding amplitude spectra of three pulses are shown in Fig. 4-1b [19]. The sample

pulses show arrival time delays of 11.5 ps and 19.5 ps, respectively compared to the reference pulse, due to the higher RH in the chamber. Based on the respective temperature and RH, the absolute water vapor density can be calculated to determine the corresponding frequency independent refractive index of water vapor.

The measurements of the arrival times of the first ascending at zero crossing of the received THz pulses on different days, as a function of the different RH are shown in Fig. 4-2a. The straight lines show a linear dependence on the chamber RH. These parallel lines (measured on different days) show the repeatability of the entire system and the chamber. All of the measurements presented in Fig. 4-2b are contained within the dashed curves with the slopes of 6.42 ps/(RH 10%) and 5.26 ps/(RH 10%), where the best fitting curve has the slope of 5.84 ps/(RH 10%), with a standard deviation of 1.40.

It is noteworthy that the pulse delays at a specified RH change of the order of 5 ps from week to week because of the small changes in the long path delay with respect to the laser clock and thermal drift of concrete and steel. However, from the experimental results, for a long-time period (several tens of minuets), the stable transit times for several continuous scans in a series show the stability of the optical train of the long-path setup. For a short-time period (< 3 min), the center frequencies of measured weak water vapor absorption line in the Fourier-transformed frequency spectra shown in Figs. 4-1b, agree with the HITRAN and the JPL database to an accuracy of 1 GHz, which indicates no significant laser-clock drift.

The frequency-independent refractivity is determined from the relationship $\Delta t = (n_0 - 1)L/c$, where L = 137 m (round trip distance in sample chamber) and c is the free-space light speed. From this relationship and the measured slope of 5.84 $\pm$ 10% ps/(RH 10%) at 21 ℃ shown in Fig. 4-2b, we obtain (n_0 -1) = 70 x 10^{-6} $\pm$ 10% for the measured frequency-independent refractivity of water vapor at 21 ℃ and 10 g/m^3, over the frequency band from 0.10 THz to 0.95 THz, which is consistent with 61 x 10^{-6} for the early 9.2, 24 and 72 GHz measurements water

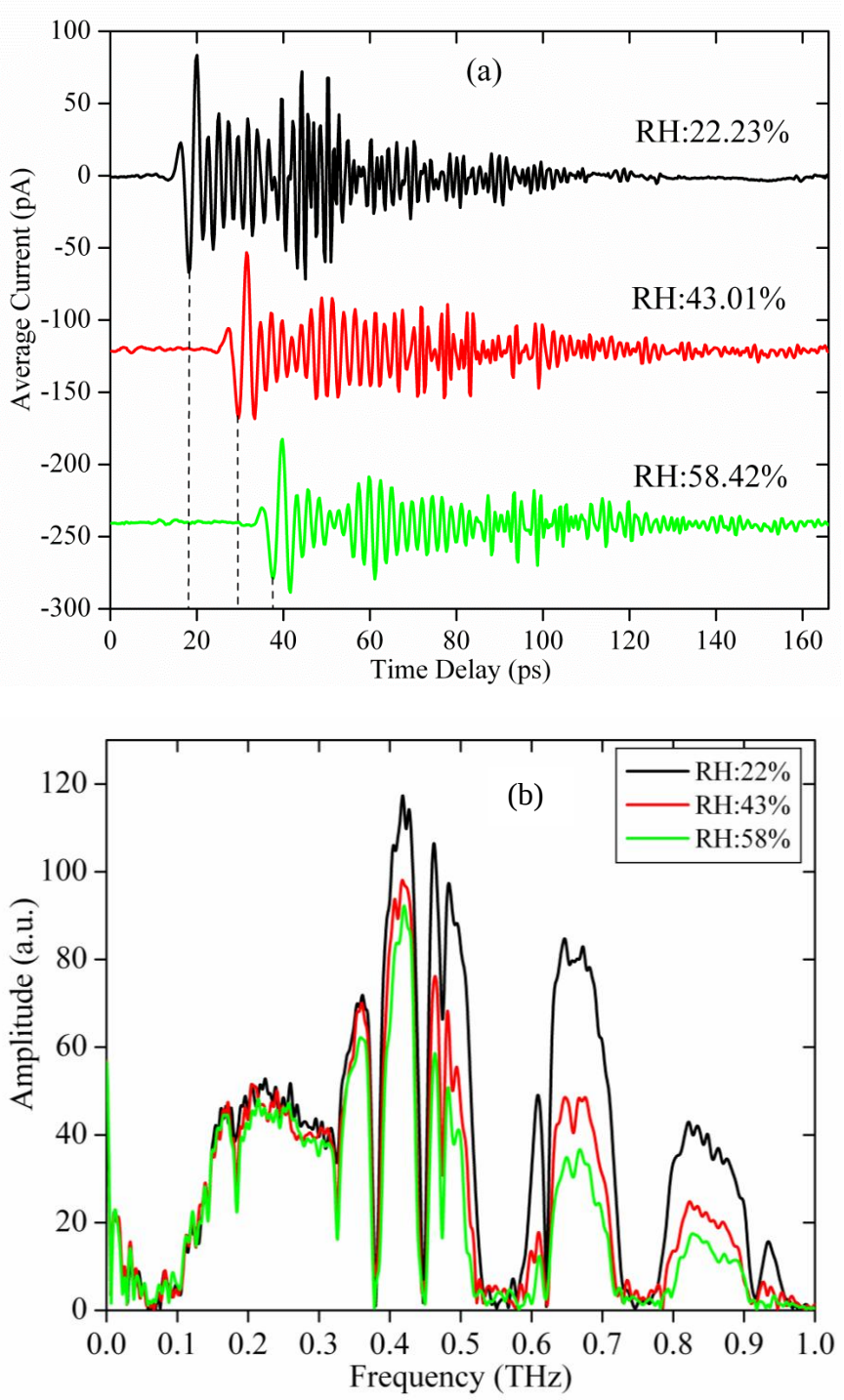

Fig. 4-1 (a) Three measured transmitted THz pulses (top) RH 22.23%, (middle) RH 43.01%, (bottom) RH 58.42%. (b) Corresponding amplitude spectra. (Figure adapted from Ref. [19])

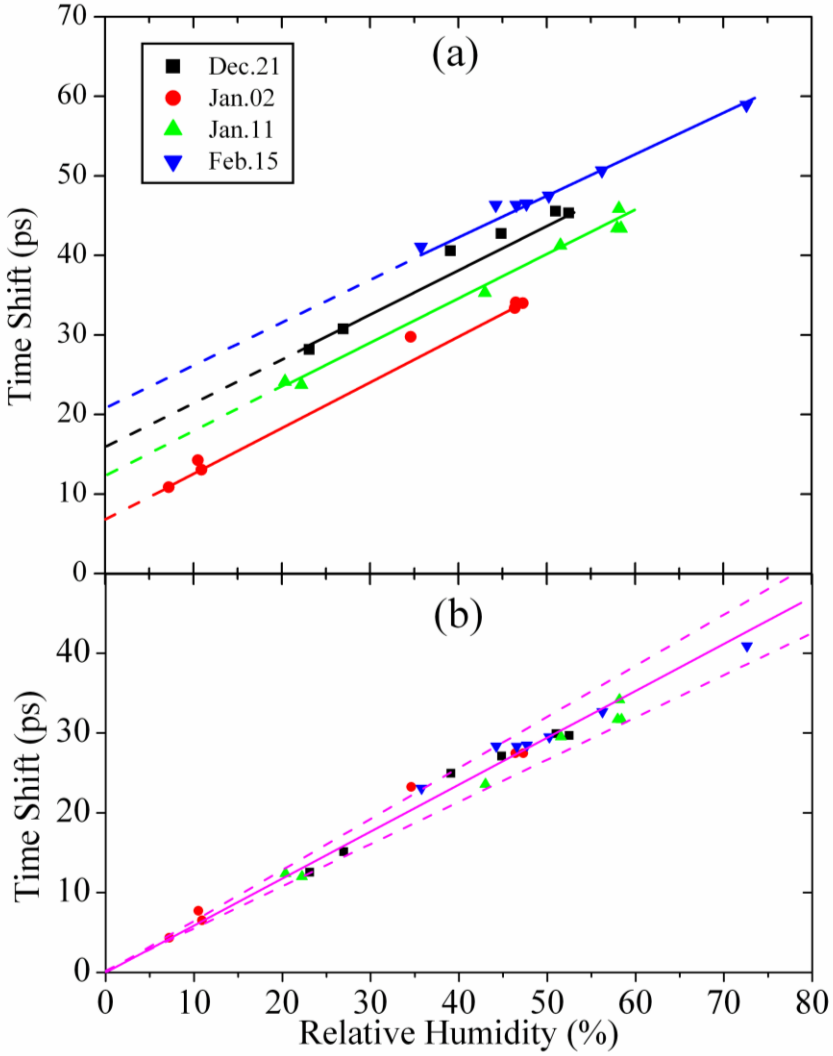

Fig. 4-2. (a) The measured pulse time-shift vs RH at 21 ℃ for four independent measurements. (b) Replot of the data and extended lines of (a), with the time delay at zero RH subtracted from the data series. (Figure adapted from Ref. [19])

vapor density of 9.9 g/m^3 [28-30]. This dry air component remains constant during our measurements, which are only sensitive to the changing refractivity of water vapor.

4.2 Microwave and MM-Wave Debye Theory Approach

4.2.1 Debye Theory

Previously, the low-frequency experimental results up to 100 GHz have been understood in terms of the Debye theory for a molecular vapor of permanent electric dipoles [22, 31]. For low frequencies, the Debye theory dipole polarization of the vapor of water molecules will be in thermal equilibrium with an applied electric field with the frequency-dependent, complex Debye refractivity of [20, 22, 24, 31],

$$\tilde{n}_D(\omega) - 1 = \left(\frac{2\pi N \mu^2}{3kT} \right) \Big/ \left(1 + i\omega\tau\right) \tag{4-1}$$

where N is the number of molecules per cubic centimeter, μ is the permanent dipole moment of the water molecule, k is the Boltzmann constant, T is the absolute temperature, ω is the applied angular frequency and τ is the relaxation time required for the external field-induced orientations of the molecules to return to a random distribution after the field is removed. (Note, this mathematical dependence is the same as for Drude theory of electrical conductivity [32]). Eq. (4-1) can be rewritten in the form below to enable simple comparison with the measurements

$$\tilde{n}_D(\omega) - 1 = \frac{n_0(0) - 1}{1 + i\omega\tau} \tag{4-2}$$

where $n_0(0) - 1$ is the Debye refractivity at zero frequency. The Debye refractivity can be rewritten in terms of the real and imaginary parts as

$$\tilde{n}_D(\omega) - 1 = \frac{\left[n_0(0) - 1\right]}{1 + (\omega\tau)^2} - i \cdot \frac{\left[n_0(0) - 1\right] \cdot \omega\tau}{1 + (\omega\tau)^2} \tag{4-3}$$

Initially, we are concerned with the real part of the Debye refractivity $[n_0(0) - 1]/ [1 + (\omega\tau)2]$, which falls off from the zero frequency as a Lorentzian with the half-width of $\omega_{1/2}\tau = 1$, equivalent to $f_{1/2} = 1/(2\pi\tau)$, where f is frequency. The Debye refractivity at zero frequency, $(n_o(0) - 1)$ can be directly calculated from Eq. (4-4) as [19],

$$n_0(0) - 1 = \frac{2\pi N \mu^2}{3kT} \tag{4-4}$$

using the following parameters; water vapor density of 10 g/cm^3 at 20 ^{o}C (T = 293 K), corresponding to N = 3.344 x 10^{17}/cm^3 ; μ = 1.85 Debye = 1.85 x 10^{-18} StatC-cm; and k = 1.38 x 10^{-16} g (cm/s)^2 . Evaluation of Eq. (4-4) with the above parameters gives the value of $n_0(0) - 1$ = 59.3 x 10^{-6}, in good agreement with previous low-frequency measurements [28-30] with $n_o(0) - 1$ = 61 x 10^{-6}.

4.2.2 Inconsistent Debye Power Absorption

Similarly, the Debye power absorption coefficient is obtained from the product of $2\omega/c$ and the imaginary part of the Debye refractivity in Eq. (4-3) [19],

$$\alpha_D(\omega) = 2\left(\frac{\omega}{c}\right) \cdot \frac{[n_0(0) - 1] \cdot \omega\tau}{1 + (\omega\tau)^2} \tag{4-5}$$

Consequently, the Debye broad-band absorption over this same range must be smaller than the observed water vapor absorption due to the previously discussed continuum absorption [11, 33], in order to provide a self-consistent understanding of the previous measurements. For our conditions of $(n_o(0) - 1) = 70 \times 10^{-6}$, and with $f_{1/2}$ = 2.0 THz, at 1 THz we obtain $\alpha_D(\omega)$ = 1.17/m equivalent to 5.1 dB/m = 5100 dB/km, which is impossibly large compared to our experiments with longer paths [18]. With respect to the continuum curve on Fig. 1 in [16], the calculated $\alpha_D(\omega)$ is approximately 230 times too large at 1 THz and 190 times too large at 0.3 THz.

The unusual absorption lineshape $\alpha_D(\omega)$ of the Debye response starts from zero at zero frequency and initially increases quadratically with frequency, but when $\omega\tau$ becomes greater than 1, monotonically approaches the constant high-frequency limit α_D(limit) [19], given below

$$\alpha_D\left(limit\right) = 2\frac{n_0\left(0\right)-1}{\left(c\tau\right)} \tag{4-6}$$

For our example, $1/\tau = 2\pi$ x 2 THz, the α_D(limit) = 5.86/m = 25.4 dB/m which is equivalent to 25,400 dB/km and is many orders of magnitude higher than experiment.

These impossibly large values show the previous opinion for measurements up to 100 GHz, that the Debye response of the vapor of permanent electric dipoles was the cause of the refractive delay is physically incorrect. Thus, there must be other causes of this delay such as water dimers, and perhaps clusters [34]. However, the effects of dimers and clusters would be expected to increase as the molecular number density squared, and our measurements show a linear dependence. Another possibility would be that the far wings of the resonance lines are broader than predicted.

4.3 Relationship of vV-W theory and Debye theory

Here, we present the van-Vleck Weisskopf (vV-W) theory as the more physically correct theory for the refractivity, than Debye theory at zero frequency. Firstly, we show that the vV-W theory converges to Debye theory at zero frequency, and thereby, remove the fundamental absorption discrepancy between theory and experiment for microwave and THz propagation of electromagnetic waves through the atmospheric water vapor, which the Debye theory fail to explain.

Then, using both the JPL and HITRAN data bases and the accepted value of the dipole moment $\mu = 1.855$ Debye, to calculate $(n_0(0) - 1)$, the previous microwave experimental results can be explained, and the associated absorption agrees with the measurements.

4.3.1 Converge from vV-W Theory to Debye Theory

The van-Vleck Weisskopf resonant lineshape theory has been shown to converge to the Debye theory as the resonant frequency approaches zero [20, 24]. Firstly, for the vV-W theory and Eqs. (3-9a), (3-9b) and (3-10) in Chapter 3, in the limit as ω approaches zero, the absorption coefficient $\alpha(0)$ equals to zero, the phase $\Delta k(0)z$ equals to zero, and the refractivity at zero frequency due to the electric dipole moment of water is given by

$$\left(n(0)-1\right)_{v-VW} = c \cdot D \cdot \sum_j \frac{2I_j}{\pi \omega_j^2}. \tag{4-7}$$

where j refers to the water vapor resonance line with angular frequency ω_j, and I_j denotes the line strength [18]. This zero frequency term only causes a pulse time shift, and consequently, has no effect on the observed pulse reshaping.

We start from the Eqs (3-6) and (3-7) of line intensity I_j in quantum-mechanical theory. After converting frequency v_j to angular frequency ω_j, Eq. (3-7) can be rewritten as

$$I_j = C_j \cdot \omega_j^2. \tag{4-8}$$

And we can rewrite Eq. (4-7) as

$$\begin{aligned} \left(n(0)-1\right)_{v-VW} &= c \cdot D \cdot \sum_j \frac{2C_j}{\pi} \\ &= c \cdot D \cdot \sum_j \left(\frac{2}{\pi}\right) \cdot \left(\frac{2\pi}{3ckT}\right) \cdot \frac{\left|\mu_{ba}\right|^2 (2J+1) e^{-E_{ja}/kT}}{\sum_{j,J} (2J+1) e^{-E_{ja}/kT}}. \end{aligned} \tag{4-9}$$

The remarkable result of Eq. (4-9) shows that for $(n(0) -1)_{vV\text{-}W}$, below 2 THz, there is no ω_j dependence and no $\Delta\omega_j$ linewidth dependence, due to the line symmetry about zero frequency of the vV-W theory. This significant situation only holds in the region for which $h\nu_{ab} << kT$, which is equivalent to $\nu_{ab} << 6.2$ THz. Consequently, it is expected that this term is reduced for frequencies f above 2 THz.

Based on Eqs. (3-11), Eq. (4-9) can be reduced to [15]

$$\left(n(0)-1\right)_{v-VW} = N\left(\frac{4\pi}{3kT}\right)\cdot\sum_j \frac{\left|\mu_{ab}\right|^2 (2J+1)e^{-E_{ja}/kT}}{\sum_{j,J}(2J+1)e^{-E_{ja}/kT}}. \tag{4-10}$$

Townes and Schawlow write the fractional function fa in their Eq. (4-25) in [24] as,

$$f_a = \frac{(2J+1)e^{-E_{ja}/kT}}{\sum_{j,J}(2J+1)e^{-E_{ja}/kT}}. \tag{4-11}$$

which gives the fraction of the total number of molecules in the lower state of the two states of ω_j. We can rewrite Eq. (4-10) as,

$$\left(n(0)-1\right)_{v-VW} = N\left(\frac{4\pi}{3kT}\right)\sum_j \left|\mu_{ab}\right|^2 f_a. \tag{4-12}$$

for which μ_{ab} is the dipole moment between the upper "b" and the lower "a" of the transition ωj. This important result shows concisely the difference between the van-Vleck Weisskopf and Debye theories. If all the E_a are set equal to zero, thereby, setting all the rotational lower E_a states to zero, f_a becomes $f_a = 0.5$, as Eq. (13-20) in [24]. Using $f_a = 0.5$, Eq. (4-12) becomes [15]

$$\left[\left(n(0)-1\right)_{v-VW}\right]_{Limit} = N\left(\frac{2\pi}{3kT}\right)\sum_j {\mu_{ab}}^2. \tag{4-13}$$

Townes and Schawlow [24], and van-Vleck and Weisskopf [20] have shown that

$$\sum_j \mu_{ab}{}^2 = \mu^2. \tag{4-14}$$

Thereby allowing Eq. (4-13) to be rewritten as,

$$\left[(n(0)-1)_{v-VW}\right]_{Limit} = \frac{2\pi N\mu^2}{3kT}. \tag{4-15}$$

which is identical to the Debye result of Eq. (4-4) for a vapor of permanent dipoles, and for which we have converted to number density/cm^3.

We can obtain mathematical agreement with Debye theory, if we set the fractional functions to 0.5 in the mathematics describing our calculations, corresponding to eliminating the rotational response and the required uniform population of all the lower states to conform to the Debye theory, which would only be achieved for a temperature high enough so that E_a/kT is significantly less than one. This is due to the mathematical consistency with the Debye theory as discussed in the vV-W original paper, and as described by Townes and Schawlow. This consideration shows that for water vapor the low frequency Debye theory may be a good approximation, but it is not physically correct.

4.3.2 Water Molecule Dipole Moment Determination

The difference can be demonstrated by calculations $(n(0) -1)_D = 58.14 \times 10^{-6}$ and $(n(0) - 1)_{vV\text{-}W} = 56.59 \times 10^{-6}$ for the identical conditions and parameters: $\mu = 1.855$ Debye, $N = 3.340 \times 10^{17}$/cm^3, and T = 300 K. For this comparison, showing a difference of 2.56 %, which would be very important in a dipole moment determination.

The earlier experiments [28-30], assumed the validity of Debye theory, and then used the measured value of $(n_o(0) - 1)$ to calculate the magnitude of electric dipole moment of the water molecule $\mu = 1.839$ Debye. An alternative method to determine the dipole moment of water μ is

to measure the Stark splitting of the hyperfine lines in rotational states of H_2O lines, which is independent of water vapor molecules number density [35, 36]. The measured value of μ is equal to 1.855 Debye, which is considered to be the most accurate value and used in the both JPL and HITRAN data bases.

Consequently, we compare our vV-W calculation to their measured value of $(n(0) - 1)$ adjusted to be 61.6 x 10^{-6} for a water vapor density of 10 g/m^3 and temperature of 293 K. Calculating the vV-W zero-frequency refractivity for the same number density and using the JPL data base for T = 293 K, we obtain 58.04 x 10^{-6}, which must be multiplied by $(1 + б)$ with $б$ = 0.052 added to account for the atomic and electric response of the water molecule that is independent of the electric dipole moment [30], to give $(n(0) - 1) = (1 + б)\,(n(0) - 1)_{vV\text{-}W}$ = 61.06 x 10^{-6} in excellent agreement with measurement.

Figure 4-3 presents the complete vV-W refractivity of water vapor at 20 ^{o}C and 10 g/m^3, the entire frequency dependent $(n(\omega) - 1)_{vV\text{-}W} + б(n(0) - 1)_{vV\text{-}W}$ is shown from 0 to 1,100 GHz. Clearly, the use of Debye theory to describe microwave and mm-wave transmission measurements is not required. Excellent agreement is shown for the early measurements [28-30, 37], marked by the red circles.

As a check on our results, we have also calculated the zero-frequency refractivity with the HITRAN data base at 293 K, and obtained 57.92 x 10^{-6}. This is relatively close agreement, considering that the JPL unadjusted value of 58.04 x 10^{-6} at 293 K involved the summation of 3085 lines up to 30 THz, and that the HITRAN calculation involved the summation of 8678 lines up to 30 THz, and shows the consistency of these two data bases for water vapor.

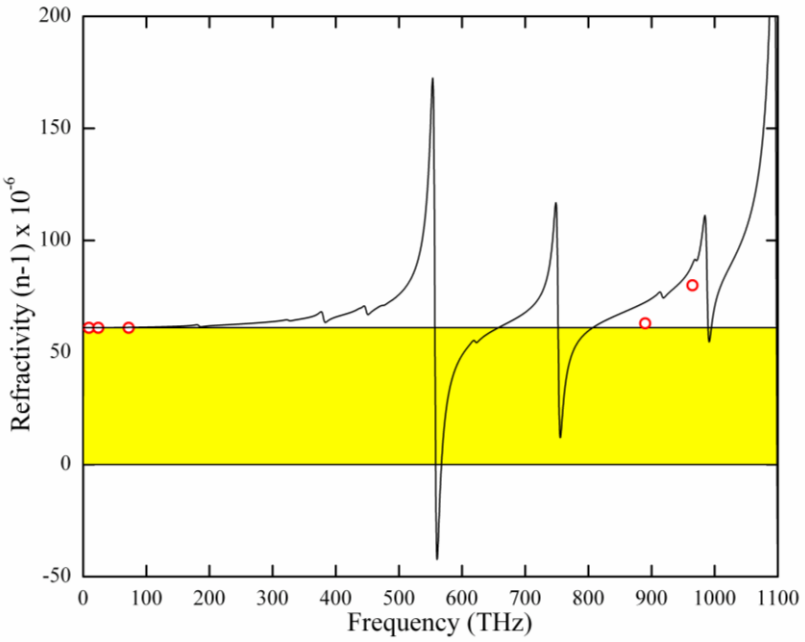

Fig. 4-3. Refractivity of water vapor at 20 ^{o}C and 10 g/m^{3}, calculated by the complete van-Vleck Weisskopf theory. The earlier measurements of are indicated by the open circles. The straight line at 61.06 x10^{-6} marks the complete calculated value of (n(0) -1). (Figure adapted from Ref. [15])

CHAPTER V

WATER VAPOR CONTINUUM ABSORPTION

The continuum absorption, which is defined as the difference between the measured absorption and the calculated resonance lines absorption, exists within those transparent windows over broad spectral range from the microwave to the infrared, and cannot be explained by the far-wing absorption of the resonant lines, as mentioned in the previous chapter. Many THz applications required a detailed knowledge of the measurements and theoretical prediction of the continuum absorption because the water vapor continuum absorption contributes more signal attenuation than resonant line absorption below 300 GHz.

Although numerous measurements have been performed in the infrared, only a few broadband experiments studied the THz range. Most of them have used the FTS technique, which bring a considerable amount of absorption from the adsorption layer of water on the reflector surfaces after many reflection. In this chapter, we will introduce the water vapor continuum absorption measurements based on the long path THz setup and compare the experimental results with empirical equations.

5.1 Introduction

The absorption mismatch problem mentioned in Chapter 3 is related to the water vapor continuum absorption which has a broadband discrepancy between the observed and calculated absorption within the windows of transparency (minimum absorption) below 1 THz as

shown in Fig. 3-8b.

As we mentioned before, the poorly understood continuum absorption is determined empirically and defined as the difference between the measured total absorption and contribution of resonant absorption lines [18]. It means that the measured amount of continuum absorption depends strongly on the lineshape function, number of lines, line intensities and line width chosen for line-by-line summation method.

It has been shown that the van Vleck-Weisskopf (vV-W) lineshape fits the resonant lines near their centers more accurately than the full Lorentz (FL) and Gross lineshapes [25]. Since then, in most of the literature the vV-W lineshape has been used to obtain the continuum absorption within the Millimeter wave [38-40] and THz regions [8, 27] under various humidity and temperature conditions. In Chapter 3, the van-Vleck Weisskopf line shape function was successfully applied for qualitatively analysis on THz pulses propagation and the corresponding reshapes.

However, the vV-W model has an unphysical constant value in far-wings, which will lead to a divergence of the lineshape integral over frequency. Firstly, a cutoff method for far-wings was introduced to solve this problem in the line-by-line summation calculation [39]. Although the cutoff frequency of 750 GHz has been used in many studies and is related to an assumed 1 ps “duration” of the molecular collisions, the resonant absorption is significantly understated in the far-wings. Then, the Molecular Response Theory (MRT) was introduced as a more physically correct model for the resonant lines, which includes the molecular orientation time during a collision.

With the precise water vapor resonant line model, the difference of absorption between experiments and resonance can be extracted, which is considered to be the continuum absorption. The corresponding empirical continuum absorption model was verified by experimental results with different reference humidity.

5.2 Resonant Absorption Lineshape Function

5.2.1 vV-W Model with Cutoff Frequency (vV-Wc)

The cutoff method was introduced to solve the problem of the unphysical far-wings of the vV-W lineshape in the line-by-line summation calculations [39], which is given by:

$$f_{cutoff}\left(\nu,\nu_j\right)=\frac{1}{\pi}\left(\frac{\nu}{\nu_j}\right)^2\cdot\left(\frac{\Delta\nu_j}{\left(\nu-\nu_j\right)^2+\Delta\nu_j^2}+\frac{\Delta\nu_j}{\left(\nu+\nu_j\right)^2+\Delta\nu_j^2}-\frac{2\Delta\nu_j}{\nu_{cut}{}^2+\Delta\nu_j^2}\right). \quad if\ \left|\nu-\nu_j\right|<\nu_{cut}$$
$$f_{cutoff}\left(\nu,\nu_j\right)=0. \quad if\ \left|\nu-\nu_j\right|\geq\nu_{cut} \tag{5-1}$$

where ν_{cut} is the cutoff frequency of 750 GHz in this work. Using the cutoff increases the calculated transmission of water vapor. However, Eq. (5-1) has a physical inconsistency, whereby the calculated value becomes negative for frequency differences from resonance, slightly smaller than the cutoff frequency. Consequently, we developed the straight-forward procedures given in Eqs. (5-2) and (5-3) to handle the cutoff and to eliminate this inconsistency [41].

For case 1, of Eq. (5-1) with $\nu_j<\nu$, we have

$$f_{cutoff}\left(\nu,\nu_j\right)=\frac{1}{\pi}\left(\frac{\nu}{\nu_j}\right)^2\cdot\left(\frac{\Delta\nu_j}{\left(\nu-\nu_j\right)^2+\Delta\nu_j^2}+\frac{\Delta\nu_j}{\left(\nu+\nu_j\right)^2+\Delta\nu_j^2}-\frac{\Delta\nu_j}{\nu_{cut}{}^2+\Delta\nu_j^2}-\frac{\Delta\nu_j}{\left(2\nu_j+\nu_{cut}\right)^2+\Delta\nu_j^2}\right). \tag{5-2}$$

for which $f_{cutoff}\left(\nu,\nu_j\right)=0.$, when $\nu_{cut}\leq(\nu-\nu_j)$

For case 2 , with $\nu<\nu_j$, we have

$$f_{cutoff}\left(\nu,\nu_j\right)=\frac{1}{\pi}\left(\frac{\nu}{\nu_j}\right)^2\cdot\left(\frac{\Delta\nu_j}{\left(\nu-\nu_j\right)^2+\Delta\nu_j^2}+\frac{\Delta\nu_j}{\left(\nu+\nu_j\right)^2+\Delta\nu_j^2}-\frac{\Delta\nu_j}{\nu_{cut}{}^2+\Delta\nu_j^2}-\frac{1}{\left(2\nu_j-\nu_{cut}\right)^2+\Delta\nu_j^2}\right) \tag{5-3}$$

for which $f_{cutoff}\left(\nu,\nu_j\right)=0.$, when $\nu_{cut}\leq(\nu_j-\nu)$

For case 3, with $\nu<\nu_j<\nu_{cut}$, we have $f_{cutoff}\left(\nu,\nu_j\right)=f_1\left(\nu,\nu_j\right)$.

5.2.2 Molecular Response Theory (MRT)

Recently, the Molecular Response Theory (MRT) lineshape has been developed, and well fit the resonant lines of methyl halide, which showed a smooth transition from the vV-W lineshape to the Lorentz lineshape [42]. Through a weighting factor, the MRT lineshape function smoothly changes from the van Vleck-Weisskopf (vV-W) lineshape [43] near the line center to the full Lorentz (FL) lineshape [43] at far wings of the resonance line. The MRT lineshape overcomes the disadvantage of the unphysical far-wing of the vV-W lineshape, as well as the underestimated absorption from the vV-W lineshape with a cutoff. Clearly, resonance absorption with a strictly defined lineshape function is needed for reliable and comparable values of the continuum absorption.

For the molecular response theory the absorption coefficient of a resonant line is given by [43],

$$\alpha_j^{MRT}(\nu) = S(\nu)\alpha_j^{vV-W}(\nu) + \left(1 - S(\nu)\right)\alpha_j^{L}(\nu). \tag{5-4}$$

for which $\alpha_j^{vV-W}(\nu)$ is the absorption coefficient with the vV-W lineshape function and $\alpha_j^{L}(\nu)$ is the absorption coefficient with the FL lineshape function. $S(\nu)$ is the MRT weighting function controlling the transition from the vV-W lineshape at low frequencies to the FL lineshape at higher frequencies. $S(\nu)$ is given simply by,

$$S(\nu) = 1 \Big/ \left[1 + (2\pi\nu\tau_c)^2\right]. \tag{5-5}$$

where τ_c is the collision parameter, considered to be a measure of the orientation time of molecules during a collision and expected to be much faster than the duration of a collision. The weighting function $S(\nu)$ monotonically changes from one to zero as the frequency increases, and S(ν) = 0.5 for $\nu_{1/2} = 1/(2\pi\tau_c)$ = 796 GHz for τ_c = 0.2 ps [42]. Consequently, for

$2\pi\nu\tau_c \ll 1$, $\alpha_j^{MRT}(\nu) \approx \alpha_j^{vV-W}(\nu)$, and for $2\pi\nu\tau_c \gg 1$, $\alpha_j^{MRT}(\nu) \approx \alpha_j^{L}(\nu)$. It is important to note that the MRT line, as defined in Eq. (5-2), will always be between the FL and the vV-W lines. Only the half-width at half-maximum Δv_j linewidths of the vV-W and FL lineshapes remain as parameters, and these are calculated by HITRAN as $\Delta v_j = \gamma_{ks} P_s + \gamma_{kf} P_f$ with γ_{ks} and γ_{kf} are the self and foreign gas line broadening coefficients [10].

As shown in Fig. 5-1, v-VWc model underestimated the absorption and MRT model approach provide a more precise value. This is more clearly demonstrated in Fig. 5-2 by absorption line comparison for a single resonance line normalized to unity with center frequency at 1.0. The vV-W (dashed line), FL (dotted line), MRT (red line between vV-W and FL lines) with τ_c = 0.2 ps, and the vV-Wc (dash-dot line) with the cut-off at 1.75 THz (750 GHz from line center) are plotted in Fig. 5-2. All lineshapes have (HWHM) linewidth of 3.15 GHz.

5.2.3 Empirical Continuum Absorption Equation

The empirical equation of the continuum absorption α_c has two components: one part is proportional to the square of the water vapor partial pressure P_W; the other part is proportional to the product of P_W and the total of the foreign gas partial pressures in the atmosphere P_A. For the quantitative analysis of the measured continuum absorption the following empirical parameterization can be rewritten as [12, 38]:

$$\alpha_c(\nu, 294K) = \nu^2 \left[C_W^* \cdot \rho_W^2 + C_A^* \cdot \rho_A \cdot \rho_W \right]. \tag{5-6}$$

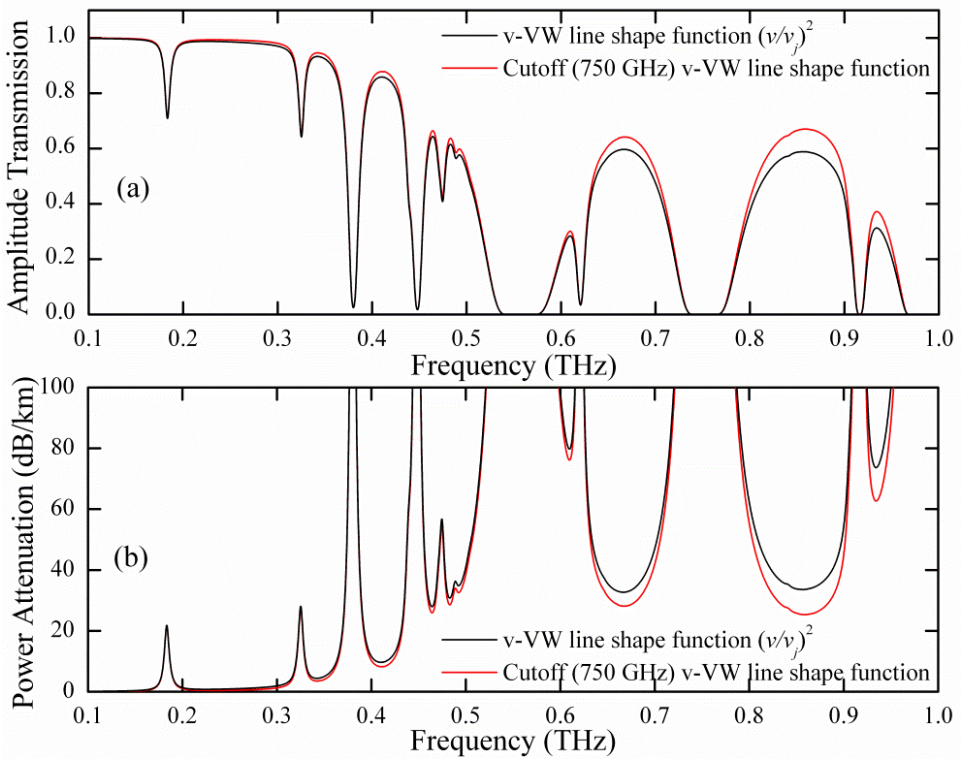

Fig. 5-1. (a) Amplitude transmission comparison between vV-W, vV-Wc. (b) Corresponding power attenuation in dB/km. (Figure adapted from Ref.[41])

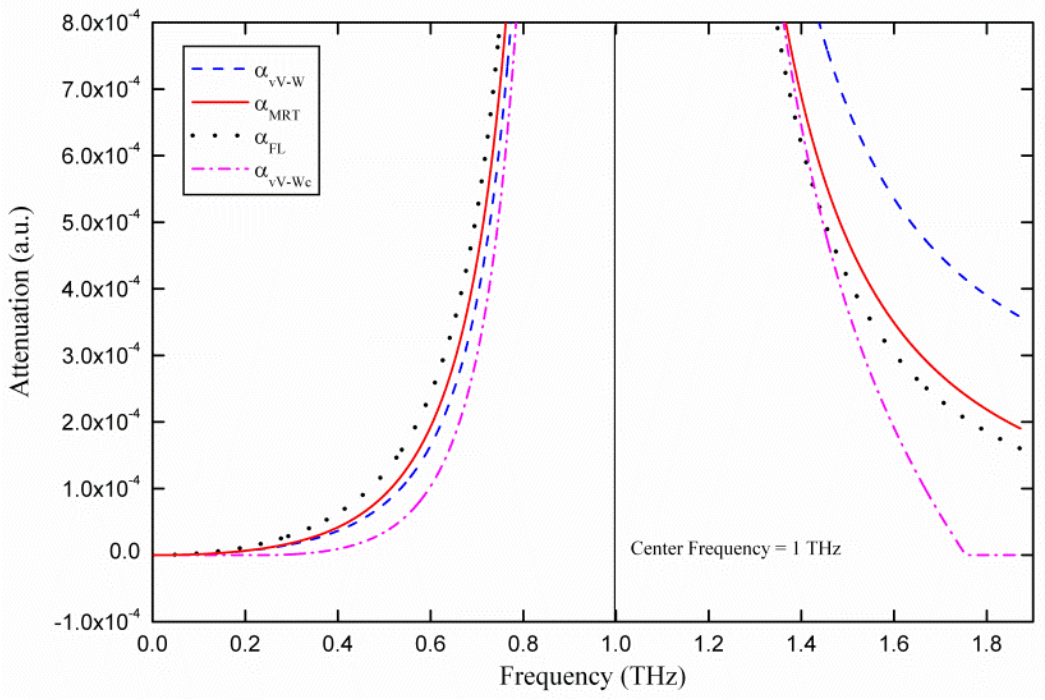

Fig. 5-2. Absorption line comparison of a single resonance line of vV-W, FL, MRT, and the vV-Wc with cut-off at 1.75 THz. (Figure adapted from Ref.[41])

where the density-related parameters $C_W^* = (1.33)^2 C_W$ and $C_A^* = (1.33 \times 0.84) C_A$, and the water vapor density ρ_W in g/m^3 can be obtained from the partial pressure P in hPa by multiplying by the factor of 1.33 for water vapor and 0.84 for air. And $C_W = C_W^0 \cdot \theta^{n_s+3}$ and $C_A = C_A^0 \cdot \theta^{n_f+3}$ as the fitting parameters for all of the curves which were obtained at 294 K, where C_W^0 and C_A^0 are the self and foreign continuum parameters at 300 K in units of dB/km/(hPa·GHz)2 respectively, θ is the temperature factor which equals to 300/T, ns and nf are their temperature exponents, and v is frequency in GHz.

5.2.4 Cross-Term (X-term)

In this work, instead of measuring the absolute total absorption α of a moist sample signal compared with a dry reference signal, we measured the relative total absorption $\Delta\alpha_x$ between the sample and reference signals with different humidity levels, where the designation of $\Delta\alpha_x$ indicates that there will be a cross term due to the quadratic part of continuum absorption [41],

$$\Delta\alpha_x = \alpha^S - \alpha^R = \left(\alpha_{MRT}^S + \alpha_c^S\right) - \left(\alpha_{MRT}^R + \alpha_c^R\right) = \Delta\alpha_{MRT} + \left(\alpha_c^S - \alpha_c^R\right) = \Delta\alpha_{MRT} + \Delta\alpha_{cx}. \qquad (5\text{-}7)$$

where the α^S, α_{MRT}^S, α_c^S and α^R, α_{MRT}^R, α_c^R denote the absolute total absorption, absolute MRT resonance absorption, and absolute continuum absorption of the sample and reference signals respectively; And the relative resonance lines absorption $\Delta\alpha_{MRT}$ is linearly proportional to water vapor number density. Based on Eq. (5-7), the relative continuum absorption including the cross term $\Delta\alpha_{cx}$ is given by,

$$\Delta\alpha_{cx} = \alpha_c^S - \alpha_c^R = \nu^2 \left[C_W^* \cdot \left(\left(\rho_W^S\right)^2 - \left(\rho_W^R\right)^2 \right) + C_A^* \cdot \rho_A \cdot \left(\rho_W^S - \rho_W^R\right) \right]. \qquad (5\text{-}8)$$

where ρ_W^S and ρ_W^R are water vapor density of the sample and reference signals respectively, and the density difference $\Delta\rho_W = \rho_W^S - \rho_W^R$. Substituting $\rho_W^S = \rho_W^R + \Delta\rho_W$ in Eq. (5-8), we obtain:

$$\Delta\alpha_{cx} = \nu^2 \left[C_W^* \cdot \left(2\rho_W^R \Delta\rho_W + \Delta\rho_W^2 \right) + C_A^* \cdot \rho_A \cdot \Delta\rho_W \right]. \tag{5-9}$$

and the cross term function X is given by

$$X = \nu^2 C_W^* \left(2\rho_W^R \Delta\rho_W \right). \tag{5-8}$$

In this paper, the cross term has to be subtracted from the relative continuum absorption $\Delta\alpha_{cx}$ and the relative total absorption $\Delta\alpha_x$. Eqs. (5-10a) and (5-10b) enable the comparison of the absolute continuum absorption $\Delta\alpha_c$ and the absolute total absorption $\Delta\alpha$, which only depend on $\Delta\rho_W$, with other works which have dry reference signals,

$$\Delta\alpha_c = \Delta\alpha_{cx} - X = \nu^2 \left[C_W^* \cdot \Delta\rho_W^2 + C_A^* \cdot \rho_A \cdot \Delta\rho_W \right]. \tag{5-10a}$$

$$\Delta\alpha = \Delta\alpha_x - X. \tag{5-10b}$$

The value of water vapor density of reference THz signal ρ_W^R in the additional cross term $\rho_W^R \Delta\rho_W$ can be obtained from the water vapor partial pressure measured by hygrometers in the sample chamber. The quadratic frequency dependence of the continuum absorption was confirmed in our experiments.

5.3 Experimental Results and Discussion

Two measurements have been completed with different levels of reference humidity using the 170 m Long-Path THz system with controlled RH chamber. The first group of

measurement has two sets of data that were taken on two different days, 20 days apart, shown in Fig. 5-3. The lowest dry reference signal had a RH of 22.2% at 21 ℃ (corresponding to a water vapor density of 4.1 g/m^3), which gave a cross-term with power attenuation of 23% of the total continuum absorption before subtracting the cross-term for 7.0 g/m^3 water vapor density (corresponding to a RH difference of 38.2%). The second group of measurements has two sets of data that were taken on two different days, 7 days apart, shown in Fig. 5-5. The dry references had RH of 13% and RH 8% at 21 ℃, respectively, corresponding to the reference water vapor densities ρ_W^R of 2.3 g/m^3, and = 1.4 g/m^3. Consequently, the corresponding cross terms X are much reduced from the earlier measurement [41].

The measured THz pulses in each group were recorded from the same start position of the time scan, which allowed obtaining the transit time difference between the THz pulses with various RH. The time values in ps at the beginning of the THz signals are the absolute transit time from the start point. $\Delta\rho_W$ denotes the difference of water vapor density between the sample signal and reference signal and is calculated by the transit time differences of THz pulses, based on the linear relationship to the frequency independent part of the refractivity [15, 19]. This method has the advantage of obtaining the RH along the entire path inside the chamber more precise than hygrometers.

5.3.1 High Relative Humidity Reference Signal

The measured THz signals are shown in Fig. 5-3a and 5-3c, and the corresponding frequency spectra shown in Fig. 5-3b and 5-3d are averages of three THz pulses in each set. The dry reference signals had RH of 22.2% at 21 ℃ (corresponding to a water vapor density of 4.1 g/m^3) and RH of 25.3% at 21 ℃ (corresponding to a water vapor density of 4.6 g/m^3).

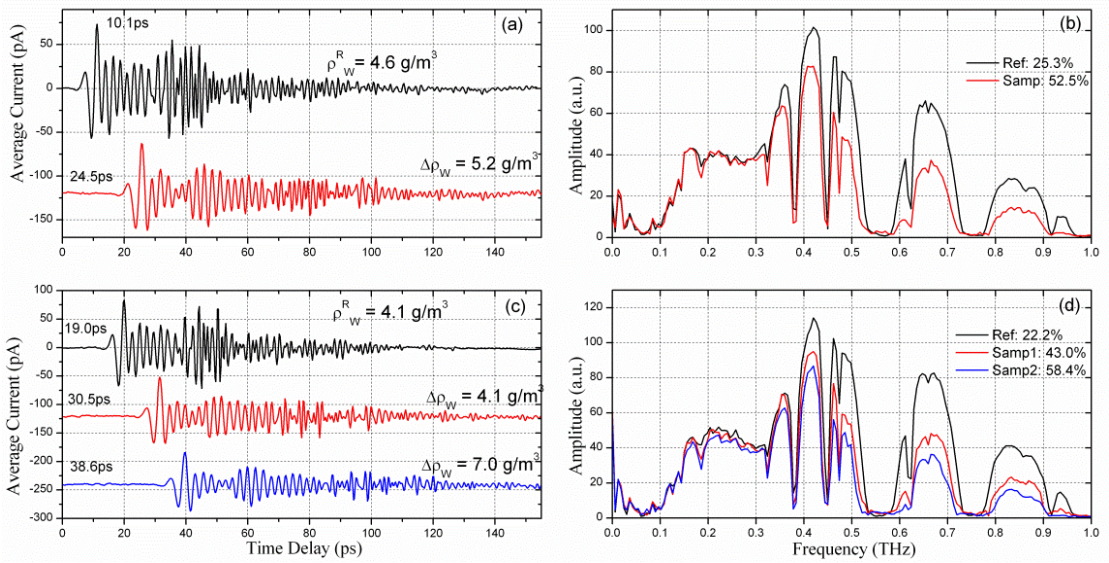

Fig. 5-3. (a) Reference pulse (top trace) and sample pulse (bottom trace). (b) Amplitude spectra corresponding to (a). (c) Reference pulse (top tract) and two sample pulses (lower traces). (d) Amplitude spectra corresponding to (c). (Figure adapted from Ref.[41])

The frequency independent part of water vapor refractivity is (n-1) = 61.6 x 10^{-6} in an atmosphere with RH 58% at 20 ℃ (density of 10 g/m^3) [19]. The transit time of THz pulses through the 137 m total round-trip path in the RH (density 10 g/m^3) controlled chamber is 27.9 ps longer, than for a dry chamber. By comparing the transmitted time difference Δt of the sample and reference pulses with 27.9 ps / (10 g/m^3), the relative water vapor density can be calculated to an accuracy of 0.04 g/m^3, corresponding to RH 2%, and a 0.1 ps delay change.

The relative amplitude transmission of set No. 2 with respect to the reference of Fig. 5-3d is shown in Fig. 5-4a for the path length of 137 m. The corresponding relative total absorption coefficients $\Delta\alpha_x$ in dB/km for different humidity levels were from the measurements of Fig. 5-3d and the results are shown in Fig. 5-4b with smoothed measured window curves, obtained by using the Matlab command in order to minimize the ripple effect and locate the average value positions of the measured points.

Four transmission windows at 0.41 THz (W1), 0.46 – 0.49 THz (W2), 0.68 THz (W3) and 0.85 THz (W4) are shown clearly within 0.35 – 1 THz. The grey regions cover no signal areas, caused by the strong water vapor absorption lines. Within all four windows, the curve with 4.1 g/m^3 has the lowest absorption and the upper curves have higher water vapor density.

The measured relative total absorption $\Delta\alpha_x$ and the calculated relative resonance absorption for the water vapor density difference of $\Delta\rho_W$ = 7.0 g/m^3 are shown in Fig. 5-5a. Using HITRAN database and MRT theory with same water vapor density as experiments, the relative resonance line absorption $\Delta\alpha_{MRT} = \alpha_{MRT}^S - \alpha_{MRT}^R$ were calculated and plotted as the black solid curves shown in Fig. 5-5. According to the accepted definition, the continuum absorption with cross-term X can be obtained by simply calculating the difference between $\Delta\alpha_x$ and $\Delta\alpha_{MRT}$ at all THz windows. Therefore, the difference between the measured absorption and calculated MRT absorption is the continuum absorption plus the cross-term X as described Eq. (5-5).

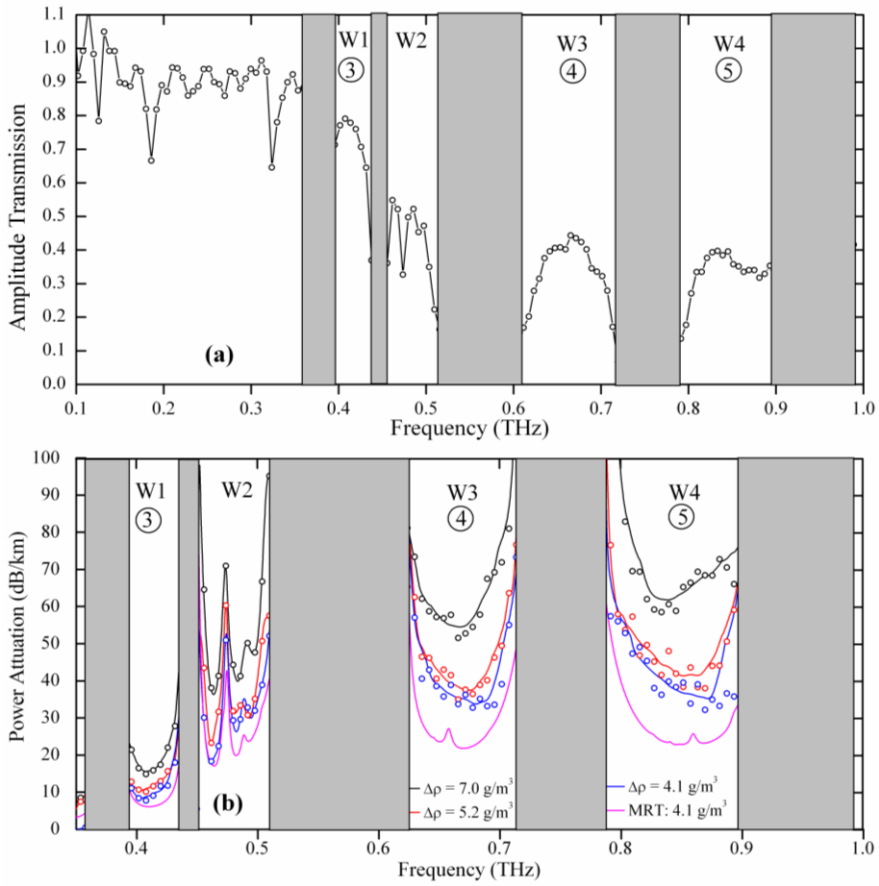

Fig. 5-4. (a) Amplitude transmission for $\Delta\rho_w$ = 7.0 g/m^3 in Fig.5-3d. (b) Measured power attenuation coefficients $\Delta\alpha_x$ in dB/km, for the water vapor density differences of $\Delta\rho_w$ = 4.1 g/m^3 (bottom blue circles), $\Delta\rho_w$ = 5.2 g/m^3 (middle red circles) and $\Delta\rho_w$ = 7.0 g/m^3 (top black circles), and MRT calculation for $\Delta\rho_w$ = 4.1 g/m^3 (bottom purple line). (Figure adapted from Ref.[41])

We determined the values of relative continuum absorption $\Delta\alpha_{cx}$ and X at each window, from the difference between the minima of the calculated resonance absorption windows to the minimum of the smoothed windows as shown in Fig. 5-5a. The comparison between the empirical theory and historical curve below 400 GHz are also shown with a 5X magnification.

In Fig. 5-5c, the dashed lines for the three curves show that part of the continuum absorption due to the linear dependence on $\Delta\rho_W$, the difference between the two curves shows that part of the absorption due to the $\Delta\rho_W^2$ quadratic components. It is noteworthy that the fraction shows this $\Delta\rho_W^2$ dependence, but it is somewhat surprising that the quadratic term $\Delta\rho_W^2$ is such a relatively small fraction of the total. For example, for 7.0 g/m^3 the quadratic term is 33% of the total, and for 5.2 g/m^3 the term (highlighted in yellow) is 25% and for 4.1 g/m^3 the term is 20%.

In Fig. 5-5c, it is informative to compare the ratio of the MRT resonant line absorption to the empirically fit continuum absorption, $R_\alpha = \alpha_{MRT} / \alpha_c$, for the THz windows of transparency: for W4 at 850 GHz, R_α = 2.5, For W3 at 680 GHz, R_α = 3.3, for W2 at 475 GHz, R_α = 6.0, for W1 at 410 GHz R_α = 2.7, for the window at 345 GHz, R_α = 1.7, for the window at 220 GHz, R_α = 0.74, and at 100 GHz, R_α = 0.33. For the windows below 300 GHz, the continuum absorption has become larger than the MRT absorption. This situation has driven much interest in mm wave applications, for which the continuum absorption is the major component.

Our empirical curve of Fig. 5-5c, and the associated MRT resonant line absorption are in acceptable agreement with the recent simulation of the two optimal THz communication links in the atmosphere at 95 GHz, and 250 GHz [21]. In that work for 10 g/m^3 at 20 ^{o}C, at 95 GHz, α_c = 0.25 dB/km, and $\alpha_{vV\text{-}W}$ =0.27 dB/km, total α = 0.52 dB/km; at 250 GHz, α_c = 2.8 dB/km, and $\alpha_{vV\text{-}W}$ = 1.5 dB/km, total α = 4.3 dB/km. These values are comparable to our values shown in Fig. 5-5c

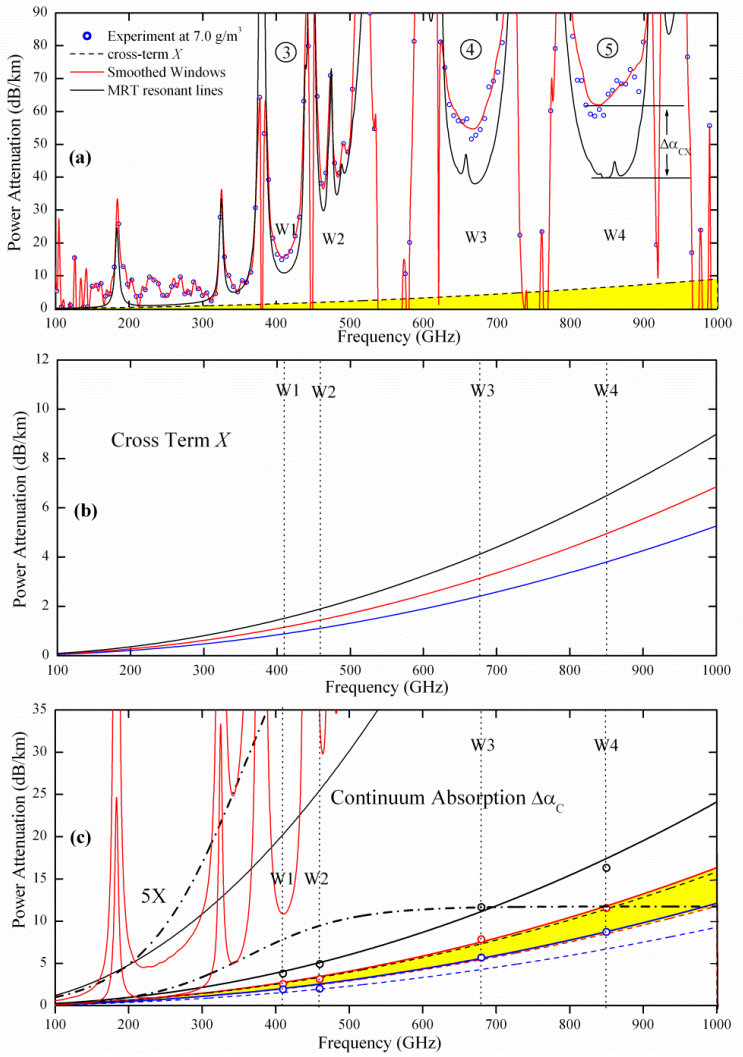

Fig. 5-5. (a) The measured total absorption (blue circles), smoothed measured THz window (red solid line), MRT lineshape (black line). The quadratic fitting for X (black dash line) with yellow highlight for $\Delta\rho_w$ = 7.0 g/m^3. (b) The calculated cross-term X absorption for 7.0 g/m^3 (top black line), 5.2 g/m^3 (middle red line), and 4.1 g/m^3 (bottom blue line). (c) The continuum absorption $\Delta\alpha_c$ and corresponding fitting (solid lines), and the historical curve in [11, 21] for 7 g/m^3 (dash dot line). The MRT calculation of Fig. 5-5(a) is shown as the lower red curve and is also shown as the 5X magnified red curve. (Figure adapted from Ref.[41])

(increased by 10/7 to account for the different water vapor density). Our increased values are for 100 GHz, α_c = 0.34 dB/km, and α_{MRT} = 0.21 dB/km, total α = 0.55 dB/km; For 250 GHz, α_c = 2.1 dB/km, and α_{MRT} = 1.43 dB/km, total α = 3.53 dB/km.

The differences $\Delta\alpha_{cx}$ between minima of the measurement and the $\Delta\rho_W$ = 7.0 g/m^3 MRT curve for each window shown in Fig. 5-5a are presented in Table 1, together with the corresponding cross-term X and the desired absolute continuum absorption $\Delta\alpha_c$. These same parameters are listed in the table for $\Delta\rho_W$ = 4.1 g/m^3 and $\Delta\rho_W$ = 5.2 g/m^3. Figs. 5-5b and 5-5c show the corresponding values taken from the table, showing excellent agreement with the squared frequency dependence of Eqs. (5-5) - (5-9). The theoretical curves presented in Figs. 5-5b and 5-5c are obtained from Eqs. (5-8) and (5-9a) with $C_W^* = (1.33)^2 C_W$ and $C_A^* = (1.33\times 0.84)C_A$, where C_W and C_A are given in Table 2.

Table 5-1 The determined values of $\Delta\alpha_{cx}$, X, $\Delta\alpha_c$ in dB/km at four THz windows with different density. (Adapted from Ref. [41])

Windows	$\Delta\rho_w$(4.1 g/m^3)			$\Delta\rho_w$(5.2 g/m^3)			$\Delta\rho_w$(7.0 g/m^3)		
All values (dB/km)	$\Delta\alpha_{cx}$	X	$\Delta\alpha_c$	$\Delta\alpha_{cx}$	X	$\Delta\alpha_c$	$\Delta\alpha_{cx}$	X	$\Delta\alpha_c$
W1	2.8	0.9	1.9	3.7	1.2	2.5	5.3	1.5	3.8
W2	3.1	1.1	2.0	4.2	1.4	2.8	6.8	1.9	4.9
W3	8.1	2.4	5.7	11.0	3.2	7.8	15.8	4.2	11.6
W4	12.5	3.8	8.7	16.5	4.9	11.6	22.5	6.5	16.0

Table 5-2 Laboratory determinations of water vapor self and foreign continuum parameters in millimeter wave and THz range. The C_W and C_A parameters are in units of dB/km/(GHz hPa)^2.

Reference	C_W ($x10^{-7}$)	C_A ($x10^{-9}$)	n_s	n_f	Experimental conditions	Database	v-VW Pre-factor	Cutoff (GHz)
This Work	0.95	1.69	NA	NA	0.35-1 THz 294 K	HITRAN	$(v/v_j)^2$	None
Slocum [27]	0.45	4.12	NA	NA	0.3-1.5 THz 296 K	HITRAN	v/v_j	None
Podobedov [8]	0.48*	2.55*	5.50	1.80	0.3-2.7 THz 293-333 K	HITRAN	v/v_j	750
Koshelev [39]	0.94*	3.11*	5.24	0.91	107-143 GHz 261-328 K	R98 [14]	$(v/v_j)2$	750

*The values are calculated from original C_W^0 for 294 K. (Adapted from Ref.[41])

The self and foreign broadened parameters, which have been obtained from different studies [8, 27, 39] and this work are shown in Table 2. Our pressure-related continuum parameters C_W and C_A do not agree with those of [8, 27], as expected, since they used the vV-Wc model and the linear prefactor for the vV-W lineshape function. Moreover, our ratio of C_W/C_A = 56.2, for the contribution of dimers to that of the water-air collisions comprising the total continuum absorption, as described in Eq. 5-10a, is much higher than that for the other two THz measurements of 18.6 in [8] and 10.9 in [27]; and is significantly higher than that for the millimeter measurement of 30.2 in [39].

5.3.2 Low Relative Humidity Reference Signal

The measured THz pulses and their corresponding Fourier-transformed frequency spectra are shown in Figs. 5-6a – 5-6d, for two groups of measurements taken on two different days, 7 days apart. The dry reference signals had RH of 13% at 21℃ (corresponding to a water vapor density of 2.3 g/m^3) and RH of 8% at 21℃ (corresponding to a water vapor density of 1.4 g/m^3). The measured relative power absorption $\Delta\alpha_x$ shown as black solid line and circles in Fig. 5-6e and 5-6f are the power attenuation with unit of dB/km.

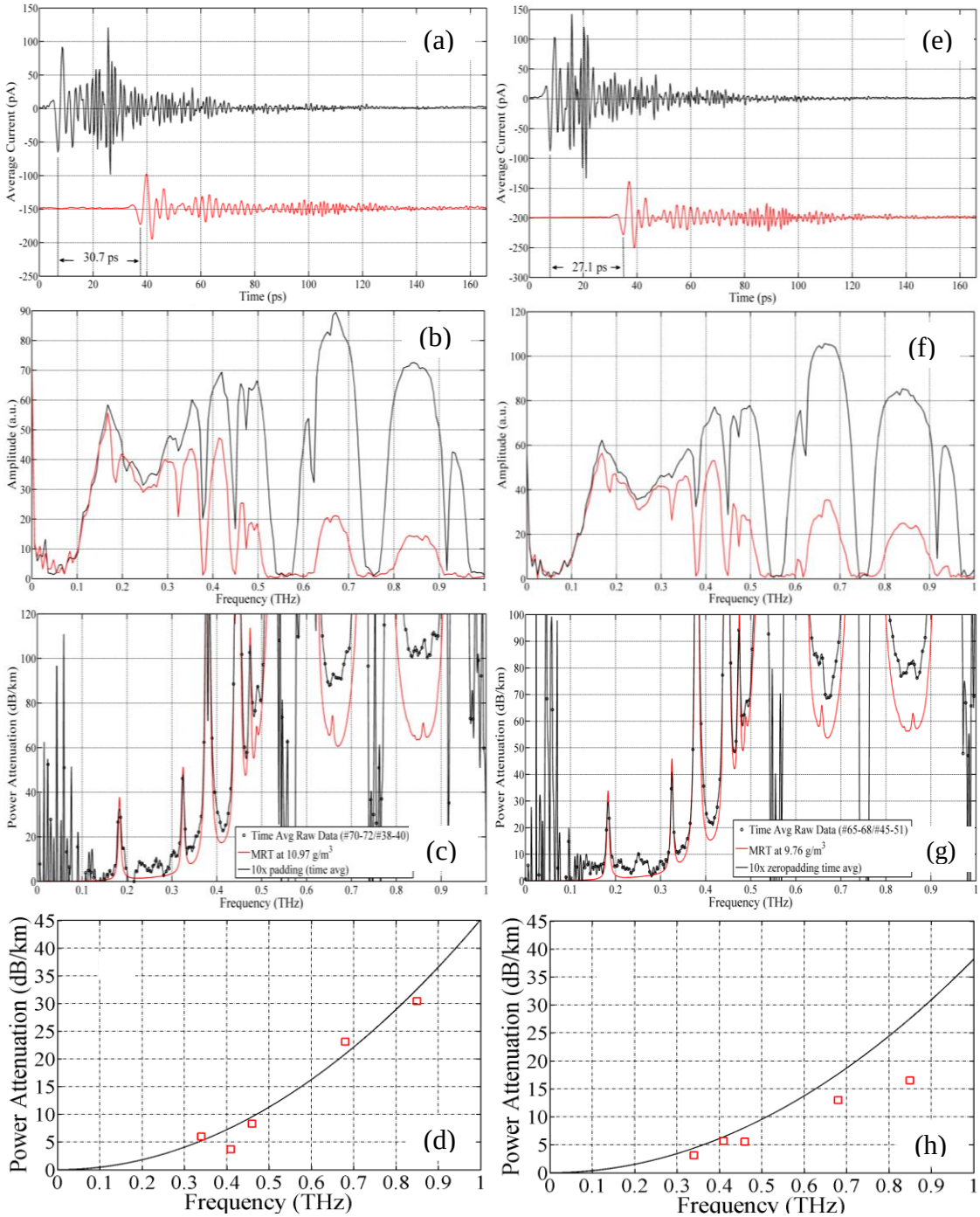

Fig. 5-6. Two sets of measurements are shown as: Measured THz pulses transmitted through the 137 m sample chamber in (a) and (e); Corresponding amplitude spectra in (b) and (f); Corresponding power attenuation in (c) and (g); Corresponding continuum absorption in (d) and (h). (Figure adapted from Ref.[44])

In Figs. 5-6d and 5-6h the determined water vapor continuum absorption at five THz windows (red open squares) compared to the empirical equation for measurements $\Delta\rho$ = 11.0 g/m^3 and $\Delta\rho$ = 9.8 g/m^3. the values of the continuum absorption are compared with the empirical theory of Eq. (5-3), using the same values of the parameters C_W* and C_A* in Table 2.

5.3.3 Backward Propagation

As we introduced in the Chapter 4, the linear relationship between RH and pulses time delay Δt can avoid using the uncertain RH values from hygrometers and provide the most accurate water vapor density based on the measurement of pulse arrival time in precision of 0.1 ps. However, so far, in the calculation of continuum absorption, we still have to use this uncertain RH value from hygrometers in the cross-term X. In the latest experiments, the continuum absorption results have been obtained from the measurements with 2% RH reference hygrometer measurement, which could minimize the cross-term X.

In order to remove the impact from the cross-term X from the continuum absorption calculation, it was possible to back propagate the sample pulse using our linear dispersion theory simulation program, to check for consistency and to determine the phase modulated outgoing spectrum propagated through 170 m with RH of 0%.

As shown in Figs. 5-7a and 5-7b, the middle black curve is the reference signal which was firstly labeled as 2% RH from hygrometers in our experiment. If we treated this 2% RH reference signal as a sample signal, the 0% RH reference signal can be calculated using linear dispersion theory for a backward propagation. Based on the understanding of the water vapor absorption, the weak water vapor absorption lines are indicators of existing water vapor density in the sample chamber and lab, when the reference signal propagated through the Long-Path system. We assume that for 0% RH reference signal, both sample chamber and lab had the same RH level.

So in the backward propagation calculation, 170 m was used as the total propagation distance for reference signal. After the calculation of backward propagation, a more precise RH value of 8% for the previous 2% RH reference signal is obtained.

The experimental measurements of the transmitted reference pulse with RH 8% are shown in Fig. 5-7a, and the corresponding amplitude spectra are shown in Fig. 5-7b. In Fig. 5-7a, the upper blue is the asymmetric RH 0% outgoing pulse, and the measured THz pulse transmitted through the 170 m path at RH 8% at 21 ^{o}C is shown as black middle pulse, and the THz pulse transmitted through the 137 m path sample chamber at RH 65% at 21 ^{o}C is the red lower pulse. The difference in transit times between the RH 8% and the RH 65% pulses is 27.1 ps corresponding to a change in water vapor density of $\Delta\rho = 9.8$ g/m^3. The blue upper line shows the amplitude spectrum of the RH 0% outgoing pulse and the insert shows the phase modulation of the RH 0% complex outgoing spectrum in Fig. 5-7b. The back-propagation was stopped when the absorption lines with RH 8% disappeared. The corresponding phase modulated outgoing amplitude spectrum is shown as the upper line in Fig. 5-7b, and the corresponding asymmetric outgoing pulse (calculated by IFFT) as the blue upper pulse in Fig. 5-7a.

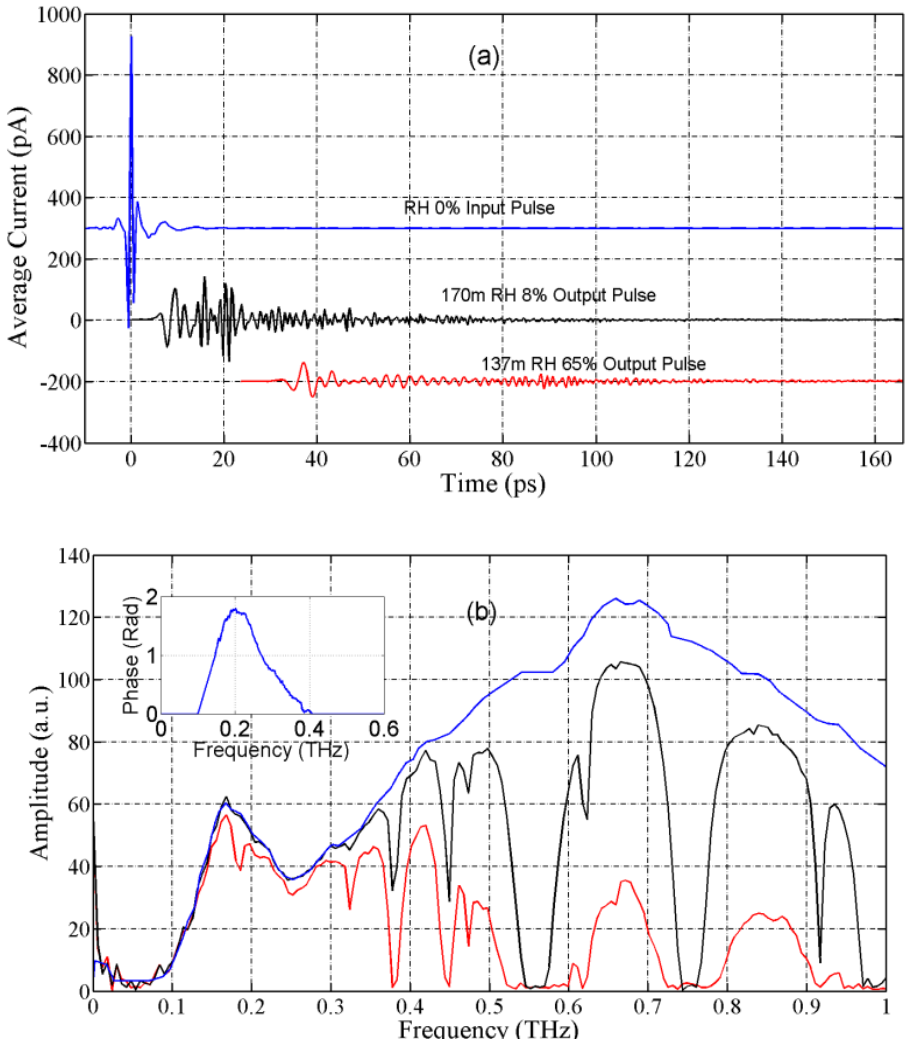

Figure 5-7. (a) RH 0% outgoing pulse, Measured THz pulse transmitted through the 170 m path at RH 8% at 21 °C (black middle pulse) and the THz pulse transmitted through the 137 m path sample chamber at RH 65% at 21 °C (red lower pulse). (b) Corresponding amplitude spectra. (Figure adapted from Ref. [45])

Given this complex outgoing spectrum, it is possible to check the accuracy of the numerical simulations, by calculating (in the frequency domain) the propagation of the RH 0% pulse through the 170 m path with RH 8%.

For our simulation calculations the propagated THz pulses are obtained from the linear dispersion theory calculation in the frequency domain [18], using the absorption and phase, as shown below.

$$E(z,\omega) = E(0,\omega) \cdot e^{i\Delta k(\omega)z} \cdot e^{-\alpha(\omega)z/2}. \tag{5-11}$$

for which the outgoing complex amplitude spectrum is given by E(0,ω), and the incoming complex spectrum is given by E(z,ω). The phase is Φ = Δk(ω)z. The amplitude transmission is exp[-α(ω)z/2]. The wave vector Δk(ω) is based on the complete van-Vleck Weisskopf lineshapes [18, 41], and the absorption coefficient α(ω), is based on the MRT combination of the complete van-Vleck Weisskopf and Lorentzian lineshapes summed over either the JPL or the HITRAN data bases. The resulting time-domain pulses are the IFFT of E(z,ω) of Eq. (5-11). For the back-propagation and the simulation shown in Fig. 5-7, the continuum absorption of Eq. (5-6) was included.

Then given the incoming complex spectrum, IFFT gives the corresponding incoming calculated (upper red) pulse, which is compared to the measured (lower black) pulse, under these same conditions in Fig. 5-8a. The corresponding amplitude spectra are compared in Fig. 5-8b with measured pulse in black and calculation in red. The agreement is excellent and thereby documents the accuracy of the simulation.

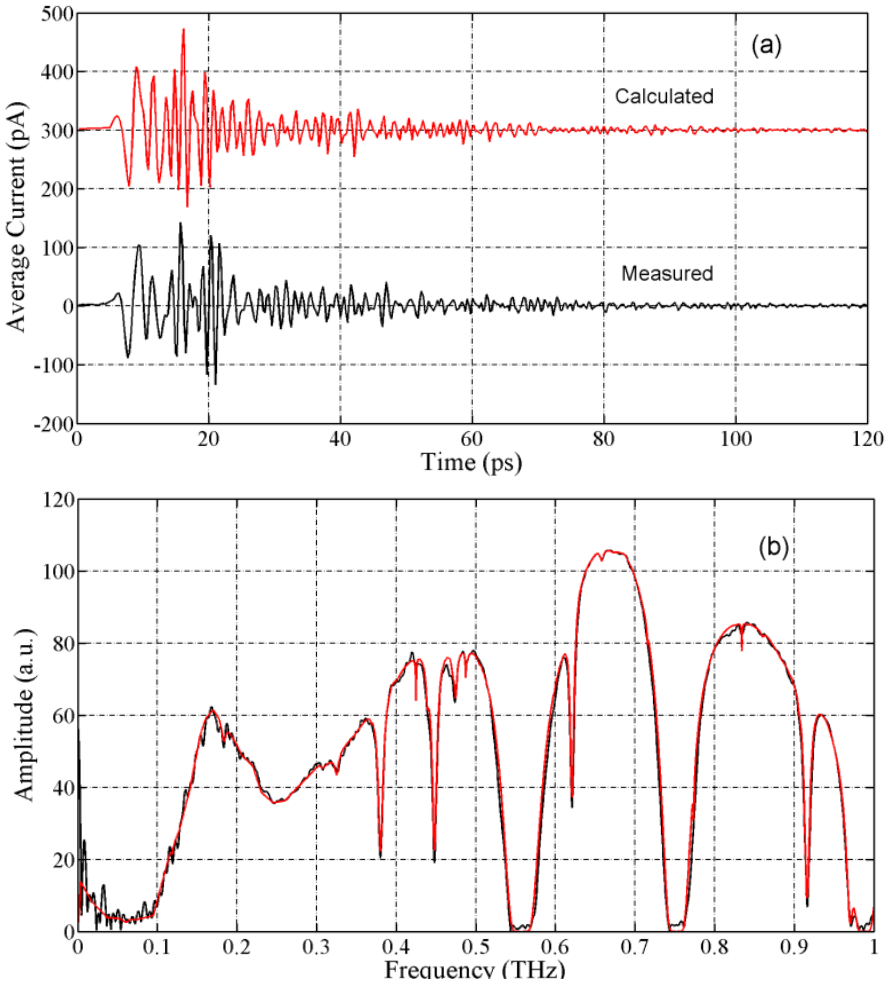

Fig. 5-8. (a) Calculated (red upper) pulse compared with measured (black lower) pulse transmitted through the same RH 8%, 170 m long path. (b) Comparison of the measured with the calculated spectrum. (Figures adapted from Ref.[45])

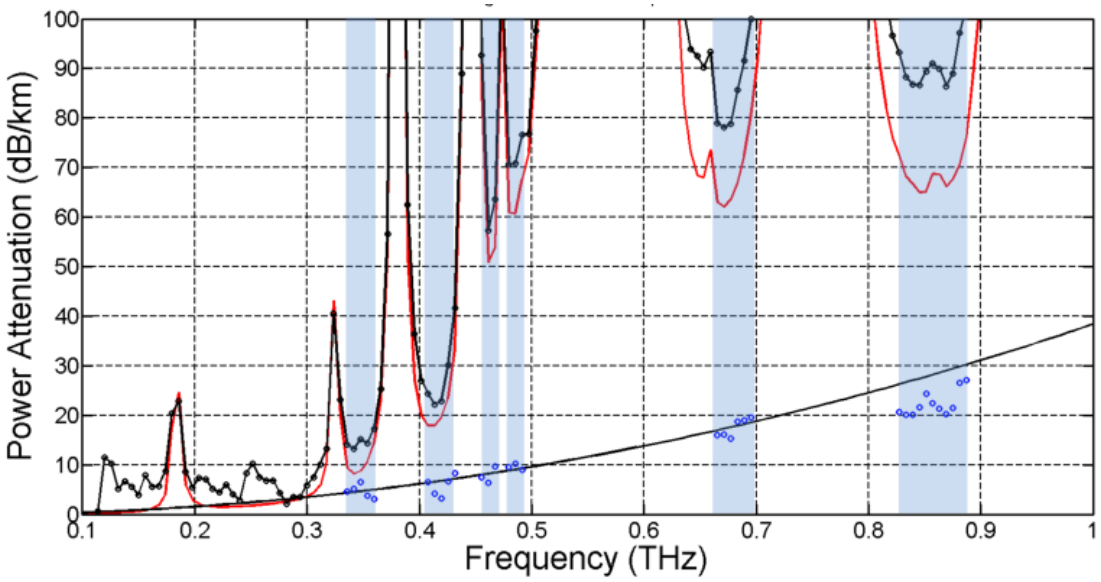

Fig. 5-9. Measured water vapor absorption $\Delta\alpha_x$ (black curve and circles), calculated MRT resonant lines absorption $\Delta\alpha_{MRT}$ (red curve). Continuum absorption given by the blue circles, compared to Eq. (5-5) (black curve). (Figure adapted from Ref. [45])

Consequently, we and demonstrated the outgoing pulse to our RH controlled sample chamber. Using this outgoing pulse shown in Fig. 5-8a and the corresponding amplitude and phase-modulated spectrum shown in Fig. 5-8b, as the reference THz-TDS outgoing pulse, we directly obtain the experimental absorption coefficient for the 137 m path at RH 65% in the sample chamber from the measured transmitted pulse shown in Fig. 5-8a. The result with the X term does not apply, because we have determined the outgoing RH 0 % reference pulse in Fig.5-9.

In Fig. 5-9 the measured total absorption $\Delta\alpha$ and the calculated MRT resonant absorption $\Delta\alpha_{MRT}$ for the water vapor density difference of 11.2 g/m^3 are shown [41, 43]. The values of the water vapor continuum absorption were determined as $\Delta\alpha_c = \Delta\alpha - \Delta\alpha_{MRT}$, shown as the red circles for the THz transmission windows, 0.35, 0.41, 0.46, 0.68,and 0.85 THz, and are compared to Eq. (5-10), with Cw* and CA* from Ref. 1, shown as the bottom black curve.

THz digital data can be transmitted through windows with the data rate and propagation distance consistent with the absorption and group velocity (GVD). Since GVD is negligible for the continuum, the water vapor continuum only limits the propagation distance. For THz windows below 300 GHz, the continuum absorption is larger than the MRT absorption [21, 41].

5.3.4 The Comprehensive Water Vapor Absorption Model

With understanding of the water vapor resonant absorption and phase in Chapter 3, water vapor frequency-independent dispersion in Chapter 4, and the water vapor continuum absorption in this chapter, the comprehensive model for water vapor total absorption, phase shift and dispersion can be obtained with consideration of all above three parts.

For the atmosphere at 58% and 21 ^{o}C (water density of 10 g/m^3), the water vapor absorption including MRT resonant absorption and continuum absorption are shown in Fig. 5-10a; The vV-W-HITRAN + Oxygen phase in units of Radians/km is shown in Fig. 5-10b. And the corresponding group velocity dispersion (GVD) is in units of (ps^2/km).

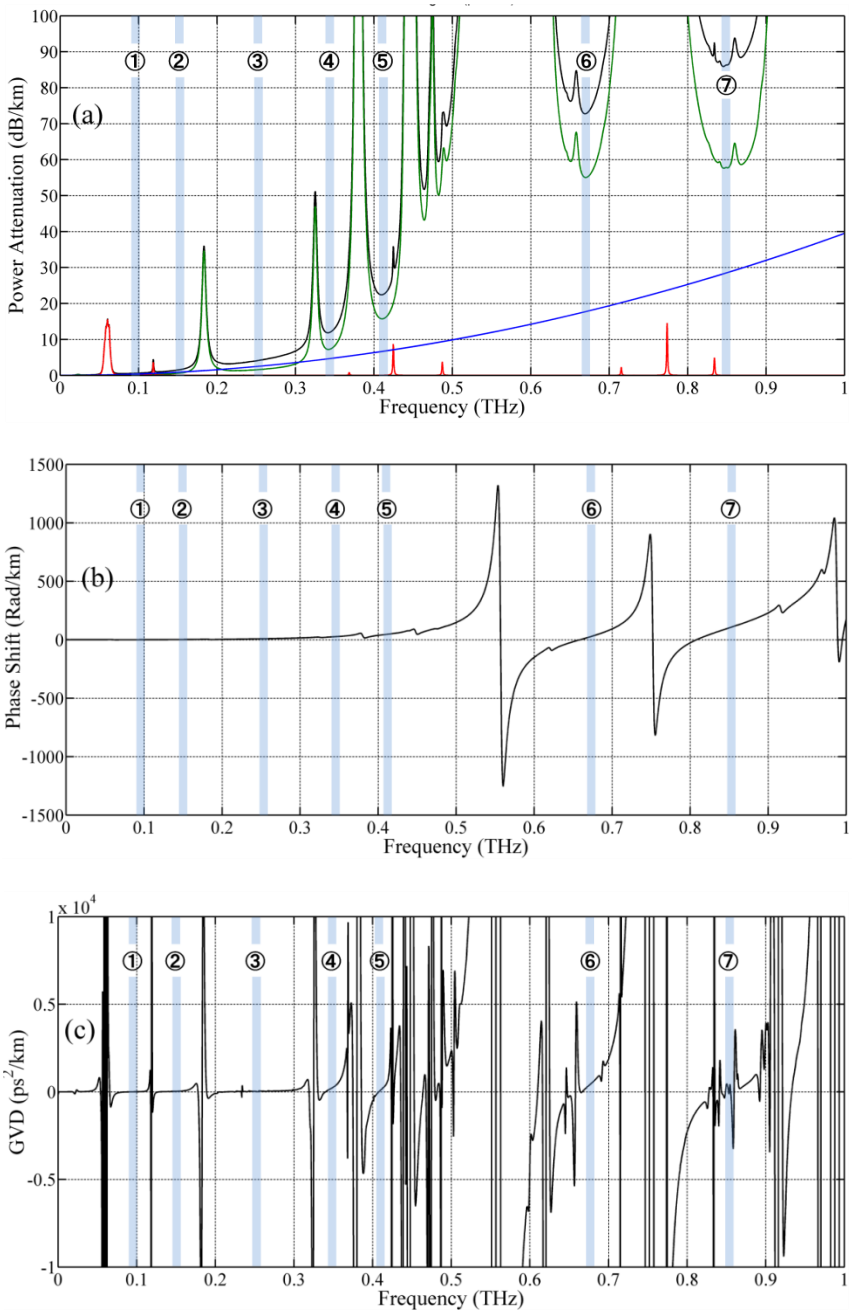

Figure 5-10. Summary results for the atmosphere at RH 58% and 20 ℃ (density of 10 g/m^3). (Figure adapted from Ref. [44])

In Fig. 5-10 of summary results for the atmosphere at RH 58% and 20 ℃ (density of 10 g/m^3),the numbered shaded lines mark the digital communication channels at 96 GHz, 144 GHz, 252 GHz, 342 GHz, 408 GHz, 672 GHz, and 852 GHz. The MRT + the continuum absorption + Oxygen absorption is shown as the upper black curve in units of dB/km. The MRT absorption is shown as the lower green curve. The continuum absorption is shown as the lowest blue curve. The oxygen absorption lines are shown as the lowest (red) resonance lines.

It is noteworthy that oxygen absorption lines are not considered in MRT simulation since the only variable in experiments is the amount of water vapor. But for the demonstration of atmospheric THz wireless communication channels shown in Fig. 5-10, all of the water vapor resonant absorption, continuum absorption and oxygen resonant absorption are considered.

Based on this comprehensive model, seven digital communication channels are proposed. As marked as blue regions in Fig. 5-10, the center frequencies of the seven digital communication channels are located in the windows of transparency. In addition, for broad-band digital communications, the center frequencies are also located at the minimum values of GVD within the windows to minimize pulse broadening. These seven center frequencies are also indicated on the GVD curve of Fig. 5-10c, and will be discussed in more detail below.

For the absorption shown in Fig. 5-10a, it is informative to compare the ratio of the MRT resonant line absorption to the empirically fit continuum absorption, $R_\alpha = \alpha_{MRT} / \alpha_c$, for the THz windows of transparency: at 852 GHz, $R_\alpha = 2.03$, at 672 GHz, $R_a = 3.10$, at 408 GHz, $R_\alpha = 2.37$, at 342 GHz, $R_\alpha = 1.57$, at 252 GHz, $R_\alpha = 0.62$, at 145 GHz, $R_\alpha = 0.59$, and at 95 GHz, $R_\alpha = 0.42$. For the windows below 300 GHz, as the frequency is reduced the continuum absorption becomes larger than the MRT absorption. This situation has driven much interest in mm wave applications, for which the continuum absorption is the major component.

Although THz waves have higher attenuation than microwaves from a humid atmosphere, rain, fog, dust and scintillations, THz waves are much better than the Free Space

Optical (FSO) communication systems, which use infrared and optics, under the same weather conditions. Moreover, the FSO has limitations on the data rates and transmission distance, from eye-safety limited transmission power, and the misalignment between transmitter and receiver. The THz wireless communication system is an alternative option to replace FSO with a more robust operation in bad weather.

It is important to note that the channel frequencies of 96 GHz, 144 GHz, and 252 GHz of this work are contained within the mm-wave domain, also designated as the extremely high frequency domain (EHF) extending from 30 to 300 GHz [5]. Our proposed Channel I, THz ground link with the center frequency of 96 GHz and 30 GHz FWHM bandwidth essentially fills the EHF-W Band with boundaries from 81-111 GHz [5]. Our Channel 3, THz geosynchronous satellite link with center frequency 252 GHz and 50 GHz FWHM bandwidth is also within the EHF domain. At the present time no operative W-Band communication systems have been developed [4], and there is no commercial activity from W-Band up to 300 GHz, the high frequency limit of the EHF range. The W-Band is currently considered as the frontier for space telecommunications.

An important demonstration of a custom built NTT prototype wireless system [4], was the 800 m wireless transmission trial of live television broadcast coverage of the Beijing 2008 Olympics. The transmitted power of 10 mW of 120 GHz Band 10 GbB (10.3125 Gb/s), had simple amplitude shift keying, and the receiver sensitivity was -35 dBm for a bit error rate of less than 10-12 [4].

The understanding of total water vapor impact on propagated THz signal shown in Fig. 5-10, provides theoretical background for next step of simulations for the achievable bit-rates and discussion of beam coupling provide a framework to present technical specifications for some of the high data rate applications for different ranges.

For the important application of Kiosk downloading [46], the THz transmitter is attached

to the fixed download station, and makes a wireless connection of a few cm to accomplish an ultrahigh download of multimedia material to the mobile THz receiver of the customer. For applications with a range of 10 m, THz wireless links are a promising solution for a wireless home entertainment system. Within this distance and stable indoor RH, the water vapor absorption can be neglected. In addition, other distributed storage devices could set up links with this hub to transmit a HD signal stream to the TV, providing a geometry of multi-point to point switchable links.

For applications with a range of 50 m, THz wireless links (852 GHz) can provide a 70 Gb/s direct point-to point connection between computer clusters. For a range of 100 m, the THz wireless links (852 GHz) are ideal to provide hotspots in a stadium, where large amounts of data are required by the crowds. With respect to the important need for the intermediate small cell and nanocell back-haul, that would be in place at near street level and would use the street signal light poles, large sign poles, and sturdy street light poles, for secure mounting,

Another significant application to consider would be a THz link (252 GHz) to a geo-synchronous communications satellite approximately 35,800 km above sea level has several important features compared to existing satellite links.

CHAPTER VI

BROADBAND THZ SIGNAL PROPAGATION THROUGH FOG

In this chapter, we experimentally demonstrate propagation with minimal distortion and attenuation of broadband, complex THz signals through 137 m of dense fog with an approximate visibility of 7 m. By controlling the concentration levels of fog inside the sample chamber, the direct measurements of fog effects, involve measuring the reshaped THz pulses and their relative transit times to a precision of ± 0.1 ps, utilizing a mode-locked laser as a precise optical clock. We have also determined the corresponding amplitude spectra of the propagated THz pulses. The experimental results indicate that the broadband THz pulses show almost no effects from passage through a dense artificial fog, which would be impenetrable for optical and IR beams. The Mie scattering model is used to calculate the optical visibility, while the Rayleigh scattering model is used to explain the observed THz attenuation. A discrepancy between the two models can only be resolved by assuming unusually small fog droplets.

6.1 Introduction

Advanced techniques, using propagating electromagnetic waves in the atmosphere, have attracted much attention due to their advantages of portability, easy-setup, low-cost and broad-band for many applications, such as infrared imaging, remote detection and Free Space Optics (FSO) wireless communications, covering frequencies from microwave to infrared and optics. However, suspended particles in the atmosphere, as in fog, smoke, clouds, dust and smog, can

cause severe scattering, resulting in large variations in the received power and markedly limiting the service availability of FSO and infrared applications. Recent studies have indicated that the optical power losses for dense maritime fog and moderate continental fog extend up to 480 dB/km and 120 dB/km respectively [47, 48].

In contrast to this situation, broadband THz pulses can propagate through dense fog with much smaller propagation loss. For example, the attenuation due to optical Mie scattering (wavelengths smaller than the fog droplet diameters) by fog with a water content density of 0.1 g/m^3 is 100 dB/km [49]. In contrast, the 500 GHz attenuation, by Rayleigh scattering (wavelengths much larger than the droplet diameters) is only 2.6 dB/km for the same density fog [50]. Here, we present experimental measurements that show that compared to the optical case, the reduction of THz loss in a fog, may even be better than the above comparison. We will now discuss the scattering sizes in clouds, fogs, smoke and dust, in order to illustrate the opportunities for THz links.

6.1.1 Particle Size Distribution

With similar microphysical structure, both clouds and fog can be characterized by their water content (g/m^3), optical visibility and droplet size distribution. Maritime fog is an advection fog that forms when warm, moist air moves over colder water; the average droplet diameter is of order 20 microns [51]. Continental fog is a radiation fog, that forms inland at night, usually in valleys and low marshes and along rivers; it is generally characterized by droplets smaller than 20 microns in diameter[51]. Moreover, cumulus and stratus clouds have a droplet size distribution under the upper boundary of 50 microns [52, 53], and with the mean diameters less than 20 microns. The droplet number densities are in the range of 100-500 per cubic centimeter. The liquid water content is less than 1.0 g/m^3 for cumulus clouds) [52]. Droplets with diameters larger than 50 microns become drizzle and increase in size during falling as rain [53].

In addition, several human activities, responsible for artificial cloud condensation nuclei (CCN), have been studied, such as, particles emitted from large paper mills [54], forest fires [54] and city pollution [55]. These effects can either broaden or narrow the cloud droplet size distributions in clouds from mean cloud droplet diameters of 20 microns up to 50 or down to 10 microns.

Several other types of particles may be suspended in the atmosphere to cause pollutions. For example, smog has particle sizes ranging from 0.003-6.8 microns [56]. The particle distributions from wood-smoke sources have a single mode that peaks between 0.1-0.2 microns particle diameter. A parameterization for the global mineral aerosol size distribution into a transport model using size classes between 0.1 and 50 microns has been reported [57]. The size classes are sand (particle diameters larger than 50 microns), silt (particle diameters between 2 and 50 microns), and clay (particles smaller than 2 microns). Since, the atmospheric lifetime of soil particles with diameters larger than 20 microns is less than a day, only smaller particles need to be considered for calculations of the effects of dust.

Some works discussing fog and smoke effects on free space optical links [58] and far-infrared holograms [59] have been reported recently. However, there is still a lack of studies on the characteristics of broad-band THz pulse propagation through dense fog and smoke. In addition, the random variations in the refractive index from the atmospheric turbulence caused by temperature inhomogeneity and pressure fluctuations can cause scintillations for FSO and IR applications. Refractive index fluctuations can distort the coherent phase front of an IR light beam during passage through a few kilometers of atmosphere. THz beams are much less susceptible to scintillation effects, compared to IR beams.

Based on the observations of fog and cloud droplet size distributions, we can now understand why broadband THz signals can propagate through dense of atmospheres of fog and clouds. This is due to the low attenuation of Rayleigh scattering for which the diameters of the

droplets of fog and clouds are much less than the THz wavelengths (300 microns for 1 THz).

This property gives THz frequency the opportunity for applications such as imaging through dense fog, clouds and smoke, and high data rate wireless communication without interruptions.

Although atmospheric water vapor absorption attenuates propagating THz signals, a series of comprehensive, theoretical and experimental studies [44], has shown for a 10 dB absorption loss, corresponding THz signal propagation distance within seven THz transparent windows, range from several hundred meters to several kilometers RH 58% (10 g/m^3) and 20 ℃.

6.2 Experiments

The long-path THz propagation experimental setup is described in [17, 19]. The combination of a standard THz-TDS system with the long-path propagation setup, includes the controlled sample chamber. The total THz propagation path, including the 137 m path within the chamber, is approximately 170.5 m, equal to 51 laser pulses round trips of 3.3423 m in the mode-locked femtosecond laser with a repetition rate of 89.6948 MHz [19]. A 12.5 μm thick sheet of plastic cling wrap covers the lab door, preventing fog from entering the lab. The THz pulses traverse the 12.5 μm sheet with no observable absorption or reflection.

The theater fog used in the sample chamber is generated by a Hurricane 901 fog machine designed to make fog for theatrical productions as shown in Fig. 6-1a. The water-based Chauvet Fog Fluid (FJU), with a specific gravity of 1.05, is a proprietary blend of 40% poly-functional alcohols with 60% water, being the main component. The FJU was diluted with water 4 times the initial volume, in order to increase the water percentage to 92% in the resulting fog. Thereby, the dielectric constant of droplets was reduced to 77 compared 80.3 for water. This reduction reduces attenuation of Mie and Rayleigh scattering by ratio (77/80.3 = 0.96), compared to water fog.

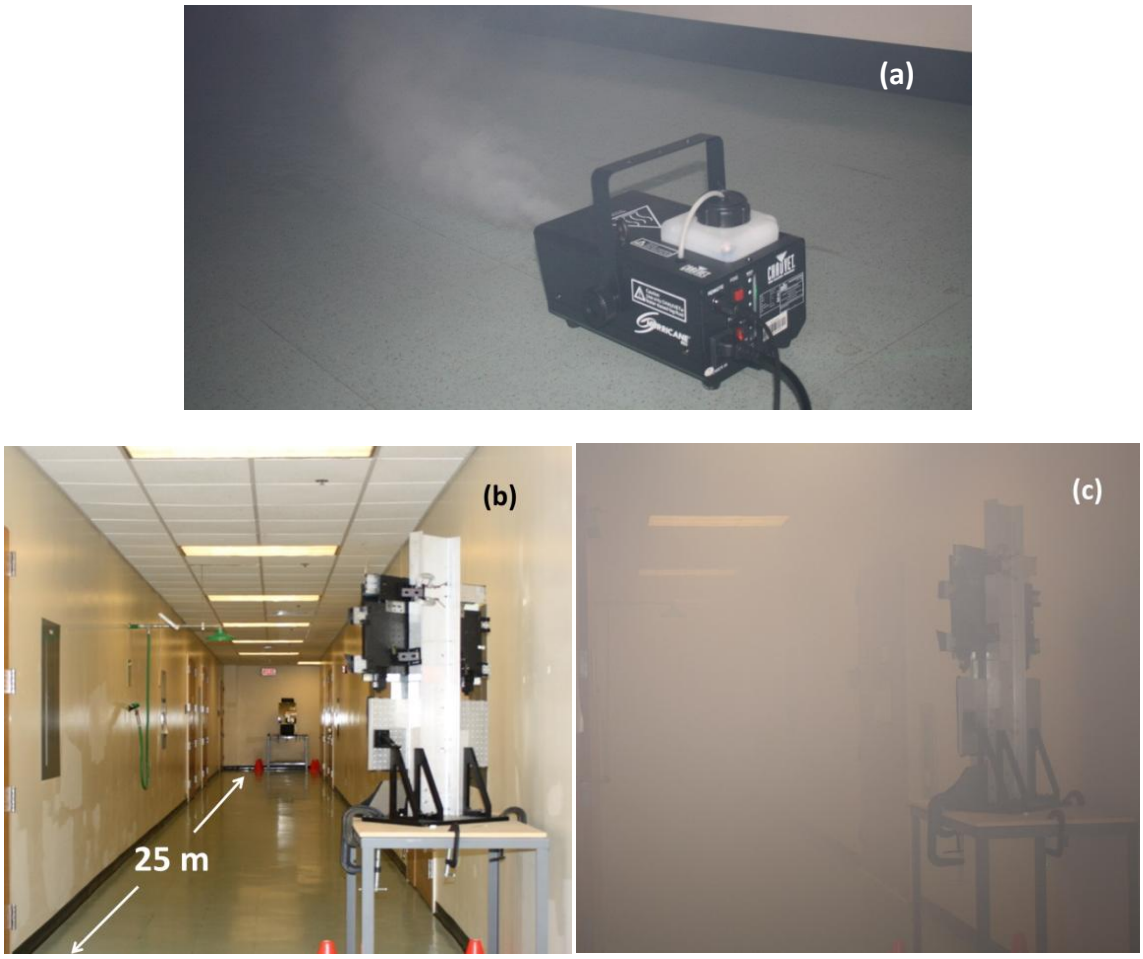

Fig. 6-1. (a) Photograph of artificial fog generator. (b) Photograph of clear–air chamber. (c) Photograph of fog filled chamber. (Figure adapted from Ref. [23])

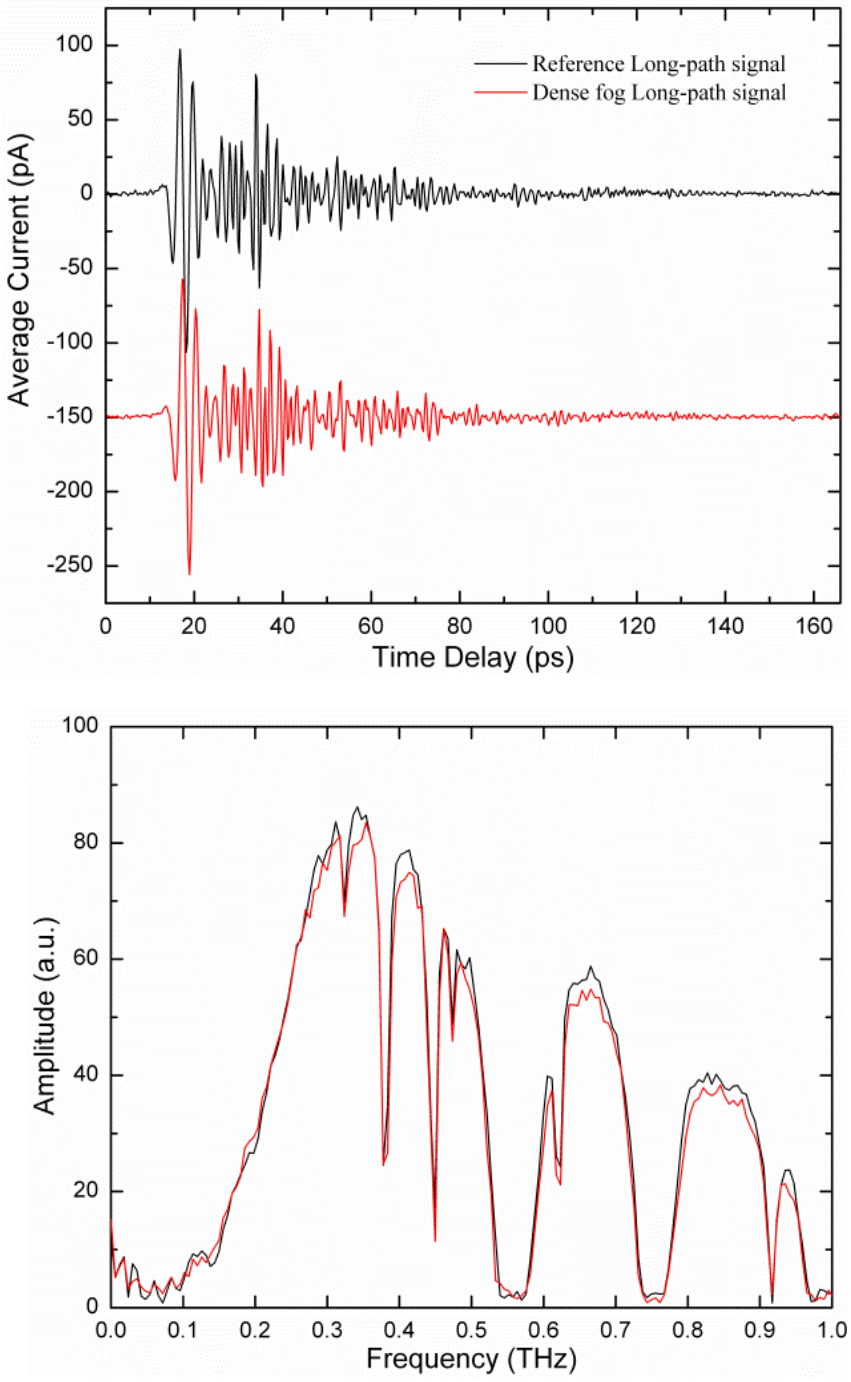

Fig. 6-2. (a). Measured THz pulses transmitted through sample chamber without fog (upper black trace) and with fog (lower red trace) (b) Corresponding amplitude spectra without fog (upper black) and with fog (lower red). (Figure adapted from Ref. [23])

The attenuation for optical Mie scattering by fog increases only as the square root of the water density [49]. In contrast, for the Rayleigh scattering of mm and THz waves by fog, the attenuation increases proportional to the water density [50]. Also, for constant water density and for droplets smaller than the wavelength, the Rayleigh attenuation is independent of the droplet diameter. In contrast, for a constant water density, the Mie scattering attenuation is inversely proportional to the droplet diameter. If the droplet diameter would be reduced from 10 microns to 2 microns, the Mie attenuation would increase from 1 dB/km to 5 dB/km, compared to water fog.

Figures 6-1b and 6-1c show the 25 m view from M5(M9) to M6 at one end of the clear-air chamber, before introducing the fog and the same view after 30 minutes of fog accumulation. It can be seen that, the dense fog reduces the visibility to approximately 7 m (the distance from M5(M9) to the first ceiling light), shown in Fig. 6-1c.

The measurement process is the following: Firstly, with the kinematic coupling assembly of M1 and M10 placed at the symmetric mid-point between the two parabolic mirrors of the THz-TDS system, several THz pulses transmitted through the sample chamber without fog are measured as reference pulses. The fog machine is then turned on for 30 minutes to accumulate heavy fog in the chamber, then the long-path THz dense fog pulses were measured. It is worth noting that a set of outgoing THz pulses in the standard THz-TDS system configuration (without M1 and M10) were taken at the beginning and end of the fog experiments, in order to monitor the stability of THz outgoing pulses.

6.2.1 Double Debye Model

The Rayleigh absorption approximation can be used for fog condition within THz range, instead of Mie scattering theory for fog effects on THz signal propagation. The microstructure of the particle can be ignored [50].

To calculate the power attenuation, we will only focus on the model introduced by Liebe et al [50],

$$\alpha = 0.1820 f N''(f) \tag{6-1}$$

where N'' is the imaginary part of the complex refractivity, and f is frequency in GHz. The incoming of Eq. (6-1) is in unit of dB/km.

$$N''(f) = \rho(9/2)\left[\varepsilon''\left(y^2+1\right)\right]^{-1} \tag{6-2}$$

where ρ denotes the water density in unit of g/m^3, $y = \left(\varepsilon' + 2\right)\Big/\varepsilon''$.

$$\begin{aligned}
\varepsilon'(f) &= (\varepsilon_0 - \varepsilon_1)\Big/\left[1+\left(f/f_p\right)^2\right] + (\varepsilon_1 - \varepsilon_2)\Big/\left[1+\left(f/f_s\right)^2\right] + \varepsilon_2 \\
\varepsilon''(f) &= (\varepsilon_0 - \varepsilon_1)\left(f/f_p\right)\Big/\left[1+\left(f/f_p\right)^2\right] + (\varepsilon_1 - \varepsilon_2)\left(f/f_s\right)\Big/\left[1+\left(f/f_s\right)^2\right]
\end{aligned} \tag{6-3}$$

where $\varepsilon_0 = 77.66 + 103.3(300/T(K))$, $\varepsilon_1 = 5.48$ and $\varepsilon_2 = 3.51$.

6.3 Discussion

The measured transmitted THz pulses and the corresponding amplitude spectra propagated through the long-path chamber without fog and with dense fog, corresponding to Figs. 6-1b and 6-1c, are shown in Fig. 6-2a and 6-2b. With the highest fog concentration in the sample chamber, the visibility is reduced to approximately 7 m, as shown in Fig. 6-1c. The transmitted THz fog pulse, with only the small relative time delay of 0.6 ps, appears to be almost identical to the clear-air (no-fog) pulse. Previous work [19] has shown that the transit time of the THz pulses has a linear relation with the refractivity and thereby with the density of the water vapor in the chamber. The 0.6 ps delay would correspond to a water vapor density increase of only 0.2 g/m^3. Assuming that this delay could be caused by the fog itself, the corresponding fog density would be 0.9 g/m^3, as shown by previous calculations [50]. Given the amount of fog solution used by the fog machine, and the 30 minute fog lifetime in the chamber, due to fog evaporation and leakage, we estimate a fog density of 1.1 g/m^3. This density gives a water fog optical loss of 332 dB/km, corresponding to a 7 m attenuation of 2.3 dB, which is too small to explain the 7 m

visibility of Fig. 6-1c.

The ratio of the transmitted amplitude spectra of the fog pulse to the no-fog pulse, shown in Fig. 6-2b, gives the amplitude transmission curve in Fig. 6-3. The measured transmission is relatively flat and does not show much more attenuation in the higher frequency regions, in contrast to the relatively strong frequency dependence of the transmission through water vapor for the same 1.1 g/m^3 water density increase [58]. As shown in Figs. 6-3 and 6-4, the predicted strong monotonically decreasing transmission due to the broadband attenuation calculated for Rayleigh scattering by the water droplets of a fog with same density of 1.1 g/m^3 [50], is in dramatic disagreement with the observations, which show much less attenuation.

Figure 6-4 compares the measured attenuated spectrum with that for the calculated of water vapor absorption with the density increase of 1.1 g/m^3, and for the attenuation predicted for the 1.1 g/m^3 fog only effect. The water vapor result shows increasing attenuation within the range of 0.6 - 0.9 THz. The calculated fog-only transmitted spectrum based on Eq. (6-1) shows increasing strong attenuation across the entire band, much stronger than the observations.

In order to obtain agreement with the mm-THz fog calculations of Liebe [50], shown in Figs. 6-3 and 6-4, the water density would have to be reduced from 1.1 g/m^3 to 0.2 g/m^3. The 1.1 g/m^3 value estimates that one half of the total consumed fog solution resulted in useful experimental fog within the chamber. Clearly this questionable high efficiency could be an over-estimate.

The water fog optical attenuation at 0.2 g/m^3 has been calculated to be 141 dB/km, giving our 7 m visibility an optical power attenuation of 0.99 dB, in disagreement with the strong attenuation shown in Fig. 6-1c. This situation shows that the current understanding of attenuation due to scattering in water fogs, cannot consistently explain our coupled optical and THz measurements. However, the diluted theater fog is expected to optically scatter more than pure water, due to smaller droplets. For undiluted fog solutions, the droplet diameters range from 1 to

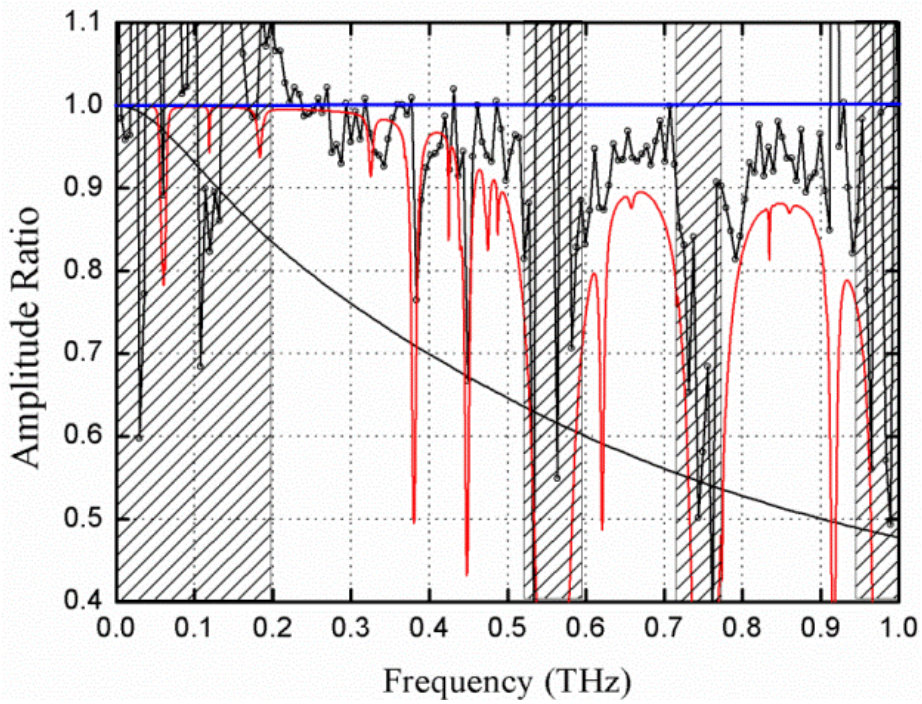

Fig. 6-3. Amplitude transmission (upper black) curve, the ratio of amplitude spectra of Fig. 6-2b, with fog to that without fog. The calculated amplitude transmission (middle red) curve for water vapor density increase of 1.1 g/m^3. The fog attenuation based on Eq. (6-1) (bottom black) (Figure adapted from Ref[23])

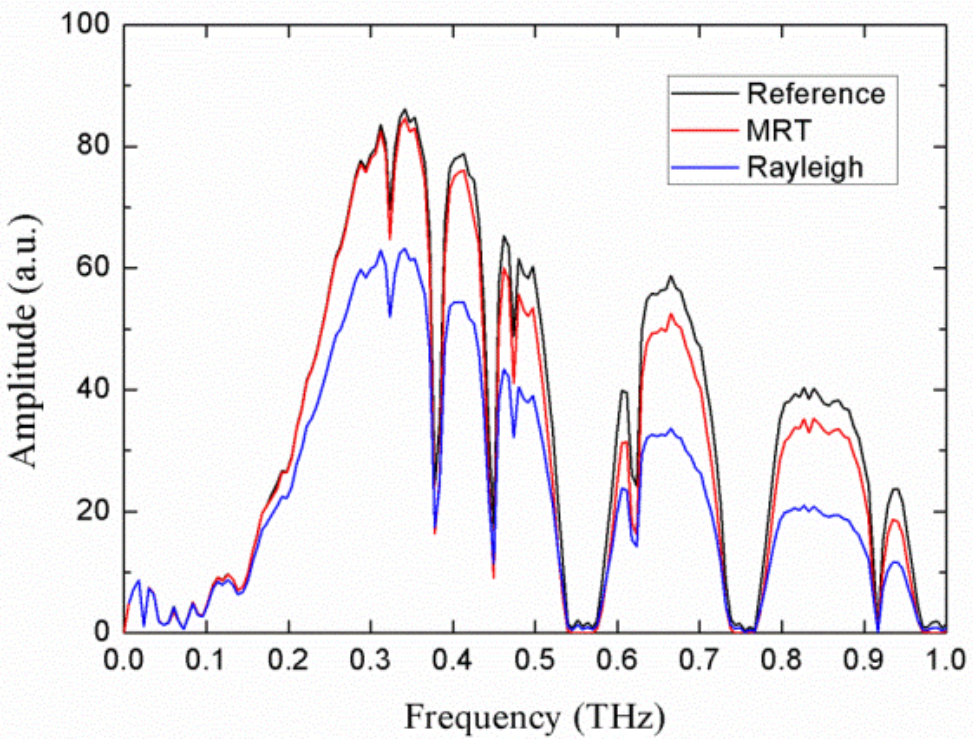

Fig. 6-4. Top black reference curve is without fog. Middle red curve is calculated transmitted spectrum through 137 m of water vapor (1.1 g/m^3). Bottom blue curve is the calculated transmitted spectrum through 137 m of (1.1 g/m^3) fog. (Figure adapted from Ref[23])

2 microns. For our 92% water solution, the diameters would be expected to be larger than 2 microns and smaller than for pure water fog. Finally, the Liebe calculations [50] need to be experimentally validated at THz frequencies.

The THz spectral windows are similar to the reference spectrum, without frequency shifts or additional resonant lines. According to these tentative experimental results, within an optically dense fog the performance of high speed THz wireless communication channels would be maintained, as well as the transparent windows reserved for observation of finger print spectra in remote detection applications. The propagation of broadband THz pulses through a dense fog, shows that broadband THz waves could be also considered as a promising illumination source for many potential applications. For example, THz imaging through a dense fire smoke could guide fire-fighters to the safest path, as well as providing guidance through the extremely dense smoke of a forest fire. Another promising area would be to help the instrument landings for airplanes under severe conditions of fog, or smog, or volcano dust.

In summary, high impact experimental results have been presented. At present, there are many inconsistencies between the previous optical measurements and how they influence THz properties. Much of the published theory has not been experimentally tested, and questions concerning the sample properties remain. However, based on these stimulating results, all areas of questions will be addressed in future work, in order to conclusively document the pre-viewed possibilities for important applications.

6.3.1 Fog, Rain and Scintillations

The effect of rain on direct THz links is approximately 4dB/km for 4 mm/hr, for a calculation based on the ITU-R-Model-2003 [60]. For the seven channels described in this paper, we can use the conservative upper value of 4 dB/km to determine the new 10 dB attenuation lengths for all of the channels in the presence of 4 mm/hr rain. This simple approach adds 4 dB/km to the entire absorption plot shown in Fig. 9a. The resulting new pathlengths in the rain

for a total of 10 dB attenuation mentioned in Fig. 5-10 in Chapter 5 are the following: Channel 1: 96 GHz (2.2 km), Channel 2: 144 GHz (1.9 km), Channel 3: 252 GHz (1.3 km), Channel 4: 342 GHz (630 m), Channel 5: 408 GHz (375 m), Channel 6: at 672 GHz (133 m), and Channel 7: 852 GHz (115 m).

The attenuation of fog with a visibility of 50 m and a density of 0.1 g/m^3 is approximately 0.4 dB at 100 GHz and monotonically rises to the constant value of 4 dB/km for a plateau starting at 700 GHz and extending past 1000 GHz [61]. This dependence gives the additional fog only attenuation for our seven channels of 0.4 dB/km, 0.6 dB/km, 1.3 dB/km, 1,8 dB/km, 2.2 dB/km, 4.0 dB/km, and 4.0 dB/km, at 96, 142, 252, 342, 408, 672, and 852 GHz, respectively. This simple approach adds these values to the attenuations for the channels shown in Fig. 5-10a. The resulting new fog pathlengths with 10 dB attenuation are the following: Channel 1: 96 GHz (10.3 km), Channel 2: 144 GHz (5.1 km), Channel 3: 252 GHz (1.9 km), Channel 4: 342 GHz (730 m), Channel 5: 408 GHz (400 m), Channel 6: at 672 GHz (130 m), and Channel 7: 852 GHz (110 m).

However, if such a fog is associated with the humidity rising to RH 100%, the attenuation of the 7 channels shown in Fig. 5-10a would need to be increased by the factor 100/58 = 1.72, these values added to the fog only attenuations given above. For these large attenuations due to the fog only plus the increase due to the associated 100% humidity, the corresponding 10 dB attenuation, channel lengths are the following: Channel 1: 96 GHz (7.2 km), Channel 2: 144 GHz (3.4 km), Channel 3: 252 GHz (1.2 km), Channel 4: 342 GHz (450 m), Channel 5: 408 GHz (240 m), Channel 6: at 672 GHz (80 m), and Channel 7: 852 GHz (70 m).

For the direct long-path links, it might be expected that scintillations, time varying fluctuations in the refractivity, due to atmospheric temperature and humidity variations, would lead to phase distortions of the transmitted coherent THz pulses and consequent changes in the incoming beam direction. The effect of turbulence on propagating electromagnetic radiation has been predicted theoretically [62], and verified experimentally for propagating IR and optical radiation [63], that the log amplitude variance of amplitude fluctuations due to atmospheric

turbulence varies as $(f)^{7/6}$, with f = frequency.

Consequently, it was quite surprising that the observed mm-wave turbulence effects were more than 2 orders of magnitude larger than expected. This is due to the comparatively very large and frequency independent refractivity of water vapor from microwave frequencies to beyond 1000 GHz [15, 64]. Within this range, the scintillation effect is expected to increase with an essentially linear frequency dependence. An experiment measuring intensity and Angle of Arrival (AOA) effects has been done with a 140 GHz beam over pathlengths of 1.3 km. Also, for a longer 25 km path with a 173 GHz beam, using an interferometric radar system capable of measuring deviations of micro-radians, an AOA distribution with standard deviation of only 10 micro-radians was observed [65]. Consequently, for our proposed longer links scintillation does not appear to be a problem, even though for higher frequencies the problem becomes more severe.

CHAPTER VII

THZ DETECTION OF ATMOSPHERIC SMALL MOLECULE VAPOR

We have measured the rotational signatures of small molecule vapors at frequencies within the atmospheric THz transmission windows, using Long-Tube and Long-Path THz-TDS system. In the Long-Tube system, the THz beam propagates along a 6.68 meter round trip path including a long sample tube of 5.4 meter round trip path for the tested analyte vapor. In the Long-Path system, the THz beam propagates over 170 meter round trip path with analyte vapor contained in a relatively short 1.2 meter round trip path sample chamber. The rotational signatures for each system were described in all of THz windows[14]. For the Long-Tube system, the peak detection sensitivity is sufficient to resolve a 1% absorption feature. For the Long-Path system, the peak detection sensitivity is sufficient to resolve a 3-5% absorption feature. To our knowledge, both of these demonstrations represent the first of their kind for broadband ultrashort THz pulses.

Then we demonstrated broadband THz-TDS monitoring of evolving HDO and D_2O vapor plumes over a 170 m round trip THz propagation path. The measurements show potential for broadband THz real-time sensing of small-molecule vapors with a range of a few hundred meters.

7.1 Introduction

The remote sensing of molecular gases and vapors in the region between 0.1 – 1.0 THz is feasible within THz windows with relatively high transmission, especially at the lower THz frequencies, although the strong absorption of THz radiation by atmospheric water vapor. For RH 34% at 20 ^{o}C (corresponding to water vapor density 5.9 g/m^{3}), the predicted THz propagation length with 10 dB of loss is about 2 kilometers at 0.3 THz and about 125 meters at 0.93 THz. These propagation lengths are potentially useful for gas and vapor sensing applications.

Continuous Wave (CW) techniques have been applied in the THz window from 0.22 – 0.30 THz for active detection of analyte vapors at ground level. Gopalsami et al. developed a millimeter radar chemical sensor based on a BWO source [66]. Using rapid scanning of the BWO they attempted field detection of a methyl chloride plume at a distance of 60 meters from the source. However, THz detection of analyte vapors in the ambient atmosphere using broadband ultrafast THz pulses has not been previously demonstrated.

The current limitations in detection sensitivity, as well as the type of vapors are important to assess the potential of using broadband THz pulses for remote sensing applications. The standard THz-TDS system uses only about 10 mW of optical power to gate each the transmitter and receiver, out of more than 300 mW. A low power beam of THz pulses with 30 nW of average power is generated. Although the returned power was reduced to 130 pW, after a propagation of 170 meters, with losses due to water vapor absorption, coupling back to the receiver, and diffraction losses, determined in Ref. [16], the THz waveform still can be measured with a signal-to-noise ratio (S/N) of 200.

Pressure broadening also limits the THz sensing of vapors in the ambient environment. The relatively light molecules discussed here represent favorable cases because of the small partition functions and large separation between rotational lines. For molecules that can be described as symmetric tops, a 5 GHz FWHM pressure-broadened line width implies that the

rotational constant (total angular momentum) should not be much smaller than 5 GHz in order to at least partially resolve the rotational bands. However, it should be mentioned that the detection of small molecules such as HCN, HCl, H_2S, and CH_2CO, are relevant to the sensing of toxic gases and vapors. Heavier molecules are far more challenging for detection because of their large partition functions and more complex spectra, which tend to merge into broad absorption features at ambient pressure, compromising specificity.

Another challenging problem for remote sensing is the atmospheric fluctuations in humidity, temperature, pressure, and mechanical vibrations. These atmospheric fluctuations can affect the repeatability of signal and reference measurements conducted over a given time duration. There is also uncertainty in projected detection levels of analytes due to uncertainties in the level of moist and dry air continuum absorption which are pressure and temperature dependent, and due to line mixing [67] (collision-induced coupling of energy levels undergoing a transition) which can be significant at ambient pressure.

7.2 THz Detection of Small Molecule Vapor

7.2.1 Experimental Setup

Both Long-Tube and Long-Path THz systems are used for measurement of analyte vapors. For the Long-Tube THz system with a roundtrip path length of 6.7 meters, the analyte vapors sample chamber is 5.4 meter round trip long, as shown in Fig. 7-1a. For the Long-Path THz system with a path of 170 meters, a relatively short 1.2 meter round trip path sample chamber is used for analyte vapors, as shown in Fig. 7-1b. We briefly describe these apparatus below with some modifications for the detection of vapors.

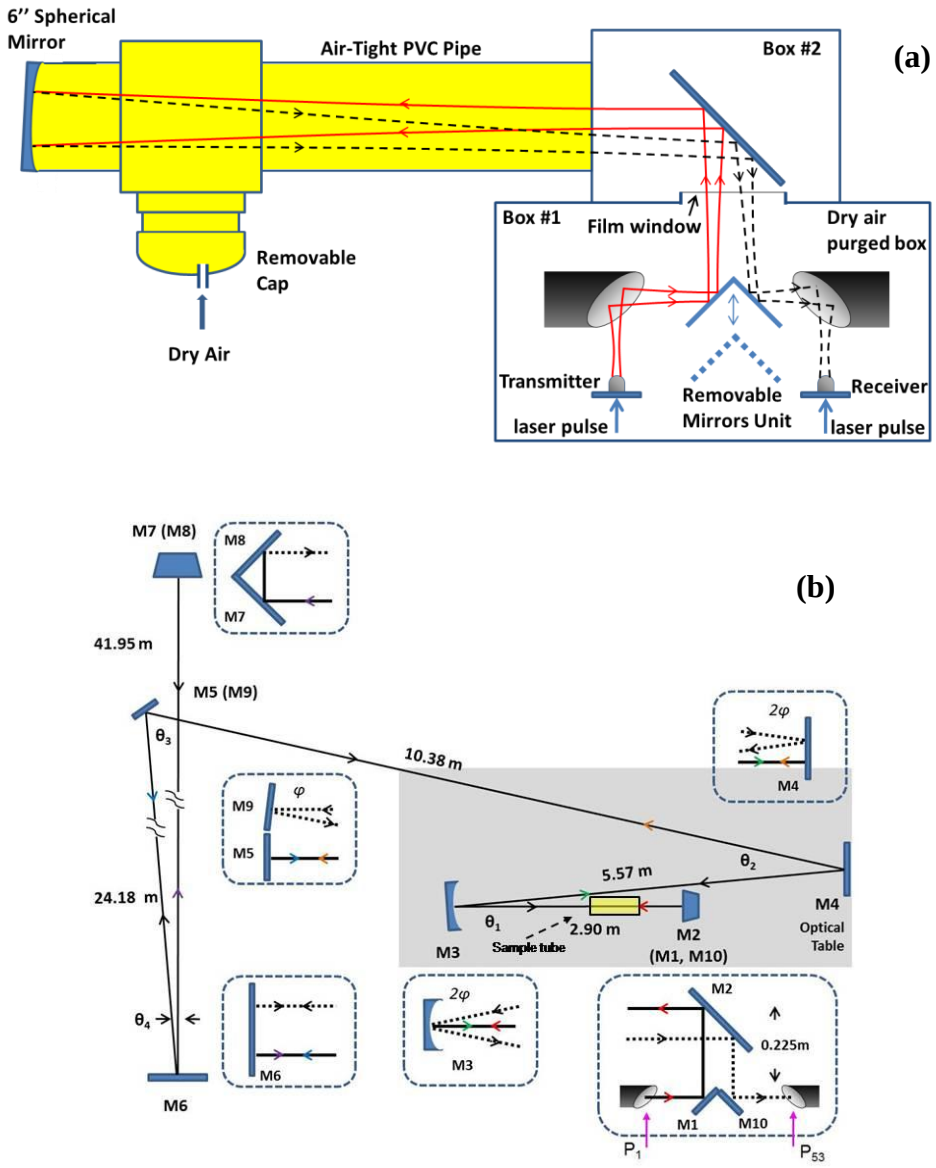

Fig. 7-1 (a). Diagram of the Long-tube apparatus based on a standard THz-TDS spectrometer with 5.4 meter round trip path length enclosed tube for vapor measurements (highlight). (b) Schematic from the top (x-z plane) of the 170 meter round trip long path apparatus with the 1.2 m sample chamber (highlight). (Figure adapted from Ref[14])

The measurement sequence for Long-Tube system is as follows: the tube is first purged with dry air to a reach a desired relative humidity. Then the tube is sealed for subsequent THz waveform measurements. For measurements at ambient humidity, laboratory air is first circulated through the tube for several minutes. Reference scans are measured over a scan length of 166 ps corresponding to spacing between points in the frequency domain of 6.1 GHz. The sample vapor is then introduced and signal scans are measured over the same time base. Typically, four reference and signal waveforms are averaged. The averages are then zero-padded to 1650 ps and Fourier transformed to obtain spectral amplitudes. The zero-padding performs an interpolation in the frequency domain but does not improve the spectral resolution.

The data acquisition parameters used in the Long-Tube measurements is also used in the Long-Path measurements. The following sequence is used to perform Long-Path measurements of analyte vapors contained in the sample tube. The THz pulse train then propagates through the 170 meter path making a double pass through the sample cell containing only ambient laboratory air. The returned pulse is measured as the reference. After measurement of typically six to eight reference waveforms the sample tube is loaded with an analyte vapor through a small hole in the side of the tube. The signal waveform is then measured and repeated six to eight times. From these measurements the average signal and reference spectral amplitudes are calculated.

In general, for measurements in the time domain, changes in the starting time of the measured signal cause frequency-dependent phase changes in the corresponding complex spectra. However, if there is no significant time drift during the time duration of the measurement, the amplitude spectra of the corresponding signals do not change. Consequently, averaging of many pulses should involve averaging of their amplitude spectra.

7.2.2 Long-Tube System Results and Discussion

The first example of a long-tube vapor measurement is for acetonitrile (CH_3CN) vapor. CH_3CN is a symmetric top molecule and its rotational spectroscopy has been well studied using high resolution methods [68]. For the case of atmospheric pressure broadening the rotational constant B is approximated as 9.199 GHz, which leads to a manifold of equally spaced rotational transitions separated by twice the rotational constant, 18.40 GHz.

Figure 7-2a shows the signal waveform (average of four measurements) where the long-tube sample chamber contains CH_3CN at a concentration of approximately 200 parts per million (ppm). The RH in the sample tube was 14%. The waveform contains two components. The highly oscillatory pattern with large amplitude at early times is due to the interaction with the rotational transitions of water vapor. This signal decays sufficiently to expose a second component which consists of echo-like pulses centered near 79 ps and 133 ps. The echo pulses are a consequence of the coherent excitation of (nearly) equally spaced rotational transitions of the symmetric top molecule. Such echoes in THz transients were first observed by Harde et al. [69] and subsequently by Mittleman et al. [70], both using THz beams contained in a standard THz-TDS spectrometer, and without interference from water vapor. The observed recurrence time τ, is approximately 54 ps, which corresponds to the inverse of the frequency spacing ($\Delta\tau$ = 1/18.40 GHz)) between rotational bands. The decay of the echo pulses is to first order related to the collision broadened linewidth. We note that for the 6.7 meter path the echo pulses are easily observable at the low RH of 14% in the sample tube. At significantly higher RH the interference from the stronger water vapor signal would tend to obscure the echo pulses.

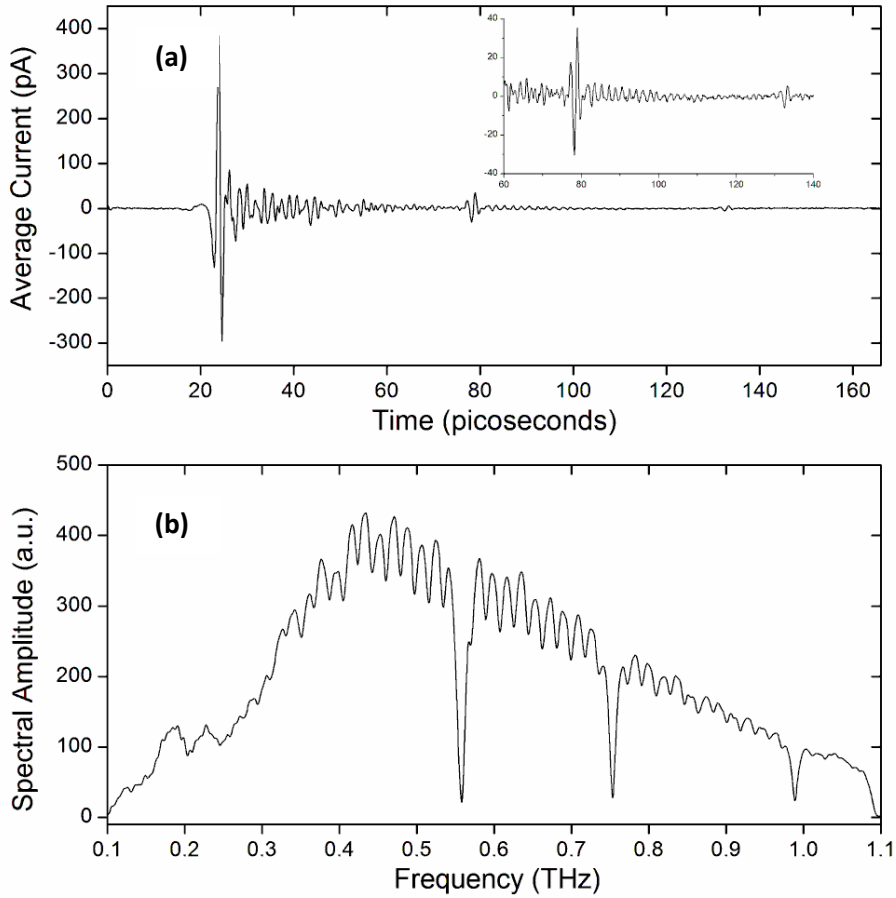

Fig. 7-2. (a) Measured THz signal propagated through chamber with CH_3CN. (b) Corresponding spectral amplitude for CH_3CN. The RH in the chamber was 14%. The inset shows the time base expanded in the echo region. (Figure adapted from Ref[14])

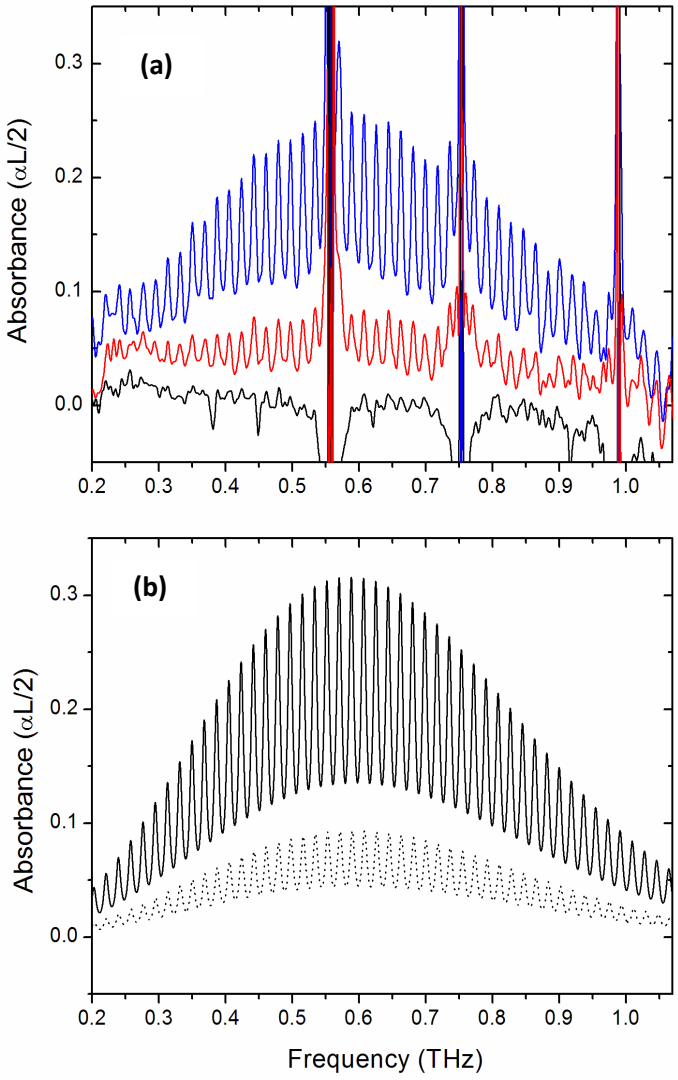

Fig. 7-3. (a)Amplitude absorbance spectra for CH_3CN vapor contained in the long -tube at three concentrations: 200 ppm (top blue curve), 50 ppm (middle red curve), and 12 ppm (bottom black curve). (b) Calculated absorbance spectrum for CH_3CN. The solid curve is the sum of the contributions from CH_3CN in the ground vibrational state and excited vibrational state v8=1. The dotted curve is the calculated spectrum from CH_3CN (v8=1). (Figure adapted from Ref[14])

Figure 7-2b shows the Fourier transform of the waveform. Here, the spectral amplitude clearly shows the equally spaced rotational absorption bands. Superimposed on the spectrum is the nearly complete absorption due to the strong water vapor transitions at 0.55 THz, 0.75 THz, and 0.98 THz.

Figure 7-3a shows amplitude absorbance spectra for CH_3CN vapor at three concentrations inside the sample tube: 200 ppm, 50 ppm and 12 ppm [71]. The amplitude absorbance is the natural logarithm ($\alpha L/2$) of the ratio of the signal amplitude spectrum to the reference amplitude spectrum. These measurements were made at a much higher RH of 51%. The strong modulations in the spectrum are due to the incomplete removal of saturated water vapor absorption. At the highest concentration the rotational manifold of CH_3CN is clearly observed. The $J \rightarrow J+1$ bands are not fully resolved because of the combined pressure and instrument broadening. We also note that each absorption band contains a superposition of non-degenerate $K \rightarrow K$ transitions, which add slightly to the width of the absorption bands. In the region where S/N is the highest (0.4 – 0.7 THz) the frequencies can be measured with a precision of about ± 0.5 GHz.

As the CH_3CN vapor concentration is lowered to 50 ppm the amplitude absorbance becomes correspondingly smaller. The limit of our detection sensitivity occurs near a concentration of approximately 12 ppm, where an experimental amplitude absorbance of about 1% is measured with S/N~1. The negative amplitude absorbance near the water vapor lines is resulted from a slight increase in the humidity level in the sample tube during the data collection for the 12 ppm sample.

We compare the experimental spectrum for CH_3CN to the theoretically predicted spectrum using database values for the CH_3CN line frequencies and line intensities that are tabulated in the JPL spectral line catalog [9]. The absorption coefficient between pairs of J, K levels in CH_3CN can be calculated using

$$\alpha^{v}_{J,K}(\nu) = S^{v}_{J,K} \cdot g(\nu) \cdot N \cdot P_o, \tag{7-1}$$

where $a^{v}_{J,K}(\nu)$ is in cm^{-1}, $S^{v}_{J,K}$ is the line intensity (cm^{-1}/molecule cm^{-2}) for a J→J+1, K→K transition, the index v represents the vibrational state, N is the number density (molecules/(cm^3-atm)), P_0 is the partial pressure of the analyte vapor (atm), and g(ν) is the Lorentz lineshape function,

$$g(\nu) = \frac{1}{\pi}\left[\frac{\Delta\nu}{(\nu_{J,K} - \nu)^2 + \Delta\nu^2}\right], \tag{7-2}$$

with transition frequency $\nu_{J,K}$, and, for simplicity, the half width Δν is taken to be the sum of the pressure broadening and a Lorentzian-type instrumental width $\Delta\nu_p + \Delta\nu_{instr}$. The spectrum is obtained by summing over J,K states and vibrational states v. For our calculation we only consider the ground vibrational state v=0 and the low frequency mode v8=1, for which the values of transition frequency and line intensity are available in the JPL catalog,

$$\alpha(\nu) \approx \sum_{J,K} [\alpha^{v=0}_{J,K}(\nu) + \alpha^{v8=1}_{J,K}(\nu)]. \tag{7-3}$$

The frequency-dependent offset of the CH3CN (v8=1) rotational bands slightly broaden the rotational bands in the summed spectrum, and to add to the absorption pedestal. The calculated peak amplitude absorbance of 0.31 is in approximate agreement with the peak experimental absorbance of 0.25. However, the calculated absorbance does not contain contributions from CH3Cn (v9-2). A comparison of the peak band frequencies of experimental and calculate spectra shows agreement to within 1 GHz.

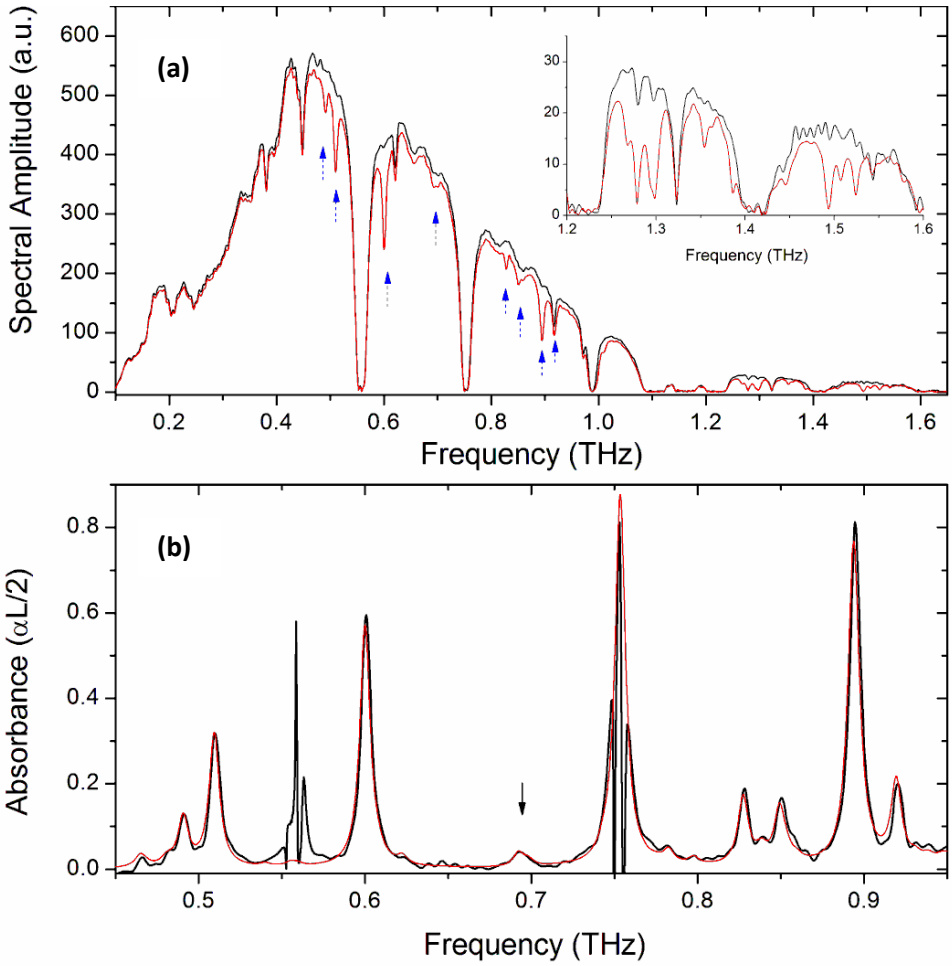

Fig. 7-4. (a) Spectral amplitudes for the reference (top black curve) and signal (red curve) for D_2O sample with a vapor concentration of 750 ppm and at RH = 51%. The inset shows absorption resonances in the expanded higher frequency range. (b) Experimental amplitude absorbance spectrum (black curve) and JPL fitting (red curve). (Figure adapted from Ref[14])

In the second example described below in Fig. 7-4, drops of liquid D_2O were introduced into the sample tube containing laboratory air at RH = 51%. The evaporation of the drops was facilitated by slightly heating the tube from underneath. Assuming complete vaporization, the volume of liquid corresponds to a vapor concentration of approximately 750 ppm in the sample tube volume. Figure 7-4a shows the reference spectral amplitude (top black curve, no D_2O present) and the signal spectral amplitude (bottom red curve, with D_2O present). There are twelve absorption dips in the region between 0.4 – 1.0 THz due to the analyte vapor. Eight of these are indicated by the blue arrows. The inset to Fig. 7-4a shows the frequency region between 1.2 – 1.6 THz, where the spectral amplitude returned to the receiver is relatively small, but still sufficient to observe an additional eight absorption lines. The best fit is shown as the red curve in Fig. 7-4 and corresponds to a ratio of 22:1 HDO : D_2O. An isolated D_2O absorption near 0.693 THz is indicated by the black arrow in Fig. 7-4.

7.2.3 Long-Path System Results and Discussion

The measurement of target vapors over the much longer 170 meter round trip path is more challenging because of increased water vapor absorption, greater fluctuations in humidity, and thermal and mechanical fluctuations leading to variations THz pulse path length. In this section we investigate the ability of the long-path apparatus outlined in Fig. 7-1b to measure the rotational spectra of CH_3CN and the HDO/D_2O mixture. Figure 7-5 compares spectral amplitudes for the reference (upper black curve) where the sample chamber (1.2 meter round trip path length) contains ambient air only and signal (lower red curve) where the sample chamber contains CH_3CN vapor at a concentration of 800 ppm mixed with ambient air. The higher concentration is used to achieve similar absorption strength as for the 4.5 times longer PVC tube. Each of the curves is the average of six separate measurements. The laboratory RH was 50%.

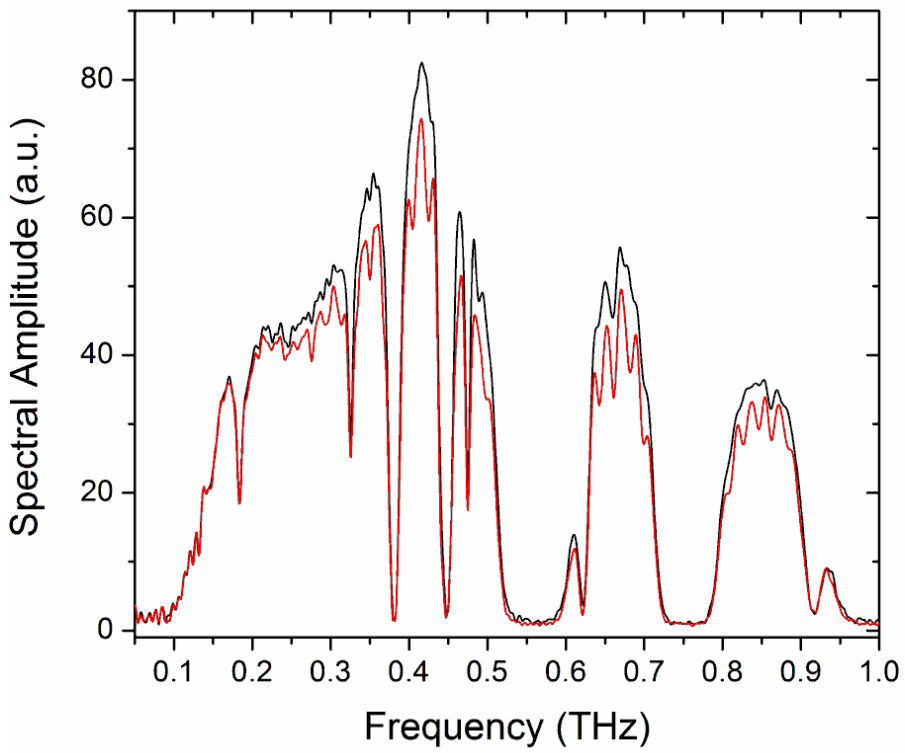

Fig. 7-5. Spectral amplitudes for the reference (upper black curve) and the CH_3CN sample (lower red curve) for the 170 meter path measurement. The concentration of acetonitrile is 800 ppm in the sample tube. The laboratory relative humidity was 50%. (Figure adapted from Ref[14])

Within the transmission windows several of the rotational absorption bands are clearly observed as dips in the spectral amplitude signal.

In the measurement, six reference waveform scans were collected first (no CH_3CN in the chamber) and the spectral amplitudes averaged to obtain the reference spectrum. CH3CH was then introduced to the chamber and allowed to equilibrate, and six signal waveforms collected and the spectral amplitudes averaged to obtain the signal spectrum. As a check of the system and environmental stability, a second set of reference scans were taken. Typically we found that the two sets of reference spectra showed agreement to within 5%. A full sequence of measurements required about 1 hour to complete.

The final example shown below in Fig. 7-6 is the detection of a HDO/ D_2O vapor mixture contained in the sample chamber within the 170 meter THz path. Here, D_2O liquid is initially evaporated in the sample chamber in an amount equivalent to a vapor concentration of approximately 3000 ppm. As before, the four-fold larger concentration (compared to the long-tube measurement) is used to compensate for the shorter interaction path. Figure 7-6 (black curve) shows the experimental amplitude absorbance for the HDO/ D_2O mixture in the presence of 50% RH. The result is the average of eight measurements. Despite the much increased effect of water vapor absorption and lower S/N compared to the corresponding long-tube measurement, seven absorption lines marked by blue arrows can be distinguished from the noise floor and are due to the analyte vapors. The red curve is the fit to the experimental spectrum based on a superposition of HDO and D_2O database line frequencies and relative line intensities. The best fit occurs for a 2.4:1 ratio of HDO: D_2O. Also from the fit we find that the accuracy of the experimental line frequencies is within 1.5 GHz of the JPL catalog values. This finding is an indication the stability of the long-path apparatus over the approximate 1 hour time to perform the measurements.

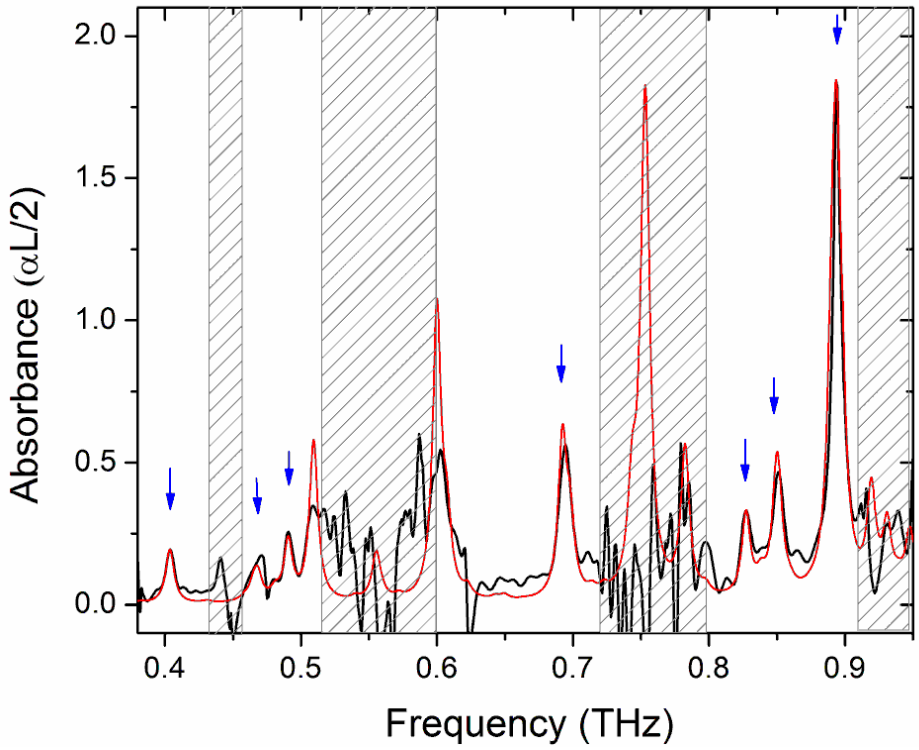

Fig. 7-6. Experimental amplitude absorbance spectrum (black curve) where D_2O liquid is introduced into the 1.2 m (round-trip) sample chamber to give a concentration of approximately 3000 ppm. The red curve indicated a relative fraction of HDO: D_2O of 2.4:1. (Figure adapted from Ref[14])

It's useful to discuss the sensitivity of the long-path system to the detection of various small molecule gas/vapor analytes. With respect to Eq. 7-1, we use the molecular cross section (cm^2/molecule) $\sigma_{i,j} = S_{j,k} g$ for a transition between states i and j, and the column density, $u = NP_o L$ (molecules/cm^2). From this we estimate the column density needed to detect an analyte using the ~3% criterion for amplitude absorption (~6% power absorption). For CH_3CN in the ground vibrational state we consider the rotational band corresponding to the J=36→37 transition in the transmission window near 0.680 THz. A HWHM width of 5 GHz for the combined pressure broadening and instrumental broadening is used for the lineshape factor, g. Summing over the K→K transitions contained in the JPL database yields an absorption cross section of approximately 1.7×10^{-19} cm^2/molecule (scaled for the fractional abundance of CH_3CN), which yields a column density of 3.6×10^{17}molecules/cm^2 (equivalent to 140 ppm-m) needed for a 3% amplitude absorption. This may be compared to cases of a relatively strong absorbing gas, such as HCN, and a relatively weak absorbing gas, such as H_2S. For these molecules we use values from the JPL database scaled for the main isotopologue. The vibrational partition function is not considered here. For isolated rotational lines in transparency windows we find for HCN with $\nu \approx 0.886$ THz and $\Delta\nu = 3.5$ GHz: $\sigma \approx 1.7\times10^{-18}$ cm^2/molecule; and for H_2S with $\nu \approx 0.708$ THz and $\Delta\nu = 5$ GHz: $\sigma \approx 8.7\times10^{-21}$ cm^2/molecule. For a 3% amplitude absorption the column densities are approximately 5.3×10^{16} molecules/cm^2 (21 ppm-m) for HCN and 6.9×10^{18} molecules/cm^2 (2800 ppm-m) for H2S. For our current system setup, using a 120 ms acquisition time per waveform time step, a minimum of 75 seconds is required to collect a 625 step waveform. To acquire a set of eight signal and eight reference scans for a 3% sensitivity to absorption would require a minimum of 20 minutes.

7.3 Remote THz Monitoring of an Evolving Gas-Phase Mixture

Our goal in this project is to investigate ability of Long-Path THz-TDS system to monitor an evolving vapor plume under ambient atmospheric conditions at 1 atm pressure and RH of 30-50%. The classical exchange reaction between H_2O and D_2O was monitored as [72]:

$$D_2O(g) + H_2O(g) \xrightarrow{k_r} 2HDO(g) \tag{7-4}$$

where k_r is the reaction rate. As shown in Figs. 7-4 and 7-7, the well separated rotational absorption lines of D_2O, HDO and H_2O can be observed in the atmospheric THz windows below 1 THz. And the reactants and products concentration can be determined by center frequency position and amount of power absorption line.

Upon comparison with the JPL catalog [9], we find that the majority of the line frequencies agree with the rotational transitions of semi-heavy water vapor, HDO. In the presence of H_2O the H and D atoms will rapidly exchange according to the reaction: $H_2O + D_2O \leftrightarrow 2HDO$. In the presence of excess H_2O the equilibrium will be driven to increase the concentration of HDO. The conversion to HDO is likely facilitated by interaction with H_2O. To determine the extent of the conversion we fit the experimental absorbance spectrum to a superposition of D_2O and HDO absorbance spectra using the line frequencies and line intensities from the JPL catalog [9] and varied the ratio of HDO: D_2O spectra to obtain a best fit. The fit shown in Fig. 7-4 for Long-Tube system implies that about 92% of D_2O has converted to HDO. In the case of Long-Path system, a smaller percentage, about 45%, of the initial D_2O introduced to the tube has converted to HDO as shown in Fig. 7-7. The closeness of the fit to the experimental spectrum indicates the stability of the THz-TDS long-tube apparatus and confirms the ability to determine the line frequencies with accuracy better than 1 GHz in the spectral range shown.

The fundamental studies for the exchange kinetics of gas-phase are important, because D_2O / H_2O exchange kinetics has been well-studied in the condensed phase, but relatively few

measurements have made in the gas phase. For Liquid phase, reaction rate typically on $(millisecond)^{-1}$ scale at room temperature. For Gas Phase, reaction rate on $(100\text{-}1000\ second)^{-1}$ scale at room temperature.

7.3.1 Determination of Decay Time of Sample Chamber

Firstly, in order to obtain the life time of sample chamber, 20 ml of HDO liquid were evaporated into sample chamber for RH 30% at 20 ^{o}C. The total volume of sample chamber which is converted from hallway is 291.7 m^3, which corresponding to 100 ppm initial concentration in chamber. A set of 7 continuous scans are shown in Fig. 7-8, with a scan time of 5 min. Inset of Fig. 7-8 shows the increasing spectral amplitude of absorption line at 0.890 THz due to reduced concentration of HDO.

By exponential fitting the decreased absorbance of absorption lines at 0.510 THz and 0.895 THz, two chamber decay times are obtained as 12.6 min and 13.7 min. The average chamber decay time τ_c = 13.2 min. It is noteworthy that the sensitivity of Long-Tube THz system is about 5 ppm.

7.3.2 Measurements of Reaction Rate of D_2O *and* H_2O

30 ml of D_2O was evaporated into chamber at RH 30% at 20 ^{o}C, using 4 hotplates which are uniformly distributed along the sample chamber. A set of 5 continuous scans with 1 min scan interval have been obtained. As shown in Fig. 7-8, D_2O lines can be easily observed in reference signals at the start. From scan #2, D_2O lines decreased enormously due to the reaction and decay time of chamber, while HDO lines appear clearly as marked by red arrows.

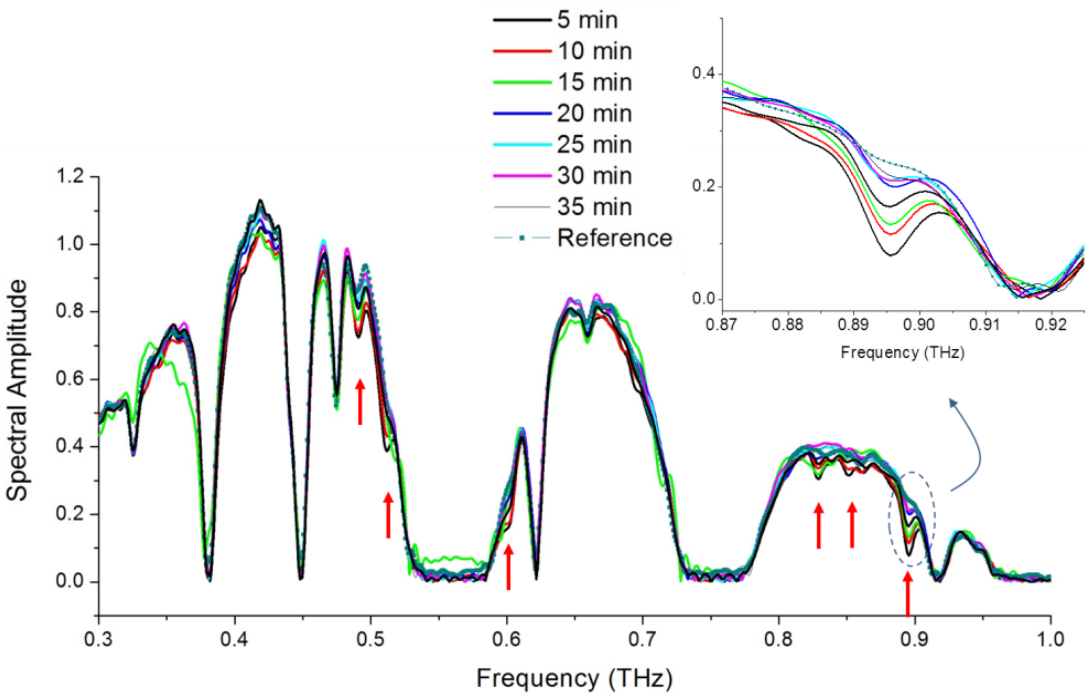

Fig. 7-7. Frequency spectra of set of 7 continuous scan of HDO sample using Long-Tube system. Inset shows the increasing amplitude at absorption line at 0.895 THz. (Figure adapted from Ref. [72])

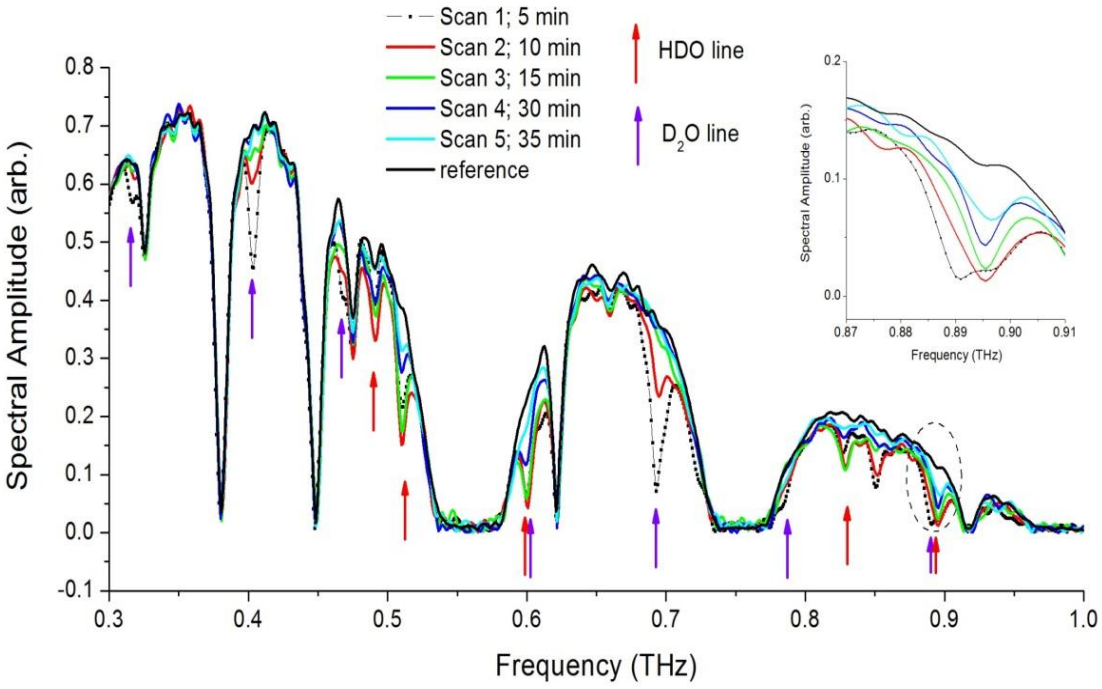

Fig. 7-8. THz-TDS monitoring of an evolving D_2O plume. Purple arrows mark the D_2O lines and the red arrows marks HDO lines. The inset shows the transition indicated by change of line center frequency. (Figure adapted from Ref. [72])

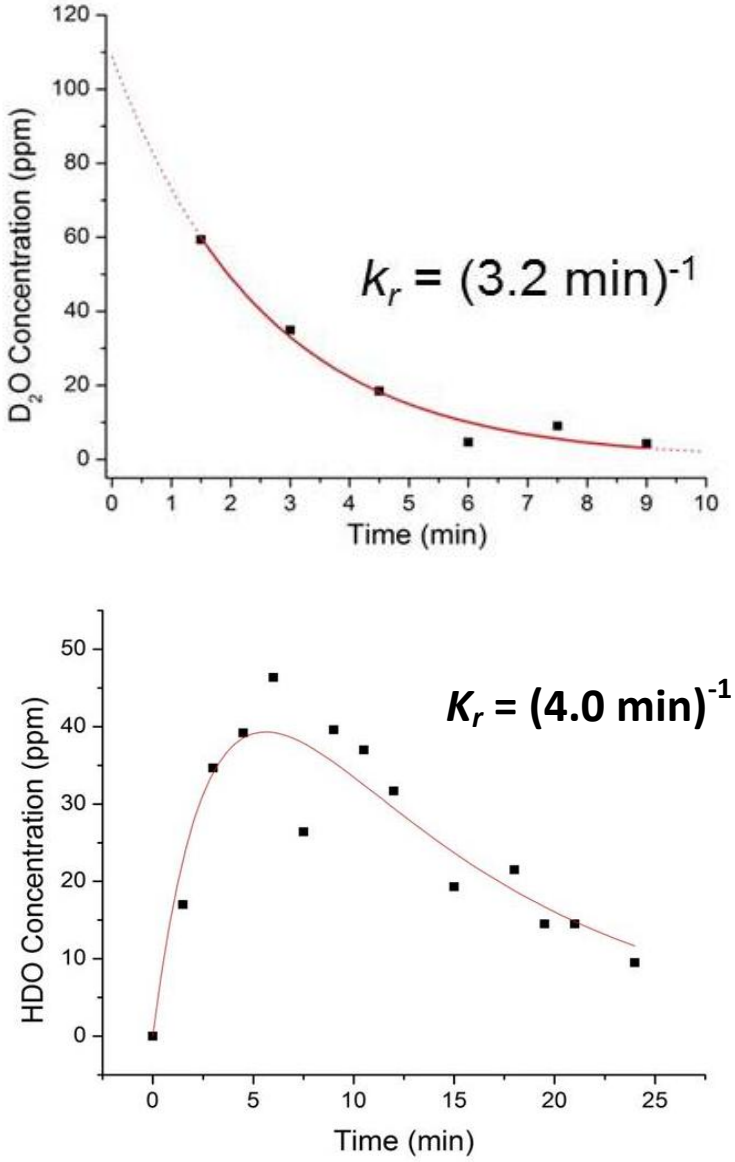

Fig. 7-9. (a) Reaction rate calculated based on D_2O decay curve. (b) Reaction rate calculated based on HDO changing curve. (Figure Adapted from Ref. [72])

Combine both of chamber delay time and reaction rate, the absolute decay rate for D_2O and HDO can be written as [72]:

$$\begin{aligned}\frac{d[D_2O]}{dt} &= -(k_r + k_c)[D_2O] \\ \frac{d[HDO]}{dt} &= 2k_r[D_2O] - k_c[HDO]\end{aligned} \tag{7-7}$$

then the corresponding concentration decay rate can be written as exponential curve:

$$\begin{aligned}[D_2O](t) &= [D_2O]_0 e^{-(k_r+k_c)t} \\ [HDO](t) &= 2[D_2O]_0 \left(1 - e^{-k_r t}\right) e^{-k_c t}\end{aligned} \tag{7-8}$$

Using Eq. (7-8), we can calculate the reaction rate k_r from both D_2O and HDO as shown Fig. 7-9. The average reaction rate k_r of 3.6 min^{-1} is approximate 2X faster than k_r determined from NMR measurements of D_2O / H_2O vapor contained in NMR tube.

Here, we demonstrated broadband THz-TDS monitoring of evolving HDO and D_2O vapor plumes over a 170 m round trip THz propagation path, with a sensitivity of 10 % amplitude absorption (5 minute integration time). The detection limit reaches 5 ppm HDO over 132 meter round trip path through plume. The measurements show potential for broadband THz sensing of small-molecule vapors with a range of a few hundred meters. The future plan is to improve S/N by at least an order of magnitude, since only about 10 mW of optical power is used of the 300 mW available. The experimental result shows that THz-TDS monitoring of reaction kinetics within a vapor plume is possible. More accurate measurement of rate constants will obtain using faster waveform scanning.

CHAPTER VIII

SUMMARY AND FUTURE PROSPECTS

In this Thesis, I have experimentally and theoretically investigated the THz radiation absorption from water vapor resonant absorption, continuum absorption and scattering loss by suspended particles, which determine the maximum propagation distance of THz pulses in the atmosphere. The reshaping of propagating broad-bandwidth short THz pulses is controlled by both the refractivity and the absorption of water vapor resonant dispersion. With this quantitative knowledge of the above atmospheric effects on THz pulses propagation, we can design free-space THz applications and analyze their performance based on the atmospheric limits.

The total water vapor resonant line absorption can be calculated as the sum of all of the individual resonant lines with the corresponding molecular parameters. The Molecule Response Theory (MRT) has been experimentally proven to be the most accurate lineshape model to well fit the measured absorption line associated with the professional spectroscopic database HITRAN for the most accurate values of the parameters, such as intensity, line center frequency and line width. The MRT lineshape model includes the molecular orientation time τc during a collision and changes smoothly from van Vleck-Weisskopf (vV-W) lineshape near the line center to Full Lorentz (FL) lineshape at far wings of the resonant line. The MRT lineshape overcomes the disadvantage of the unphysical far-wing of the vV-W lineshape, as well as the under-estimated absorption from the vV-W lineshape with a cutoff.

From the result of simulation, the frequency spectra below 1 THz are divided into seven regions called transparent THz windows by water vapor resonant absorption lines, and the attenuation increase as the frequency increase. For atmosphere at 20 ℃ and RH 58% which is equivalent to a water vapor density of 10 g/m^3, the power attenuation at 0.3 THz is less than 5 dB/km, but the power attenuation at 0.85 THz is about 60 dB/km.

In additional to the resonant absorption, atmosphere water vapor also includes another kind of attenuation on THz spectra called continuum absorption. The continuum absorption covers the entire broadband frequencies and can be observed within the transparent THz windows. The continuum absorption cannot be explained by far-wing absorption of the resonant lines. It is still not clear how the continuum absorption is derived. But, it has been experimentally verified to have a quadratic frequency dependence and to be a combination of two ambient air pressure terms. The empirically determined continuum absorption is usually defined as the difference between the measured total absorption and the calculated absorption of the resonant lines. The determined continuum absorption depends strongly on the lineshape function, number of lines, line intensities and linewidth chosen for the line-by-line summation method. In the latest report, the continuum absorption reaches nearly 30 dB/km of power attenuation at 0.85 THz at 20 ℃ and RH 58% which is half of the corresponding resonant absorption. However, below 0.3 THz, the continuum absorption has higher attenuation than resonant absorption.

Besides atmospheric water vapor, different weather conditions bring various particles into atmosphere, such as fog, dust, rain and snow, which also influence the propagated THz pulses. The physical understanding of this phenomenon is relatively simple, and mostly depends on the comparison between the wavelength and the distributed particle sizes.

Recent work demonstrates that artificial fog with a visibility of 7 m attenuates the amplitude of THz pulses transmitted through 137 m by only 10%. Based on the observations of fog and cloud droplet size distributions, we can understand the broadband THz pulses can

propagate through dense of atmospheres of fog and clouds, with certain propagation loss, due to Rayleigh scattering. The fog particles are generally considered to be less than 50 microns in diameter, which is much smaller than the THz wavelengths (300 microns for 1 THz). This property gives THz frequency techniques the opportunity for applications such as imaging through dense fog, clouds and fire smoke, and high data rate wireless communication without interruption by fog, cloud and smoke.

In the future works, we will utilize the complete Molecular Response Time theory, including both MRT attenuation and MRT-HITRAN phase shift, instead of vV-W-HITRAN phase, for a more precise simulation model. We also plan to continue the experiments of the THz pulses propagation through diffusive medium including fog or smoke environments using the longer life-time chamber and optical power meter. The optical power meter will provide quantitative record of the visibility of diffuse environments, instead of Mie scattering theory. It will lead an investigation on the THz wireless communication, imaging and other applications in different weather conditions, such as imaging in a fire fighting environment, and the possible precise aircraft landing instruments.

Another future plan is the further research on molecule evolving in gas-phase is to improve S/N by at least an order of magnitude, since only about 10 mW of optical power is used of the 300 mW available. More accurate measurement of rate constants will obtain using faster waveform scanning.

REFERENCES

1. P.H.Siegel, "Terahertz Technology," *IEEE Trans. Microwave and Techniques*, **50** (2002)
2. R.Appleby and H.Wallace, "Standoff detection of weapons and contraband in the 100GHz to 1 THz region," *Ieee Trans. Antennas and Propagation*, **55** (2007)
3. J. Wells, "Faster than Fiber: the future of multi-Gb/s wireless," *IEEE Microwve Magazine*, (2009)
4. T.Kosugi, and Y.Kado, "MM-Wave long-range wireless systems," *IEEE Microwave Magazine*, **09** (2009)
5. E.Cianca, T.Rossi, A.Yahalom, Y.Pinhasi, J.Farserotu, and C.Sacchi, "EHF for satellite communications : the new broadband frontier," *Proc. IEEE*, **99**(11), 1858-1881 (2011)
6. D.Grischkowsky, S.Keiding, M.v.Exter, and C.Fattinger, "Far-infrared time-domain spectroscopy with terahertz beams of dielectrics and semiconductors," *J. Opt. Soc. Am. B*, **7**(10), 2006-2015 (1990)
7. V.B.Podobedov and G.T.Fraser, "Investigation of the water-vapor continuum in the THz region using a multipass cell," *J. Quan. Spec. & Rad. Transfer*, **91** (2005)
8. V.B.Podobedov, D.Plusquellic, K.Siegrist, G.Fraser, Q.Ma, and R.H.Tipping, "New measurements of the water vapor continuum in the region from 0.3 to 2.7 THz," *J. Quan. Spec. & Rad. Transfer*, **109**(3), 458-467 (2008)
9. H.M.Pickett, R.L.Poynter, E.A.Cohen, M.L.Delitsky, J.C.Pearson, and H.S.P.Muller, "Submillimeter, millimeter, and microwave spectral line catalog," *J. Quan. Spec. & Rad. Transfer*, **60**(5), 883-890 (1998)
10. L.Rothman, I.Gordon, A.Barbe, D.Benner, P.Bernath, M.Birk, V.Boudon, L.Brown, A.Campargue, J.Champion, K.Chance, L.Coudert, V.Dana, V.Devi, S.Fally, J.Flaud, R.Mikhailenko, C.Miller, N.Moazzen-Ahmadi, O.Naumenko, A.Nikitin, J.Orphal, V.Perevalov, A.Perrin, A.Predoi-Cross, C.Rinsland, M.Rotger, M.Simeckova, M.Smith, K.Sung, S.Tashkun, J.Tennyson, R.Toth, A.Vandaele, and J.V. Auwera, "The HITRAN

2008 molecular spectroscopic database," *J. Quan. Spec. & Rad. Transfer*, **110**(9-10), 533-572 (2009)

11. D.E.Burch and D.A.Gryvnak, "Continuum absorption by water vapor in the infrared and millimeter resions," *Proc. of the International workshop on atmospheric water vapor*, 47-76 (1979)
12. P.W.Rosenkranz, "Water vapor microwave continuum absorption: a comparison of measurements and models," *Radio Sci.*, **33**(4), 919-928 (1998)
13. S.Paine, R.Blundell, D.Papa, J.Barrett, and A.Radford, "A Fourier transform spectrometer for measurement of Atmospheric transmission at submillimeter wavlengths," *Publ. Astron. Soc. Pac.*, **112**(767), 108-118 (2000)
14. J.S.Melinger, Y.H.Yang, M.Mandehgar, and D.Grischkowsky, "THz detection of small molecule vapors in the atmospheric transmission windows," *Opt. Express*, **20**(6), 6788-6807 (2012)
15. D.Grischkowsky, Y. Yang, and M.Mandehgar, "Zero-frequency refracitivity of water vapor, comparison fo Debye and van-Vleck Weisskopf theory," *Opt. Express*, **21**(16), 18899-18908 (2013)
16. Y. Yang, A.Shutler, and D.Grischkowsky, "Measurement of the transmission of the atmosphere from 0.2 to 2 THz," *Opt. Express*, **19**(9), 8830-8838 (2011)
17. Y. Yang, M.Mandehgar, and D.Grischkowsky, "Broadband THz Pulse Transmission through the Atmosphere," *IEEE Trans. THz Sci. Technol.*, **1**(1), 264-273 (2011)
18. Y. Yang, M.Mandehgar, and D.Grischkowsky, "Understanding THz Pulse Propagation in the Atmosphere," *IEEE Trans. THz Sci. Technol.*, **2**(4), 406-415 (2012)
19. Y. Yang, M. Mandehgar, and D. Grischkowsky, "Time domain measuremetn of the THz refractivity of water vapor," *Opt. Express*, **20**(24), 26208-26218 (2012)
20. J.H.V. Vleck and V.F.Weisskopf, "On the shape of collision-broadened lines," *Rev. Mod. Phys*, **17**(2-3), 227-236 (1945)
21. M.Mandehgar, Y. Yang, and D.Grischkowsky, "Atmosphere characterization for simulation of the two optimal wireless terahertz digital communication links," *Opt. Lett.*, **38**(18), 3437-3440 (2013)
22. P.Debye, "Polar Molecules," *(Dover Publications: New York),* (1957)
23. Y. Yang, M.Mandehgar, and D.Grischkowsky, "Broadband THz Signals Propagate through Dense Fog," *Photonics Technology Letters*, **Submitted** (2014)
24. C.H.Townes and A.L.Schawlow, "Microwave Spectroscopy," *(Dover Publications: New York),* (1975)

25. R.J.Hill, "Water vapor absorption line shape comparison using the 22-GHz line: the Van Vleck-Weisskopf shape affirmed," *Radio Science*, **21** (1986)
26. J.H.v. Vleck, "The absorption of microwaves by oxygen," *Phys. Rev*, **71**(7), 413-424 (1947)
27. D.M.Slocum, E.J.Slingerland, R.H.Giles, and T.M.Goyette, "Atmospheric absorption of terahertz radiation and water vapor continuum effects," *J. Quan. Spec. & Rad. Transfer*, **127**(49-63) (2013)
28. L.Essen, "The refractive indices of water vapour, air, oxygen, nitrogen, hydrogen, deuterium and helium," *Proc. Phys. Soc. B*, **66**(189), 189-193 (1953)
29. K.D.Froome, "THe refracitve indices of water vapour, air, oxygen, nitrogen and argon at 72 kMc/s," *Proc. Phys. Soc*, (1955)
30. L.Essen and K.D.Froome, "THe refractive indices and dielectric constants of air and its principal constituents at 24,000 Mc/s," *Proc. Phys. Soc*, (1951)
31. B.R.Bean and E.J.Dutton, "Radio Meterorology," *(National Bureau of Standards)*, (1966)
32. Martin.v.Exter and D.Grischkowsky, "Optical and electronic properties of doped silicon from 0.1 to 2 THz," *Appl. Phys. Lett*, **56**(17), 1694-1696 (1990)
33. A.Deepak, T.D.Wilkerson, and L.H.Ruhnke, "Atmospheric water vapor," *(Academic Press)*, (1980)
34. Y.Scribano and C.Leforestier, "Contribution of water dimer absorption to the millimeter and far infrared atmospheric water continuum," *J. Chem. Phys*, **126** (2007)
35. T.R.Dyke and J.S.Muenter, "Electric dipole moments of low J states of H2O and D2O," *Journal of chemical physics*, **59** (1973)
36. S.L.Shostak, W.L.Ebenstein, and J.S.Muenter, "The dipole moment of water. I. Dipole moments and hyperfine properties of H2O and HDO in the fround and excited vibrational states," *J. Phys. Chem.*, **94**(9), 5875-5882 (1991)
37. C.C.Bradley and H.A.Gebbie, "Refractive index of nitrogen, water vapor, and their mixtures at submillimeter wavelengths," *Applied Optics*, **10** (1971)
38. H.J.Liebe, "The atmospheric water vapor continuum below 300GHz," *Int. J. Infrared Millim. Waves*, **5**(2), 207-227 (1984)
39. M.A.Koshelev, E.A.Serov, V.V.Parshin, and M.Y. Tretyakov, "Millimeter wave continuum absorption in moist nitrogen at temperatures 261-328K," *J. Quan. Spec. & Rad. Transfer*, **112**(17), 2704-2712 (2011)
40. M.Yu.Tretyakov, A.F.Krupnov, M.A.Koshelev, D.S.Makarov, E.A.Serov, and V.V.Parshin, "Resonator spectrometer for precise broadband investigations of

atmospheric absorption in discrete lines and water vapor related continuum in millimeter wave range," *Rev. Sci. Instrum*, **80**(9), 093106 (2009)

41. Y. Yang, M.Mandehgar, and D.Grischkowsky, "Determination of the water vapor continuum absorption by THz-TDS and Molecular Response Theory," *Opt. Express*, **22**(4), 4388-4403 (2014)
42. H.Harde, N.Katzenellenbogen, and D.Grischkowsky, "Line-shape transition of collision broadened lines," *Phys. Rev. Lett.*, **74**(8), 1307-1310 (1995)
43. H.Harde, R.A.Cheville, and D.Grischkowsky, "Terahertz studies of collision-broadened rotational lines," *J. Phys. Chem. A*, **101**(20), 3646-3660 (1997)
44. Y. Yang, M.Mandehgar, and D.Grischkowsky, "THz-TDS Characterization fo the Digital Communication Channels of the Atmosphere and the Enabled Applications," *J. Infrared Milli. Terahz. Waves*, **to be published** (2014)
45. Y. Yang, M.Mandehgar, and D.Grischkowsky, "Determination of Water Vapor Continuum Absorption, Using Long-Path THz-TDS without the Cross-Term," *IRMMW-THz 2014*, (2014)
46. T.Kurner and S.Briebe, "Towards THz Communications - Status in Research, Standardzation and Regulatin," *J. Infrared Milli. Terahz. Waves*, **35** (2014)
47. M. Gebhart, and C. Chlestil, "Measurement of Light Attenuation in dense fog conditions for FSO applications," *Proc. of SPIE*, (2005)
48. B. Flecker, and C. Chlestil, "Results of Attenuation-Measurements for Optical Wireless Channels under Dense Fog Conditions Regarding Different Wavelengths," *Proc. of SPIE*, (2006)
49. S.Muhammad, M.Awan, and A.Rehman, "PDF Estimation and Liquid Water Content Based Attenuation Modeling for Fog in Terrestrial FSO Links," *Radioengineering*, **19**(2) (2010)
50. H.J.Liebe, T.Manabe, and G.A.Hufford, "Millimeter-Wave atteunation and delay rates due to fog/cloud conditions," *Ieee Trans. Antennas and Propagation*, **37** (1989)
51. H. Vasseur and C. Gibbins, "Inference of Fog Characteristics form Attenuation Measurements at Millimeter and Optical Wavelengths," *Radio Science*, **31** (1996)
52. N. Miles, J. Verlinde, and E. Clothiaux, "Cloud Droplet Size Distributions in Low-Level Stratiform Clouds," *Journal of the Atmospheric Science*, **57** (2000)
53. J. Hudson and S. Yum, "Droplet Spectral Broadening in Marine Stratus," *Journal of the Atmospheric Science*, **54** (1997)

54. R. Eagan, R. Hobbs, and L. Radke, "Particle Emissions From a Large Kraft Paper Mill and Their Effects on the Microstructure of Warm Clouds," *Journal of Applied Meteorology*, (1974)
55. J. Fitzgerald and P. Spyers_Duran, "Changes in Cloud Nucleus Concentration and Cloud Droplet Size Distribution Associated with Pollution from St. Louis," *Journal of Applied Meteorology*, **12** (1973)
56. K. Whiteby, R. Husar, and B. Liu, "The Aerosol Size Distribution of Los Angeles Smog," *Journal of Colloid and Interface Science*, **39** (1972)
57. I. Tegen and A. Lacis, "Modeling of particle size distribution and its influence on the radiative properties of mineral dust aerosol," *Journal of geophysical research*, **101** (1996)
58. M.Ijaz, and E.Bentley, "Modeling of fog and smoke attenuation in free space optical communications link under controlled laboratory conditions," *Journal of Lightwave Technology*, **31** (2013)
59. M.Locatelli, and R.Ferraro, "Imaging live humans through smoke and flames using far-infrared digital holography," *Optics Express*, (2013)
60. ITU-R-Model-2005, "Specific Attenuation Model for Rain for Use in Prediction Methods," (2005)
61. R.Appleby, "Passive millimetre-wave imaging and how it differs from terahertz imaging," *Phil. Trans. of the Royal Society A*, **2013** (2003)
62. R.Lawrence and J.Strohbehn, "A Survey of Chlear-Air Propagation Effects Relevant to Optical Communications," *Proc. of IEEE*, **58** (1970)
63. R.W.McMillan, R.A.Bohlander, G.R.Ochs, R.J.Hill, and S.F.Clifford, "Millimeter Wave Atmospheric Turbulence Measurements: Preliminary Results and Instrumentation for Future Measurements," *Optical Engineering*, **22** (1983)
64. R.J.Hill, and W.P.Schoenfeld, "Turbulence-induced millimeter-wave scintillation coompared with micrometeorological measurements," *IEEE trans. Geoscience and remote sensing*, **26** (1988)
65. R.W.McMillan, "Intensity and Angle-of-Arrival Effects on Microwave Propagation Caused by Atmospheric Turbulence," *IEEE Internatinoal Conference on Microwave, Communications, Antennas and Electronic Systems (COMCAS)*, (2008)
66. N.Gopalsami and A.C.Raptis, "Millimeter-wave Radar Sensing of Airborne Chemicals," *IEEE Trans. Microwave and Techniques*, **49** (2001)

67. C.D.Boone, K.A.Walker, and P.F.Bernath, "An efficient analytical approach for calculating line mixing in atmospheric remote sensing applications," *J. Quan. Spec. & Rad. Transfer*, **112**(6) (1990)

68. M.Kessler, H.Ring, R.Tramborulo, and W.Gordy, "Microwave Spectra and Molecular Structure of Methyl Cyanide and Isomeghyl Cyanide," *Phys. Rev*, **79** (1950)

69. H.Harde, S.Keiding, and D.Grischkowsky, "THz commensurate echoes: Periodic rephasing of molecular transitions in free-induction decay," *Phys. Rev. Lett.*, **66** (1991)

70. D.Mittleman, R.H.Jacobsen, R.Neelamani, R.G.Baraniuk, and M.C.Nuss, "Gas sensing using terahertz time domain spectroscopy," *Appl. Phys. B*, **67** (1998)

71. J.S.Melinger, A.Shutler, Y. Yang, and D.Grischkowsky, "Long path THz detection of small molecule vapors in the atmopheric transparency windows," *Conference on Lasers and Electro-optics (CLEO 2011)*, **CThEE7** (2011)

72. J.S.Melinger, Y. Yang, M.Mandehgar, and D.Grischkowsky, "Remote THz Monitoring of an Evolving Gas-Phase Mixture," *Conference on Lasers and Electro-optics (CLEO 2013)*, **CM3J.4** (2013)

PUBLICATION LIST

PUBLICATIONS

Yihong Yang, M. Mandehgar and Daniel Grischkowsky, 'Broadband THz Signals Propagate through Dense Fog', *Photonics Technology Letters*, submitted, (2014).

Yihong Yang, M. Mandehgar and Daniel Grischkowsky, 'THz-TDS Characterization of the Digital Communication Channels of the Atmosphere and the Enabled Applications', *J. Infrared Milli. Terahz. Waves*, to be published, (2014).

M. Mandehgar, **Yihong Yang** and Daniel Grischkowsky, 'Experimental Confirmation and Physical Understanding of Ultra-High Bit Rate Impulse Radio in the THz Digital Communication Channels of the Atmosphere', *Journal of Optics*, Accepted, (2014).

Yihong Yang, M. Mandegar and Daniel Grischkowsky, 'Determination of the Water Vapor Continuum Abosption by THz-TDS and Molecular Response Theory', *Opt. Express*, **22**(4), 4388-4403, (2014)

M. Mandehgar, **Yihong Yang** and Daniel Grischkowsky, 'Atmosphere characterization for simulation for the two optimal wireless terahertz digital communication links', *Opt. Lett*. **38**(17), 3437-3440, (2013).

Daniel. Grischkowsky, **Yihong Yang** and M. Mandehgar, 'Zero-frequency refractivity of water vapor, comparison of Debye and van-Vleck Weisskopf theory', *Opt. Express*, **21**(16), 18899-18908, (2013).

Yihong Yang, Mandehgar, and Daniel Grischkowsky, 'Time domain measurement of the THz refractivity of water vapor', *Opt. Express* **20**(24), 26208-26218, (2012).

Yihong Yang, Mahboubeh Mandehgar, and Daniel Grischkowsky, 'Understanding THz Pulse Propagation in the Atmosphere', *IEEE Trans. Terahertz Sci. Tech*. **2**(4), 406-415, (2012).

Joseph S. Melinger, **Yihong Yang,** Mahboubeh Mandehgar and Daniel Grischkowsky, 'THz detection of small molecule vapors in the atmospheric transmission windows', *Opt. Express*, **20**(6), 6788-6807, (2012).

Yihong Yang, Mahboubeh Mandehgar, and Daniel Grischkowsky, 'Broad-band THz pulse transmission through the atmosphere', *IEEE Trans. Terahertz Sci. Tech.* **1**(1), 264-273, (2011).

Yihong Yang, Alisha Shutler, and Daniel Grischkowsky, 'Measurement of the Transmission of the Atmosphere from 0.2 to 2 THz', *Opt. Express* **19**(9), 8830-8838, (2011).

CONFERENCES

Yihong Yang, Mahboubeh Mandehgar, and D. Grischkowsky, 'Determination of Water Vapor Continuum Absorption, Using Long-Path THz-TDS without the Cross-Term', 39th International Conference on IRMMW-THz, Tucson, AZ, Sep. 2014.

Yihong Yang, Mahboubeh Mandehgar and D. Grischkowsky, 'Measurements of Broadband THz Pulse Propagation through Dense Fog', Conference on Laser and Electro-Optics (CLEO), San Jose, CA, June, 2014.

Joseph S. Melinger, **Yihong Yang**, Mahboubeh Mandehgar, D. Grischkowsky, 'Remote THz monitoring of an evolving gas-phase mixture', Conference on Laser and Electro-Optics (CLEO), San Jose, CA, Jun, 2013.

D. Grischkowsky, **Yihong Yang**, Mahboubeh Mandehgar, 'The THz refractivity of water vapor', 37th International Conference on IRMMW-THz, Wollongong, Australia, Sep. 2012.

D. Grischkowsky, Joseph S. Melinger, **Yihong Yang**, Mahboubeh Mandehgar, 'THz detection of small molecule vapors in the atmospheric transmission windows', Naval Research Lab, Washington DC, Mar, 2012.

Joseph S. Melinger, **Yihong Yang**, Mahboubeh Mandehgar, Alisha Shutler, D. Grischkowsky, 'THz detection of small molecule vapors over long paths in the atmospheric transmission windows', 36th International Conference on IRMMW-THz, Houston, TX, Oct. 2011.

Yihong Yang, Mahboubeh Mandehgar and D. Grischkowsky, 'Long Path (167m) Broad-Band THz Transmission through the Atmosphere', Conference on Laser and Electro-Optics (CLEO), Baltimore, MA, May, 2011.

Yihong Yang, Alisha Shutler and D. Grischkowsky, 'Precise Measurement of the Transmission of the Atmosphere form 0.2 to 2 THz', Conference on Laser and Electro-Optics (CLEO), Baltimore, MA, May, 2011.

Joseph S. Melinger, Alisha Shutler, **Yihong Yang**, and D. Grischkowsky, 'Long Path THz Detection of Small Molecule Vapors in the Atmospheric Transparency Windows', Conference on Laser and Electro-Optics (CLEO), Baltimore, MA, May, 2011.

VITA

Yihong Yang

Candidate for the Degree of

Doctor of Philosophy

Thesis: STUDIES OF ATMOSPHERIC EFFECT ON FREE-SPACE THZ PULSES PROPAGATION AND APPLICATIONS

Major Field: Electrical Engineering

Biographical:

Education:

Completed the requirements for the Doctor of Philosophy in Electrical Engineering at Oklahoma State University, Stillwater, Oklahoma in August, 2014.

Completed the requirements for the Master of Engineering in Material Physics at Nankai University, Tianjin, China in 2009.

Completed the requirements for the Bachelor of Science in Material Physics at Nankai University, Tianjin, China in 2006.

Experience: Designed and built the world longest indoor (170 m) long-path THz-TDS system. Conducted experiments and developed the numerical model of atmospheric water vapor absorption. Investigated and obtained the most accurate continuum absorption of water vapor. Investigated the atmospheric effects on THz signal propagation.

Professional Memberships: IEEE Student Member; OSA Student Member; APS Student Member; SPIE Student Member;